Title
Microfluidics and Multiferroics Technologies for Single-Cell Manipulation and Analysis

Author
Khojah, Reem Ibrahim

Publication Date
2019

Peer reviewed|Thesis/dissertation

UNIVERSITY OF CALIFORNIA
Los Angeles

Microfluidics and Multiferroics Technologies for Single-Cell Manipulation and Analysis

A dissertation submitted in partial satisfaction
of the requirements for the degree
Doctor of Philosophy in Bioengineering

by

Reem Ibrahim F Khojah

2019

ABSTRACT OF THE DISSERTATION

Microfluidics and Multiferroics Technologies for
Single-Cell Manipulation and Analysis

by

Reem Ibrahim F Khojah
Doctor of Philosophy in Bioengineering
University of California, Los Angeles, 2019
Professor Dino Di Carlo, Chair

Sorting engineered cells with unique properties or functions from a larger population represents the future for personalized cell therapy and diagnostics. High-throughput and high-content single-cell sorting methods enable selecting specific desirable cell subpopulations from a heterogeneous mixture and facilitate extracting wealthy information of medically relevant biomarkers. This thesis explores programmable microfluidic and multiferroic methods for cell sorting and analysis. Microcavity flow was used to passively separate cancer cells from blood in high-throughput. Cavity flow physics was explored for size-based capture of cells. To expand cell sorting automation and artificial intelligence integration in microfluidic devices, suspended micromotor system was developed and controlled with computer-assisted image analysis software to enable modular sorting of cells, cells encapsulated in droplets, cell clusters, and organoids of any size. Next section, programmable magnetoelastic microstructures were coupled with microfluidic devices for single-cell manipulation. Magnetoelastic materials with controllable intrinsic magnetic properties were used for single-cell capture/release in highly parallel arrays. Microfluidic and multiferroic cell sorting technologies will potentially enhance single-cell profiling across diverse cancer cells for personalized medicine and support cell engineering technologies through a precise selection of high-performing cells.

The dissertation of Reem Ibrahim F Khojah is approved.

Alireza Khademhosseini

Pei-Yu Chiou

Jeffrey D Eldredge

Dino Di Carlo, Committee Chair

University of California, Los Angeles

2019

This dissertation is dedicated to my family and friends for their love and support.

Table of Contents

0.1 Introduction 1

1 Size-tunable microvortex capture of rare cells 4

1.1 Introduction 4

1.2 Methods 6

1.2.1 Device fabrication 6

1.2.2 Device Operation 7

1.2.3 Image Analysis 7

1.2.4 Particle and Cell suspension 8

1.2.5 Simulation 9

1.3 Results and discussion 9

1.3.1 Particle Migration to Microvortex Flow 9

1.3.2 Microvortex Size-Based Radial Seperation 10

1.3.3 Tunable Size Selective Capture of Cells 13

1.3.4 Rare cell capture in blood 14

1.4 Summary 15

2 3D Confined Microcavity Flow 25

2.1 Introduction 25

2.2 Methods 26

2.2.1 Experimental methods 26

2.2.2 Numerical Simulation 27

2.2.3 Scaling arguments 28

2.3 Results and discussion 29
2.3.1 Recirculating cavity flow formation and logistic growth . . 29
2.3.2 Separatrix breakdown 31
2.4 Summary 32

3 Motor-driven Microfluidics 44
3.1 Introduction 44
3.2 Results and Discussion 46
3.2.1 Motor-driven flow 46
3.2.2 Modular microflow control 47
3.2.3 Automated modular sorting 48
3.3 Materials and methods 48
3.3.1 Simulation 48
3.3.2 Imaging 49
3.3.3 Micro-motor operation 50
3.3.4 Carrier fluid, particle suspension and droplets 50
3.4 Summary 50

4 Cytocompatible Magnetostrictive Microstructures for Nano- and Microparticle Manipulation on Linear Strain Response Piezoelectrics 58
4.1 Introduction 58
4.2 Methods 61
4.2.1 Fabrication of microstructures on piezoelectric substrate and magnetization state initialization 61
4.2.2 XMCD-PEEM for magnetic domain imaging 63

4.2.3 Nanomagnetic particle preparation 63
4.2.4 Trapping of superparamagnetic beads by stray field from Ni and FeGa microstructures 64
4.2.5 Electric-field-driven particle motion 64
4.2.6 Optical microscope and Fluorescent microscope imaging and data analysis 65
4.2.7 Microfluidics integration 65
4.2.8 Cell viability test 66
4.3 Results and discussion 66
4.3.1 XMCD-PEEM imaging of the microstructure arrays and localized fluorescent bead trapping 66
4.3.2 Strain profile characterization 68
4.3.3 Electric-field-driven particle displacement 69
4.3.4 Cell viability on magnetoelectric devices 70
4.4 Summary 71

5 Programmable Single Domain Terfenol-D Micromagnets for Single-cell Manipulation 77
5.1 Introduction 77
5.2 Results and discussion 79
5.2.1 Terfenol-D single domain micromagnets 79
5.2.2 Single domain uniform micromagnetic trapping 80
5.2.3 Single-domain magnetic localization 81
5.2.4 Programmable multiferroic magnets for particle and cell capture/release 82

5.3 Methods 84
5.3.1 Film deposition and micropatterning 84
5.3.2 Scanning electron microscopy imaging (SEM) and Magnetic Force Microscopy (MFM) 84
5.3.3 Magnetic hysteresis loop: Superconducting quantum interference device (SQUID) 85
5.3.4 Magnetic domain imaging by X-ray magnetic circular dichroism photoemission electron microscopy (XMCD-PEEM) . 85
5.3.5 Microfluidic device integration 86
5.3.6 Microscopy imaging and image analysis 87
5.3.7 Cell Culture and labeling 87
5.4 Summary 87

References **100**

List of Figures

0.1 Precise single-cell manipulation technologies lead to profiling heterogeneous physical and biochemical phenotypic properties of a single-cell. 3

1.1 Microfluidic device principle and operation. (a) Schematic of a single-channel device with an upstream filter to prevent debris from blocking the channel. Downstream flow divider and diffuser to prevent backflow and capture of cells at the outlet. Micro-cavity was placed 1 cm from the inlet. Microvortex flow form between leading and trailing walls of the cavity at high Reynolds number. (b) Polydispersed rare cells (clusters, large and small cells) are captured by different microvortices generated in the same device. Inertial flow conditions (Re) are tuned to generate a distinct vortical flow geometry with specific capturing properties: Phase I ($Re = 100-175$) capture clusters, phase II ($Re = 175-225$) capture large cells and phase III ($Re = 225 - 300$) capture small cells 16

1.2 Microfluidic device geometry and trapping reservoir (cavity) dimensions. Different cavity aspect ratios (AR) are designed to test radial migration of particles in microvortices. Cavity length (L), width (W) and height (H) are along the X, Y and Z directions respectively. Cavity is placed 1 cm away from the inlet. All cavities are made of the same height (H = 70 μm.). Rectangular channel width (W_{ch}) is 40 μm and channel height (H_{ch}) is 70 μm. 16

1.3 Microvortex core characterization. (a) COMSOL Multiphysics model of velocity distribution in microcavity (AR =2) recirculation region. Different vortex topologies generated at different inertial conditions defined by the mean-flow Reynolds number (Re) in a rectangular channel. Vortex core was identified by the local velocity minimum inside the cavity at different flow rates. (b) Schematic illustration of x-y plane of the cavity and location of vortex core (x0, y0). (c) Vortex core coordinates along x-axis in the cavity at Reynolds number (Re) 100, 150, 200, 250 and 300. 17

1.4 Radial migration phenomena description at different inertial flow conditions (Re): Each three columns of images (a-e) represent an example of an inertial flow condition in phase I ($Re = 100-175$), phase II ($Re = 175-225$) and phase III ($Re = 225-300$). (a) Flow streamlines (grey lines) and velocity distribution (color contours) of laminar vortical flow in the cavity with aspect ratio ($AR = 1$) at $Re = 150$, 200 and 300. The color scale represents the velocity magnitude (m/s). We specified the range of velocity magnitude were it saturates at (0.04 m/s) to show the vortex core of each microvortex flow. (b) Time-lapse of high-speed image of single polystyrene particles show the transition of equilibrium orbits in each capture phase. (c) Particle tracing inward radial migration switch between large particle ($\lambda > 0.5$) (red) and small particle ($\lambda < 0.5$) (blue). (d) Bright field images captured with high-speed recording of polystyrene particle suspension illustrates their motion transition between phases. All scale bars represent 120 μm. (e) Scatter plot of polydisperse polystyrene beads illustrate orbital transition towards vortex core between phase I and phase III. The color scale represents scaled bead diameter (λ). (f) Average orbital radius (O_r) of polydisperese beads over different inertial conditions (Re) illustrates the switch of size-dependent orbital radius in different flow rates. 18

1.5 Relationship of size-dependent vortex capture and average orbital radius of cells. Each three columns of images (a-c) represent an example of an inertial flow condition in phase I ($Re = 100 - 175$), phase II ($Re = 175 - 225$) and phase III ($Re = 225 - 300$) (a) Flow streamlines (grey lines) and velocity distribution (color contours) of laminar vortical flow in cavity with aspect ratio ($AR = 2$) at $Re = 100$, 200 and 300. The color scale represents the velocity magnitude (m/s). (b) MDA-MB-231 cell lines self assemble in different size-selective trapping phases. All scale bars represent 60 μm. (c) Size distribution scatter plot of tracked cells inside microvortex flow from different experiments. The color scale represents scaled cell diameter (λ). (d) Average orbital radius O_r of polydisperese cells over different inertial conditions (Re) show the switch in size-based equilibrium orbits after phase II. (e) MDA-MB-231 cell line size distribution and captured cells in different Reynolds number (Re). Each Reynolds number form a micro-vortex with specific capture efficiency. Plot of single capturing unit (one cavity) efficiency (secondary axis on the right) . . 19

1.6 Scatter plot of captured cells size distribution and their orbit trajectories in AR = 1 cavity. Cell motion and progression in micro-vortices illustrates size selective orbit transition in increasing flow conditions at Reynolds number (Re) 100, 125, 150, 175, 200, 225, 250, 275 and 300. 20

1.7 Microvortex loading capacity for MCF-7 ($\lambda > 0.5$) cells) and MDA-MB-231 ($\lambda < 0.5$). Flow of concentrated cell suspension for five minutes followed by PBS wash for five minutes in three inertial conditions at Re = 150, 240 and 300. Microvortex capture of MCF-7 with mean cell diameter = 25 μm and MDA-MB-231 = 18 μm show size-selective capacity in phase I (Re = 150) and phase III (Re = 275) respectively. 21

1.8 Captured MDA-GFP orbit trajectories in microvortex flow with PBS and blood. Bright field (left) and fluorescent (right) images of PBS and 20x diluted blood spiked with MDA-GFP cell lines in microvortex flow show consistent orbit trajectories. Fluorescently labeled cancer cell line MDA-GFP orbit trajectories observed in phase I (Re = 125), phase II (Re = 200) and phase III (Re = 300). 21

1.9 Device performance of rare cells capture from blood samples. (a) Immunofluorescent staining and classification criteria. Collected cells were classified according to immunostains against GFP (green) and CD45 (red), as well as DNA stained with DAPI (blue). MDA-GFP cells are identified as GFP+/CD45-/DAPI+ and WBCs as GFP-/CD45+/DAPI+. (b) Purity and capturing unit efficiency of collected MDA-GFP spiked in blood. (c) Cells released from microvortex flow are able to grow and proliferate after 4 days. 22

1.10 Vortex HT device capture efficiency and size selectivity for MDA-GFP in blood. Isolation and capture of MDA-GFP cells spiked in 20X diluted blood were tested on a High-Throughput vortex device under phase I and phase III flow conditions. (a) The captured MDA-GFP population were segmented to large cells with diameter (a $>$ 25 μm, $\lambda > 0.5$) and small cells (a $<$ 25 μm, $\lambda > 0.5$). Phase I shows high capture efficiency for large cells ($\lambda > 0.5$) while phase III shows high capture efficiency for small cells ($\lambda < 0.5$). (b) The size distribution of captured cells from phase I and III, shows a consistent size selectivity for each flow condition with the vortex device. 23

1.11 Size-based capture characterization of rare cells from the blood. (a) The size distribution of MDA-GFP isolated from blood starting phase I (Re = 125) flow conditions followed by phase III (Re = 275). The blood sample was recycled in the device in each phase. (b) The size distribution of isolated cells starting phase III (Re = 275) followed by phase I (Re = 125). (c) Captured cells in both phases and in different order show a significant difference in cell size distribution. Both phase I (Re = 125) (red) and phase III (Re = 275) (blue) are necessary to capture all MDA-MB-231 size distribution (grey). (*) p-value = 0.0001. 24

2.1 Cavity geometry dictates the vortical flow growth state at the same channel Reynolds number. Fluorescent microscope images of cavity flow shows the significant contribution of the cavity aspect ratio (H/X_s) to the flow growth in three dimensional confined cavities, where H = cavity height = channel height (μm), X_s = cavity side length (μm). The channel Reynolds number ($Re = \frac{UD_h}{\nu}$) were held constant across different cavity geometry, where the channel hydraulic diameter $D_h = \frac{2(WH)}{(W+H)}$ (m), U = fluid velocity (m/s), W = channel width (μm) and ν = kinematic viscosity (m^2/s). 34

2.2 Logistic growth of three-dimensional confined cavity flow. (A) Three dimensional cavity diagram with leading wall (x_1), side wall (x_2) and lagging wall (x_3). (B) Top down view of the experimental set up for confined cavity flow characterization by the transition of reattachment point (x^*) on all stationary cavity walls ($\sum x_i$). (C) Experimental ($\square$) and numerical simulation ($\diamond$) evidence of the logistic progression of the reattachment point (x^*) on the cavity walls with cavity side length (X_s = 250 μm) and cavity height (H = 70 μm) as a function of the channel's Reynolds number with 70×40 μm ($H \times W$) channel height and width. Color bar indicate the velocity profile (m/s) around the reattachment point on the cavity wall (white: fast, dark red: slow). . . 35

2.3 Reattachment point (x^*) calculation in numerical simulation results. The reattachment point is located when the y-component velocity (v) along the midpoint symmetry line on the cavity wall equals zero. On leading wall (x_1) flow going to the channel ($+v$) and flow going back to the cavity ($-v$). Similar to (x_3) with opposite velocity component signs. In the side wall (x_2), x-component velocity (u) is measured along the wall to determine the reattachment point. 36

2.4 Spatiotemporal plot of the reattachment point (x^*) progression. Experimental measurement of the reattachment point progression of different Reynolds's numbers as a function of time t(sec). Reattachment point stabilizes after one minute of changing the flow rate. A pronounced transition of cavity wall on the side wall (x_2) parallel to the direction of channel flow. 37

2.5 Universal scaling of cavity flow development through following the reattachment point evolution on the cavity wall. The figure shows the phases of cavity flow growth in the channel's Reynolds number (Re) versus the scaled channel's Reynolds number by the cavity aspect ratio (Re (H/X_s)). (A) Experimental result of the reattachment point (x^*) transition in different cavity side lengths ($X_s = 400 : 100 : 1000\ \mu m$) as a function of the channel's Reynolds number. (B) Empirical data of vortex growth data for different cavity sizes collapse when plotted as a function of the cavity geometry ratio and Reynolds number. The data set were fit in a logistic function presented in a solid red line (-) with parameters used in Eq. (2.1). 38

2.6 The channel width does not significantly contribute to the cavity circulating flow development with the scaled Reynolds number. The reattachment point (x^*) progression plotted against the scaled Reynolds number show no significant shift or difference with two channel widths W = 40 μm (blue) and 100 μm (red). 39

2.7 Universal scaling of microcavity flow logistic growth and correlation with cavity height. Colored symbols denote results of different cavity heights, (A) H= 70 μm (black), (B) H= 118 μm (red) and (C) H=130 μm (blue). (D) collection of all log-fit of different heights. 40

2.8 Reattachment point (x^*) measurement across different cavity locations along the channel validate the use of PDMS device for cavity flow study. Reattachment points (x^*) are plotted at different downstream cavity location ($\diamond$) near the inlet (high pressure region), ($\square$) middle of the channel and ($\triangle$) near outlet (low pressure region). Cavity flow develop similarly in different pressure points in PDMS device. Flow in the side wall x_2 is less uniform than other measurements. 41

2.9 Phase diagram showing three different flow transition of cavity flow (no cavity flow, half cavity flow and full cavity flow) as a function of the cavity aspect ratio (H/Xs). 41

2.10 (a) Schematic illustration of 2-D cavity flow imaging and experimental setup. The device with three inlet (Q1-Q3) flow, where two different fluorescent dyes Q1 (red rhodamine), Q2 (green fluorescein) label the streamlines near the channel-cavity flow, and Q3 colorless water on the other side of the channel. (b) Progression and formation of the circulating streamlines at different reattachment points reaching to full cavity flow. 42

2.11 (a) Schematic illustration of 3-D cavity flow confocal imaging and experimental setup by capturing 2D images with 1 μm increment for high spatial resolution. Fluorescent dye is applied in the midline of the inlets (Q2) to visualize how the flow unfold and exit from the cavity flow. (b) Separatrix breakdown of the vortex core near the trailing wall in confined cavity flow. Images are taken from the middle to the upper side of the cavity show flow symmetry with two dominant vortical flow exiting near the cavity upper and lower walls to the main channel flow. 42

2.12 2D fluorescent image of separatrix breakdown in cavity flow with swirling streamlines exiting from the cavity to the channel. 43

3.1 Schematic of automated motor-driven microfluidics work-flow for modular sorting systems. The top box illustrates continuous flow microfluidics work-flow for image-based binary sorting systems limited to single-cells. The bottom box illustrates modular unconfined motor-driven flow functionalities for automated non-binary sorting systems with intelligent 3D inspection of a wide size range of cellular and multicellular structures. 52

3.2 (a) Two side-by-side rotating motors suspended in fluid with opposite angular velocities ($\pm\Omega$) and identical circular shaft radius (a) with distance between the motor centroids ($|O1O2|/2 = L$). (b) Phase diagram showing motor-driven flow type development as a function of the Reynolds numbers and the distance between the two motors. 53

3.3 Spatio-temporal microflow control of one motor-driven flow unit at h=0.1 and a range of Re (0.12-1.5) show the ability to change the sample flow rate. Simulation and particle tracing experiments illustrate uniform Jeffery's flow at different motor angular velocity. 54

3.4 Modular microflow control via motor-driven microfluidics. An ensemble of micromotors can substitute the basic functions of confined microchannel pressure-driven flow like driving (a) shaping (b) and separating (c) the flow of a sample fluid. 55

3.5 3D inspection before sorting. Computer-assisted modular rotational flow allow 3D scanning of large cellular and multicellular structures spatial information (cells are stained with calcein green) with conventional fluorescent microscopy. 56

3.6 Automated modular motor-driven microfluidics sorting of droplets. The top panel shows the default state of motors flowing the sample and carrier fluid down when cells are not detected. When cells are detected in droplets, cells are then sorted based on their number to two different outlets. 57

4.1 Schematic of the sample and the relative orientations between the initial field direction and the PMN-PT principal strain axes. After the initialization field, H_{init}, is removed, an electric field is applied through the thickness of the ferroelectric PMN-PT via the top and bottom electrodes made of Pt thin films, inducing a differential in-plane strain. 72

4.2 Magnetization hysteresis loop measured by SQUID magnetometry for a suspension of the superparamagnetic nanobeads (600 nm in diameter) used for the fluorescent imaging. 72

4.3 Microfluidic chip integrated on the top surface of the magnetoelectric device. Arrays of magnetostrictive micropatterns are located at the center of the device, viewed by optical microscopy. 72

4.4 Fluorescent beads of 0.6 μm (green) trapped and localized on the magnetic domain walls of the Ni microstructures. (a) XMCD-PEEM images of Ni rings. (b) Overlay of bright field and fluorescent microscope images of fluorescent beads coupled to rings of 6 μm, 4 μm, and 2 μm in diameter. (c) Time-lapse images of 4 μm Ni rings capturing fluorescent bead (0.6 μm in diameter) in the microfluidic channel, corresponding to the location of the DWs of Ni rings, as shown in the PEEM images. (d) XMCD-PEEM images of Ni squares with 2 μm in length. (e) Overlay of bright field and fluorescent microscope images of fluorescent beads captures at the corners of 2 μm squares. (f) Time-lapse images of FeGa squares of 2 μm in length capturing fluorescent bead at the corner. Dashed circle highlighted the position of the fluorescent bead. . . . 73

4.5 (a) Representative particle trapping event in the absence of flow (1 μm particle, 4 μm diameter ring. Left: particle path overlaid on image of 4 μm Ni ring. (b) Particle displacement relative to position at time 0 (Euclidean distance) vs time over the course of the trapping event. Trapping occurs around 1.5 s and most random motion ceases. 73

4.6 (a) Initialized onion states in polycrystalline FeGa rings of varied width and diameter, with a thickness of 20 nm, observed by XMCD-PEEM. (b) Rings of various sizes in (a) trapping fluorescent nanoparticles via the magnetic stray field emanating from the onion state domain. (c) Squares of 2 μm in length trapping fluorescent particles on the corners. 74

4.7 Time-lapse images of 2 μm ring (No. 3) capturing a fluorescent bead in the microfluidic channel, corresponding to the location of the DWs of FeGa rings, as shown in the PEEM images. Ring No. 1 and No. 2 have captured beads prior to No. 3. All the three rings trapped beads locally along the x direction, in which H_{init} was applied. 74

4.8 (a) Magnetoelectric device is mounted on a leadless chip carrier (LCC), and a biaxial strain gauge is mounted on the surface of the device for strain profile characterization. (b) Linear strain response along the [01-1] and [100] directions of the PMN-PT substrate to the applied electric-field is measured using the strain gauge. 75

4.9 Continuous magnetic bead movement, driven by applied electric field to the PMN-PT with linear strain response, along the perimeter of the Ni ring, 4 μm in diameter and 600 nm in width, captured by optical microscope. The diameter of the bead is 1 μm. 75

4.10 (a) XMCD-PEEM images of a Ni square with a magnetic vortex state at zero electric field, and evolves into a two-domain state at 0.36 MV m^{-1}, (b) a Ni square of 2 μm in length trapping fluorescent beads on the corners before and after applying voltage and (c) Sample orientation with respect to the initialization magnetic field direction. 76

4.11 Viability test on multiferroic heterostructure platform using Calcein AM stain (a) stained viable cells, (b) stain leakage of damaged cells, (c) before applying voltage and (d) after ramping up the voltage to 400 V applied to the top and bottom electrodes, with corresponding electric field up to 0.8 MV m^{-1}, the cells are viable for downstream bio-applications. 76

5.1 Schematic of single-domain magnetics potential upgrade in bio-applications precision and control at the micro-scale. Single-domain size limit (left side) of magnetically initialized magnetoelastic material. Terfenol-D has the largest single domain state (20 μm). Single-domain stray field (red dotted lines) are strong, uniform and tunable to magnetically control a wide range of cell sizes. Other magnetoelastic material breaks in multi-domain state (right side) around 1 μm in diameter. 89

5.2 Magnetic characterization of Terfenol-D microstructures. (A) Terfenol-D microdisks on Si 50 nm thick, diameters of 3 μm and 20 μm) show single domain configuration with Magnetic force microscopy imagin.(B) Magnetic hysteresis loop of the Terfenol-D disks of 3 μm in diameter shows large saturation magnetization of 780 emu/cc and a coercivity of 0.23 T, as measured by SQUID. A large fraction of the magnetization is retained upon the removal of saturation magnetic field. (C) The x-ray absorption spectrum with the Fe edges confirms the non-oxidized state of the Terfenol-D microstructure. The XMCD-PEEM image is acquired after in-situ etching that removes the 4 nm thick protective Ta layer on the Terfenol-D. Magnetic contrasts taken by PEEM at the elemental absorption edges of all three elements (Tb, Dy, Fe) in the Terfenol-D confirm the single domain configuration in the 20 μm Terfenol-D microstructures. The black contrast indicates the magnetization is pointing along the +x direction; the white indicates the magnetization is pointing in the -x direction. The entire disk functions nearly as a magnet with single domain. 90

5.3 An example of single domain and multi-domain in disks at relaxation, simulated by mumax micromagnetics modeling . B.XMCD-PEEM micrographs of magnetoelastic disks of 2 um in diameter, and 20 nm in thickness (polycrystalline Ni, Fe81Ga19 and Co40Fe40B20). Compared to polycrystalline Terfenol-D disks with single domain on the micron scale, these microdisks already exhibit multidomain behavior at 2 um in diameter, implying the domain configuration in even larger structures including disks will fall into multidomains. 91

5.4 Microfluidic device integration with magneto-elastic microstructurs substrate. (A) Microfluidic channel integration with Terfenol-D micropattern on sapphire substrate to visualize magnetic beads (fluorescent label : green) trapping. (B) Before (left) and after (right) magnetic bead (fluorescent label : red) localization on the x-axis poles on different Terfenol-D microstructures. 91

5.5 Uniform single domain trapping vs non-uniform multi-domain trapping. Heat map of beads trapping locations on magnetically initialized (x-axis) Terfenol-D (TdDyFe) (right) and Galfanol (FeGa) (left) of 10 and 20 μm disks. Magnetic beads are trapped only on the x-axis poles of the Terfenol-D while scattered around the x-axis poles of FeGa. 92

5.6 Uniform localized stray field gradient of Terfenol-D magnetostrictive microstructures. Fluorescent nanomagnetic particle (green) capture with high trapping rate and precision. 92

5.7 Magnetic bead trapping maps on Terfenol-D and Galfenol microstructures 20, 10, 5, 3 μm disks, 10 μm square, x=3 μm and y=6 μm vertical ellipse and finally x=6 μm and y=3 μm horizontal ellipse. Fluorescent images of labeled magnetic beads of more than 20 microstructures are overlaid and analyzed. Contour plot darker red regions correspond to high magnetic beads trapping region and lighter areas depicts low trapping regions. This exhibits precise localization and magnetic trapping of single domain Terfenol-D over various thin film structures. 93

5.8 Stray field magnetic trapping range from the surface of the the Terfenol-D magnetized poles. (a) Magnetic bead trapping trajectory around Terfenol-D show a transition from random brownian motion to particle displacement towards the magnetized pole of the microdisk. This suggests the effective trapping region of stray field is (2.54 μm).(B) Magnetic particle trapping trajectory show particles accelerating towards the magnetized poles before trapping (scale bar = 20 μm). (C) Small gaps between Terfenol-D microdisk pattern result in less trapping and accumulation of magnetic beads (fluorescent label : red) (scale bar : 100 μm). (D) Magnetic particles (fluorescent label : green) trapped and aligned on the stray field lines and form bridges between Terfenol-D microstructures (scale bar : 50 μm). 94

5.9 Programmable magnetic trapping poles on 20 μm Terfenol-D microdisks magnetized on the y-axis (top) and diagonally (bottom). This demonstrates the programming ability to control magnetic beads (fluorescent label : orange) trapping locations at a micro-scale. (scale bar = 20 μm) 95

5.10 Nanomagnetic controlled assembly. Controlled assembly of two different functionalized magnetic nano -particles on single magnetic Terfenol-D disks (3 μm) via two magnetization steps in the x -axis (fluorescent label : green) and y -axis (fluorescent label : orange)(scale bar = 1 μm). 95

5.11 Stray field (H_s) initialized diagonally trap magnetic beads moving towards and external magnetic field (B) from large permanent magnet (NdFeB). 96

5.12 Experimental study of fluid born particle interaction with Terfenol-D magnetostrictive microstructures. Three particle-Terfenol-D disk interaction states (i) stagnant particle at initial flow rate (Q_0) when magnetic force dominates over hydrodynamic drag force ($F_m > F_d$). (ii) Increasing flow rate by ($\triangle Q$) demonstrates particle tumbling between Terfenol-D magnetic domain walls when Magnetic binding force is equal or similar to hydrodynamic force ($F_m \approx F_d$). Binding time decrease when hydrodynamic drag force starts to dominate over magnetic binding force. (iii) Last state is particle release when hydrodynamic drag dominates over magnetic binding force ($F_m < F_d$). . . . 96

5.13 Calculation of Hydrodynamic simulation of magnetostrictive microstructure interaction with particle in flow. The drag calculations were performed using COMSOL Multiphysics software Finite Element Method (FEM) to solve the partial differential equations that dictate the physical system to simulate the fluid-particle interactions. 97

5.14 Cell manipulation with Terfenol-D micromagnets. (A) Single-cell labeled with magnetic beads were localized in Terfenol-D magnetized poles. Large cells and cell clusters are trapped between two Terfenol-D microstructures. (B) Cells captured by Terfenol-D at low flow were then released by increasing the flow rate, in which hydrodynamic drag dominated over the magnetic binding force. (C) Captured cells were successfully grown on the Terfenol-D micropattern submerged in media. 98

5.15 Programmable multiferroic micromagnets for single cell capture/release. (A) schematic of magnetoelastic microstructure Terfenol-D on ferroelectric PMN-PT substrate. (B) Magnetic bead capture on Terfenol-D microdisk (diameter = 20 μm). (C) Magnetic bead release due to the rotation of the initial magnetization state of Terfenol-D disk via voltage induced strain when electric field is applied through PMN-PT substrate. (D) An electric field of 0.8 MV m^{-1} induces compressive strain of 900 ppm along [100] direction and tensile strain of 300 ppm along [0-11] direction. The resulting total strain of 1200 ppm, perturbs the single domain state due to magnetic anisotropy variation following which magnetic beads were released from the TerfenolÂŋ-D micromagnets to the outlet of the microchannel. 99

List of Tables

Acknowledgments

I would like to thank my advisor Professor Dino Di Carlo for his endless support and encouragement. His guidance has been the most important contributor to my success. I am very fortunate for his mentorship, confidence in me throughout my research and, most of all, his friendship. Also, I would like to extend my gratitude to his wife Melissa for hosting lab socials with her wonderful family.

I have been blessed by lifelong friendships at UCLA with brilliant and passionate people. I would like to thank my labmates and research collaborators who have played significant roles in my research.

I would especially like to thank Professors Ali Khademhosseini, Pei Yu Eric Chiou and Jeffrey D. Eldredge who have been members of my Ph.D. committee for their support and advice in my thesis.

Microfluidics chapters (1,2,3): I would like to thank Dr. Oladunni Adeyiga for her contribution in blood sample collection. I would like to thank Professor Jeffrey D. Eldredge for his valuable input. He is a great teacher, the kind that makes you excited to start working on the homework right after a two-hour class of deriving and solving fluid mechanics problems. My undergraduate students, Ryan Stoutamore, Fiona Tang, Darren Lo, Michael Margolis and Micheal Bogumil for helping in experimentation and image analysis. Finally, I gratefully acknowledge the support of the California NanoSystems Institute (CNSI) at the University of California, Los Angeles.

Multiferroics chapters (4,5): I would like to thank Professors Gregory P. Carman, Robert N. Candler, Christopher S. Lynch, Abdon E. Sepulveda and Jeffrey Bokor who have provided tremendous help and advice. This work was supported by the NSF Nanosystems Engineering Research Center for Translational Applications of Nanoscale Multiferroic Systems (TANMS) under the Cooperative Agree-

ment Award (EEC-1160504). The work at the Advanced Light Source at Lawrence Berkeley National Laboratory is supported by the Director, Office of Science, Office of Basic Energy Sciences, U.S. Department of Energy, under contract number DE-AC02- 05CH11231.

My parents were a great and constant source of support, thank you for working hard to provide the best education for me. To my mother, your unconditional love and the Compaq Presario 2100 enabled me to nurture my academic curiosity. To my grandmother, Aziza, my aunt Fatmah, my sisters Abrar and Sara, and my brother Muhammed, thank you for your continual cheers and support.

I would like to thank my brilliant husband and best friend, Faisal, who makes science, engineering and research looks so simple. His courage in marching towards new research alleys in the pursuit of pushing the limits of science and technology, encourages me everyday to take a few steps towards open scientific questions and tolerate the ambiguity of long laboratory experiments. Thank you for supporting me through my Ph.D. journey. To my son, you are the love of my life, the sun of my life and everything in my whole life.

Finally, I dedicate this work to all researchers working in the democratization of health care by building accessible diagnostic and therapeutic technologies to serve people around the world.

Vita

2009–2011	M.Sc. Chemical and Biological Engineering, King Abdullah University for Science and Technology. Research: Single-molecule analysis of DNA replication via T7 polymerase under hydrodynamic flow.
2003-2008	B.S. Medical Technology, King Abdul-Aziz University. Research: Comprehensive review of VDJ immunoglobulin gene rearrangement.

Publications

10. (In preparation: chapter 2) Reem Khojah, Darren Lo, Fiona Tang and Dino Di Carlo, **The evolution of flow entry and exit in 3D confined microcavity flow**.

9. (In preparation: chapter 3) Reem Khojah, Michael Margolis, Marc Van Zee and Dino Di Carlo. **Motor-driven microfluidics for modular sorting systems**.

8. (In preparation : chapter 5) Reem Khojah*, Zhuyun Xiao*, Mohanchandra K. Panduranga*, Rajesh V. Chopdekar, Michael Bogumil, Gregory P. Carman, Rob N. Candler and Dino Di Carlo. **Programmable single domain Terfenol-D micromagnets for single-cell manipulation**.

7. Zhuyun Xiao*, Reem Khojah*, Marc Chooljian*, Roberto Lo Conte, Kevin Fitzell, Yilian Wang, Dino Di Carlo, Rob N. Candler and Gregory P. Carman. **Cytocompatible magnetostrictive microstructures for nano- and microparticle manipulation on linear strain response piezoelectrics**, Multifunctional Materials 1.1 (2018): 014004.

6. Reem Khojah, Ryan Stoutamore, and Dino Di Carlo. (2017). **Size-tunable microvortex capture of rare cells**. Lab on a Chip, 17(15), 2542-2549.

5. Manjima Dhar, Reem Khojah, Andy Tay and Dino Di Carlo. (2015), **Research highlights: microfluidic-enabled single-cell epigenetics**. Lab on a Chip, 15(21), 4109-4113.

4. (Under reviw) Yu-Ching Hsiao*, Reem Khojah*, Xu Li, Auni Kundu, Cai Chen, Daniel B. Gopman, Andres C. Chavez, Zhuyun Xiao, Abdon E. Sepulveda, Rob N. Candler, Gregory P. Carman, Dino Di Carlo and Christopher S. Lynch. (2019), **Capturing magnetic bead-based arrays using perpendicular magnetic anisotropy (PMA)**.

3. (In preparation) Mohanchandra K. Panduranga, Zhuyun Xiao, Taehwan Lee, Reem Khojah, Dino Di Carlo, Rob N. Candler and Gregory P. Carman. (2019), **Side-wall protected Terfenol-D micropatterns for multiferroic applications**.

2. (In preparation) Michael Guevara*, Reem Khojah*, Yu-Ching Hsiao*, Andres C. Chavez, Kevin Fitzell, Auni Kundu, Dino Di Carlo, J.P. Chang, Gregory P. Carman and Christopher Lynch, **Assessing the use of magnetostrictive ellipse nanostructures for capture and release of superparagmagnetic beads in biomedical applications.**.

1. (In preparation) Patrick Corona*, Reem Khojah*, Dino Di Carlo, Gary Leal, and Mathew Helgeson. **Microroller four roller mill for polymers and nanoemulsion birefringence and SANS measurements**.

* Equal contribution

0.1 Introduction

Microfluidic and magnetic cell separation have been effective methods for cell capture and isolation. However, newly discovered heterogeneity of cell phenotypic properties requires fine control of microflow and micromagnetic field to sort cells with complex phenotypic properties. For example, a single-cell possesses many medically relevant phenotypic properties like the level of cell receptor expression and kinetics [30, 101], cytokine secretion [89], cell-cell interactions [114] and phosphorylation state of signaling pathways [10]. In addition to physical cell properties like size, density and deformability (Fig. 0.1). Thus, there is a need to individually select cells based on multiple phenotypes.

The purpose of this dissertation is to provide microfluidic and multiferroic platforms for highly controlled single-cell separation and manipulation. Although both topics are interdisciplinary in nature, the focus of this research is to provide bioengineering solutions to single-cell sorting at the micro-scale. The first three chapters of the dissertation present two microfluidic label-free cell separation methods. The first method provides a high-throughput inertial cell separation from the main microchannel to microvorticies. The second method although operates in viscous conditions, but offer high spatial and temporal controllability via micro-motor driven flow. The last two chapters introduce a new method in magnetic cell separation via the use of programmable magneto-elastic materials. A proof of concept of cell manipulation via multiferroic device shows controllable micro-scale displacement of magnetic beads via voltage induced strain on magnetostictive material microstructures (Ni and FeGa) [132]. The last chapter shows a novel magnetostrictive material (Terfenol-D) ability to magnetically capture and release cells without an external magnetic biasing field. Switching the magnetic state (on/off) of magnetoelastic microstructures via voltage induced stain introduces a high-throughput programmable magnetic array for magnetically labeled

single-cell manipulation (capture/release).

A new generation of AI compatible microfluidic and multiferroic technologies enable programmable and localized control of cellular and sub-cellular structures with broad utility for intelligent and data-driven sorting and analysis.

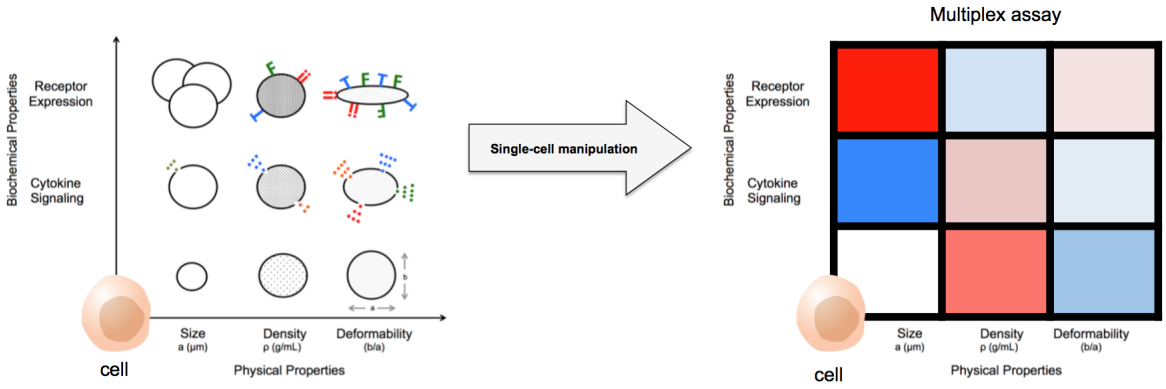

Figure 0.1: Precise single-cell manipulation technologies lead to profiling heterogeneous physical and biochemical phenotypic properties of a single-cell.

CHAPTER 1

Size-tunable microvortex capture of rare cells

1.1 Introduction

Inertial microfluidics has evolved into an efficient and tunable platform for general micro-scale manipulation and analysis of rare cells [23]. They enable high-throughput technologies to process large sample volumes in short analysis time. Most importantly, it offers superior features for blood components isolation and processing [137]. Fluid inertia becomes finite in a microfluidic system with high flow velocity ($1 << Re <\sim 100$) and below turbulent regimes. In this case, physical properties of suspended particles influence their motion by inertial migration or inducing secondary flow.[32] [85] This enable precise manipulation (i.e. focusing, sorting and separation) of bio-particles by controlling inertial flow properties. Many technologies use this feature by either inducing external forces (active separation) or using intrinsic hydrodynamic forces (passive separation) in sample processing. Active technologies were developed for cell separation such as dielectrophoresis (DEP)[58] [18] [53] , magnetophoresis (MP) [44] [57] [130], acoustophoresis (AP) [125][98] [91] [99] and optical tweezer[51] [24]. They allow precise and tunable control of target particle motion in suspension. However, external forces have to be balanced with limited flow speed, resulting in a significant throughput penalty.

Passive technologies, on the other hand, are simple, robust and solely based on controlling hydrodynamic properties of higher flow conditions. Methods as

pinched flow fractionation (PFF)[134] [115] [100], deterministic lateral displacement (DLD) [62], microfiltration [1] and inertial microfluidics [32] [124] were used for continuous cell separation. They enable label-free, high throughput and adaptive automation while conserving cell phenotypical properties for downstream analysis. However, these systems are incapable to separate and enrich target cells from other suspension components in one device. Biophysical measurements and tests cannot be performed on isolated cells in the same device as well. In addition, due to continuous flow separation, cells are collected out of the device in large collection volumes which leads to low purity and low recovery rate of cells. This cause a drawback in rare cells detection like circulating tumor cells (CTCs), in which no cell should be left behind for profiling and analysis [104]. It is challenging to modulate label-free size-based separation to capture rare cells with anisotropic size and deformability with fixed trapping properties [5]. In such a case, a redesign of device geometry is necessary to get different separation or trapping conditions.

Recently, our group developed long term and high-throughput cell entrapment in microvortices [64]. This enable processing (staining [20], conjugation[83] and transfection [120]) cells in the same device. The system can isolate CTCs from patient samples with high purity and efficiency [110] [31] [21], but lacks flexible size cut-off. This is the main limitation since cells from the same lineage are polydispersed in size. In addition, cells form clusters which challenge this method efficiency. CTC-clusters are associated with aggressive metastasis and worse clinical outcome in some cancers.[38]. In this work, we uncover a new particle trapping phenomenon that enables size-based modality of cell capture in confined flow. Through modulating the balance of intrinsic inertial forces, laminar vortices separate particles radially in preferential orbits based on their size. We explored different trapping properties over a range of flow rates in a single cavity geometry (Fig. 1.1a). Each flow condition generates distinct radial separation of

particles from the vortex core. We provide a new systemic understanding of three selective trapping phases based on the cavity's vortical flow properties. Experimental investigations of cell motion in mirco-vortex flow shows phase I maintain cell clusters, phase II maintain large cells and phase III maintain small cells in the cavity (Fig. 1.1b). We tested a set of flow conditions in different cavity geometries (Fig. 1.2) and phase trapping characteristics were consistent. In previous studies, cell trapping was practiced only in phase I conditions ($Re \sim 150$) due to a decrease in large particle trapping beyond this range. Previous studies reported general observations of size-based particle separation in vortical laminar flow formed in T-junction [121], tubular sudden expansion [67] [68] and cavity flow [83] [138]. We chose MDA-MB-231 breast cancer cell line to model rare cell capture. It is the most challenging CTC to capture due to heterogeneous receptor expression. This made labeling with immunoaffinity techniques obsolete. More importantly, it is relatively smaller than CTCs and there is a size overlap with WBCs. In this work, we show a novel method of exploiting microvortex selective trapping phenomena to engineer tunable size-based capture. A single device geometry can isolate an expanded size range of cells by only switching flow conditions. We were able to find critical Reynolds numbers to capture and enrich small cells, large cells, and cell clusters. Our approach opens a new platform for tunable on-chip separation and enrichment of target cells. This facilitates automated bio-fluid processing for many on-chip applications and downstream analysis.

1.2 Methods

1.2.1 Device fabrication

A straight rectangular channel ($H_{ch} = 70\ \mu m$, $W_{ch} = 40\ \mu m$, $L_{ch} = 3$ cm) was formed from a master mold fabricated via standard soft photolithography. KMPR 1050 (Microchem) photoresist is used for this process. Trapping reservoirs were

placed 1 cm away from the inlet of the rectangular channel. In addition, cavities with different aspect ratios (AR = 1, 2 and 3) and channel expansion ratios were designed. All cavities are made of the same height ($H = 70\ \mu m$) to unify the generation of axial flow. PDMS elastomer and curing agent (Sylgard 184, Dow Corning, Midland, MI) were mixed at ratio 10:1 and poured onto the master mold and degassed for 60 min to remove all trapped bubbles. The master mold was placed in a 68 C oven for 24 hours to thoroughly cure the PDMS. The cured PDMS replica was peeled away from the master mold. Inlet and outlet holes were punched in PDMA replica and irreversibly bonded to a glass slide by exposing both PDMS and glass surfaces to O_2 plasma for 37 s, at 500 mTorr, 80 W power (Harrick Plasma, Ithaca, NY).

1.2.2 Device Operation

Particles suspension were pumped into the device using a syringe pump (Harvard Apparatus, Holliston, MA, USA) through polyetheretherkertone (PEEK) tubing (Upchurch Scientific). The device was primed with PBS buffer for 1 min to form vortex topology in different flow rates ranging from (100-1000 $\mu L/min$). The fluid was collected at the end of the chip in a new capped syringe for reruns. To avoid particle sedimentation, syringes with a suspension were mixed and changed in each run to keep the uniform distribution of particles. The number of cells passing over the cavity was normalized across different flow rates to get only 1000 cells to pass over the cavity in the entrapment study.

1.2.3 Image Analysis

The cavity was viewed using a microscope (Nikon Ti- U) illuminated by a mercury arc lamp with 10x objective of an effective pixel size of 2 μm. A high-speed camera Phantom V2010 camera (Vision ResearchInc., Wayne, NJ, USA) recorded

at 10 000 frames per second for characterizing equilibrium orbits and 30 frames per second for analyzing long term behavior of particle motion inside the cavity. In-house image processing code was developed in MATLAB to identify sizes of trapped particles and track particle motion in the cavity. The fluorescent images were captured by a CCD Coolsnap HQ2 camera (Roper Scientific, Evry, France), then processed by Zen2 software. Cells that are not intact were excluded from the study.

1.2.4 Particle and Cell suspension

Fluorescent polystyrene particles with a mean diameter of 10, 15, 20, 30 μm were from (Phosphorex, Hopkinton, MA). Tween 20 (Sigma-Aldrich, product No. P9416) was added with 0.1 % to prevent aggregation. MCF-7 (30-2004, ATCC, Manassas, VA) and MDA-MB-231 (ATCC 30-2002) were cultured in DMEM medium (ATCC 30-2002). Medium is supplemented with 10% fetal bovine serum (Invitrogen, Carlsbad, CA) and 1% penicillin-streptomycin (Invitrogen, Carlsbad, CA) at 37 °C under 5% CO2 conditions. Cells were passaged once they reach 80% confluence. Cells and medium tested negative for mycoplasma. Cells were fluorescently labeled with 0.1 propidium iodide AM (Invitrogen, Carlsbad, CA) for viability test and CellTracker for tracking cell motion inside the cavity. In addition, cell were stained with final concentrations of 0.005mg/ml DAPI (40,6-diamidino-2-phenylindole, Molecular Probes) and 0.05 mg/ml anti- CD45-PE (BD Biosciences, HI30) in blood spiking experiments. MDA-MB-231 GFP expressing cells which we will refer to as (MDA-GFP), were spiked in whole blood and diluted in PBS by a factor of 20x. Stained cells were defined in (Fig. 1.3). Whole blood samples from healthy donors were obtained from UCLA in venous blood collection tubes containing EDTA (Vacutainer, BD Biosciences, San Jose, CA).

1.2.5 Simulation

We modeled the device using a simulation software COMSOL Multiphysics (COMSOL, Burlington, MA) to quantify the stabilized streamlines and velocity distribution of a microvortex flow. The flow rate was set from 100-1000 $\mu L/min$. The physical properties of water was applied to the fluid in the simulation (density ρ = 1000 kg m^3 and dynamic viscosity $\mu = 10^3$ kg $m^{-1}s^{-1}$). The velocity of magnitude (ms^{-1}) is calculated from the flow rate applied in the inlet velocity. We analyzed simulation results to locate vortex core by finding velocity minimum within cavity flow.

1.3 Results and discussion

1.3.1 Particle Migration to Microvortex Flow

Before describing particle motion and separation in the cavity, we explain important parameters that influence particle transition from the main channel to the open cavity. Inertial flow is described in terms of Reynolds number, which is controlled by varying flow rate Q ($\mu L/min$) in a pressure-driven pump system. The Reynolds number of the system is defined by the flow in a rectangular channel (Re= $\rho U D_{\mathrm{h}}/\mu$). Here ρ, U and μ correspond to density, inlet velocity and kinematic viscosity of the fluid, respectively. D_{h} is the hydraulic diameter of the channel, defined as ($D_{\mathrm{h}} = 2(W_{ch}H_{ch})/(W_{ch} + H_{ch})$), where H_{ch} and W_{ch} are channel height and width respectively. At finite Reynolds number, suspended particles in bounded conditions experience two counteracting forces [107]. These forces control particle lateral migration in the channel of Newtonian fluid shear gradient lift force (F_{LS}) pushes the particle towards the channel wall, while the wall induced lift force (F_{LW}) directs the particle towards the channel centerline. Particles migrate certain distance to reach an equilibrium position [32][34] [33].

The inertial lift forces are simplified as the following ($F_{\mathrm{LS}} = f_{\mathrm{L}}\rho U^2 a^3/W_{ch}$) and ($F_{\mathrm{LW}} = f_{\mathrm{L}}\rho U^2 a^6/W_{ch}^4$), where ($f_{\mathrm{L}}$) is the dimensionless lift coefficient and (a) is the particle diameter (μm).

Particle experience different magnitudes of hydrodynamic forces based on their size. Particle size is scaled in relation channel minimum width (W_{ch}). Particle confinement ratio (λ) was set ($\lambda = a/W_{ch}$). The channel was designed in such all particles, cells and cell clusters to reach equilibrium positions before passing over the cavity. Channel aspect ratio ($AR = H_{ch}/W_{ch}$) is 1.75 to align particles laterally in the midsection of each wall [79] [60].

1.3.2 Microvortex Size-Based Radial Seperation

In this section, we explore long term behavior of neutrally buoyant particles inside microvortex flow after entrapment. Vortical flow inside the cavity is strongly influenced by the characteristics of the main channel flow (Re). At very low Reynolds number ($Re \sim 10$), fluid flow passes symmetrically through the cavity with no recirculation. [129] (Fig. 1.4). Moffat eddies are formed in the leading wall corners at slightly higher flow rates [88]. Particles pass through the cavity with no entrapment in this regime. However, under inertial conditions ($Re \sim 70$), the flow separates from the main channel due to the jetting effect at the channel expansion region. Microvortex formation has been described extensively in previous studies [64] [83]. In the sudden expansion-contraction region, particles are driven into the cavity due to the absence of wall-induced lift force (F_{LW}). Some particles join the recirculating fluid flow, however, not all are maintained in the cavity (i.e. short residence time).

We found a connection between vortical flow properties and their trapping dynamics through tracking finite size particle motion over open cavities. Under the same flow conditions, particles settle in separate equilibrium orbits based on their

size in microvortex flow. When changing the flow rate, equilibrium orbits change their radius. We tracked the motion of polystyrene beads in the cavity at different flow conditions. Each flow rate forms a unique vortex topology with size-specific capturing properties. To systemically understand size-based orbital separation process, we transform the particle motion from cartesian coordinates to polar coordinates in order to find a universal metric for this behavior. Two-dimensional particle trajectory [$x_p(t)$,$y_p(t)$] were translated to average orbital radius (O_r) :

$$O_r = \sqrt{[x_p(t) - x_0]^2 + [y_p(t) - y_0]^2} \tag{1.1}$$

Vortex core coordinates x_0 and y_0 are set as the reference point of the system (Fig. 1.4b). The vortex core coordinated was set by the local velocity minimum within the cavity boundaries x-y cross-sections along the y-axis. (Fig. 1-4c). There was a small shift in vortex core coordinates from experimental study due to PDMS deformation.

We segment beads and cells to different sizes ($\lambda = 0.1, 0.5, 1$) and calculate their average orbital radius in the cavity at different flow rates. At low inertial conditions, large particles ($\lambda > 0.5$) settle in small equilibrium orbits near the vortex core. However, small particles ($\lambda \leq 0.5$) orbit around the vortex boundary further away from the vortex core. Accelerating the flow rate, small and large particles switch their proximity to the vortex core. We describe more in details the progression phases of this phenomena (Fig. 1.5), in which average orbital radius (O_r) change in correlation to a range of inertial flow conditions defined by Reynolds number (Re):

1.3.2.1 Phase I

The first set of Reynolds numbers where vortical microflow generate ($100 < Re < 175$), vortex core is formed near the leading wall then shift to the middle of the

cavity. Large particles spiral inward migrating toward the vortex core, leading to a decrease in their orbital radius. However, small beads settle in orbits away from vortex core and near cavity walls (Fig. 1.5a) with larger orbital radius $[O_r(\lambda < 0.5) > O_r(\lambda > 0.5)]$ (Fig. 1.5b). Particle-wall interaction with leading and trailing wall is minimal after entering the cavity. Particles with large orbital radius circulate near the cavity wall. They are unstable and exit the cavity over time or small flow fluctuations.

1.3.2.2 Phase II

Increasing the flow further to Reynolds number ($175 < Re < 225$), vortex core dead space takes over the cavity pushing both large and small beads outward. In this case, large and small beads share the same orbit trajectory away from vortex core and near vortex boundary $[O_r(\lambda < 0.5) \simeq O_r(\lambda > 0.5)]$. Particle loading and accumulation in the cavity is limited due to narrow trapping space. Large particles dominate the trapping space in this phase.

1.3.2.3 Phase III

Interestingly, at high Reynolds number ($225 < Re < 300$), an inversion occurs. Small beads orbit near vortex core while large beads migrate outward near cavity walls $[O_r(\lambda < 0.5) < O_r(\lambda > 0.5)]$. Vortex core shift from the center of the cavity to the trailing wall. To further investigate on radial separation phenomena in the cavity, we experimentally studied the trapping dynamics of a polydispersed solution of particles. Equal fraction of 30, 20, 15 and 10 μm polystyrene beads suspension were passed over the cavity in all trapping phases (Fig. 1.5 d). The scatter plot of the particle size distribution in the cavity and average orbital radius agrees with the observation in single particle trajectory analysis of the previous section (Fig. 1.5e). A plot of the average orbital radius (O_r) of polydispersed

beads shows the switch in equilibrium orbit's proximity to the vortex core after phase II (Fig. 1.5f).

1.3.3 Tunable Size Selective Capture of Cells

Cells exhibit the same size-based radial migration as beads. In addition, we observed the same pattern of cell radial migration as a function of the cavity aspect ratio ($AR = 1, 2, 3$. We tested the size-selective capture properties of MDA-MB-231 breast cancer cells under different microvortex flow conditions (Fig. 1.6 a-c). At early stages of phase I, cell clusters $\lambda \geq 1$ are steadily trapped in the vortex core with $O_r = 0$. Large cells dominate tapping orbits in phase II. Lastly, in phase III, small cells self-assemble in orbits near the vortex core and large cells settle near the vortex boundary (Fig. 1.6b). The scatter plots of cell size distribution over multiple experiments are shown for the three phases and ($AR = 2$) (Fig. 1.6c). The same radial separation of beads for ($AR = 1$) is observed (Fig. 1.7). Moreover, the average orbital radius (O_r) of cells in ($AR = 1$) matches the beads results over all three phases (Fig. 1.6d). This implies that deformability differences do not play a significant role in the size-dependent inversion of the orbital radius. We investigated the relationship between inward radial migration switch with the effective capture size of cells (Fig. 1.6e). The mean cell-size of captured cells is significantly shifted when the orbital radius becomes smaller. Each vortex flow condition possesses a different capture distribution of cells. The total number of captured cells per cavity agrees with the results from a previous study [110]. The microvortex flow at Re = 150 has the highest number of captured cells but a low size specificity.

To investigate further, we compared the capture and loading capacity of two different breast cancer cell lines with different size distributions (MCF-7 and MDA-MB-231). We found the optimal capture phase for each cell line, Phase I for MCF-7 and Phase III for MDA-MB-231 (Fig. 1.8). This result suggests

that the capture and loading capacity of microvortex flow in phase I and III is size-selective.

1.3.4 Rare cell capture in blood

From previous findings, we defined a critical Reynolds number above which cells of certain diameter have attractive stable orbits towards the vortex core. Also, we found the local capture efficiency maximum of each phase. Here, we tested the contribution of size-based orbit selectivity in trapping all sizes of MDA-GFP cells from blood in one device. We spiked 1000 MDA-GFP cells in blood samples with optimal conditions for trapping small cell ($\lambda < 0.5$) in phase III (Re = 275) and large cells and clusters ($\lambda > 0.5$) in phase I (Re = 125) described in the methods section. We passed the sample three times with phase I flow conditions and three times later with phase III flow conditions (Fig. 1.11a) and vice versa (Fig. 1.11b). Each trapping cycle shows consistent size-selective capture. In addition, recycling the sample improved the efficiency of capture. Captured cells were released on-demand by stopping the inlet flow for enumeration and size distribution. We found the same bias in captured cell size according to each phase (Fig. 1.11c). Size distribution of cells collected in the outlet show statistically significant difference of target cell mean size between phase I ($Re = 125$) and phase III ($Re = 275$) ($p - value < 0.00001$; $\alpha = 0.01$).

We were able to obtain spiked cells from both flow conditions while maintaining scalable efficiency (Fig. 1.10) and high purity and cell viability and functionality (Fig. 1.9). Increasing sample purity enables improved downstream molecular diagnostics. Cell viability and functionality enable drug development.

1.4 Summary

In this work, we report a new multimodal size-based membraneless filter which enables long-term trapping of rare cells from complex suspensions in confined cavity flow. This enables on-chip testing and analysis of polydisperse cells of all sizes within the same device. The flow-based switch changes the flow morphology of vortical flow acquiring different trapping properties. We described radial separation phenomena in confined vortical flow. For future work, we intend to investigate more on capturing dynamics and generalize a capturing method of any particle size under the realm of continuum mechanics. As for applications, we intend to scale up the system with multiple capturing units to achieve higher device capture efficiency. Captured target cells can be released on demand to improve profiling and characterization of rare cells.

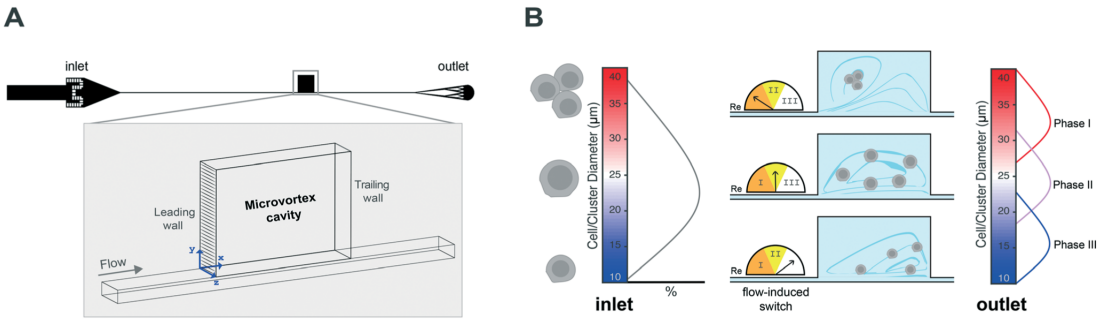

Figure 1.1: Microfluidic device principle and operation. (a) Schematic of a single-channel device with an upstream filter to prevent debris from blocking the channel. Downstream flow divider and diffuser to prevent backflow and capture of cells at the outlet. Micro-cavity was placed 1 cm from the inlet. Microvortex flow form between leading and trailing walls of the cavity at high Reynolds number. (b) Polydispersed rare cells (clusters, large and small cells) are captured by different microvortices generated in the same device. Inertial flow conditions (Re) are tuned to generate a distinct vortical flow geometry with specific capturing properties: Phase I ($Re = 100 - 175$) capture clusters, phase II ($Re = 175 - 225$) capture large cells and phase III ($Re = 225 - 300$) capture small cells

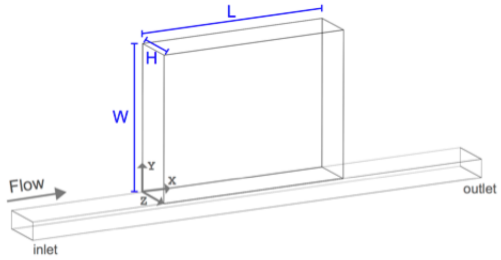

Aspect Ratio AR = L/W	Length (L) (μm)	Width (W) (μm)	Height (H) (μm)	Channel Expansion Ratio ER = W/W_{ch}
1	930	930	70	23.25
2	930	465	70	11.625
3	930	310	70	7.75

Figure 1.2: Microfluidic device geometry and trapping reservoir (cavity) dimensions. Different cavity aspect ratios (AR) are designed to test radial migration of particles in microvortices. Cavity length (L), width (W) and height (H) are along the X, Y and Z directions respectively. Cavity is placed 1 cm away from the inlet. All cavities are made of the same height (H = 70 μm.). Rectangular channel width (W_{ch}) is 40 μm and channel height (H_{ch}) is 70 μm.

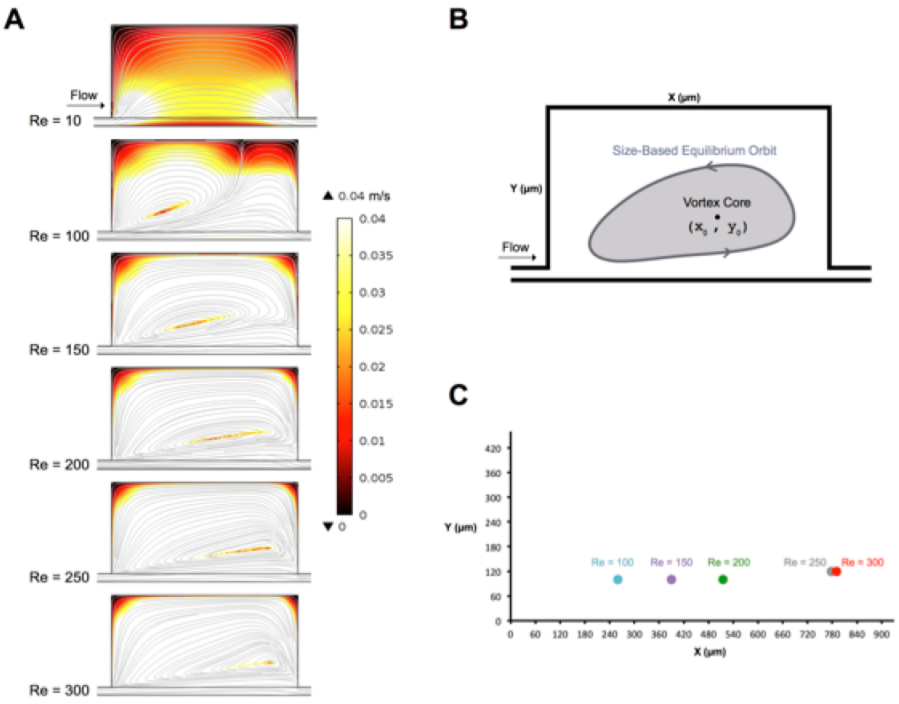

Figure 1.3: Microvortex core characterization. (a) COMSOL Multiphysics model of velocity distribution in microcavity (AR =2) recirculation region. Different vortex topologies generated at different inertial conditions defined by the mean-flow Reynolds number (Re) in a rectangular channel. Vortex core was identified by the local velocity minimum inside the cavity at different flow rates. (b) Schematic illustration of x-y plane of the cavity and location of vortex core (x0, y0). (c) Vortex core coordinates along x-axis in the cavity at Reynolds number (Re) 100, 150, 200, 250 and 300.

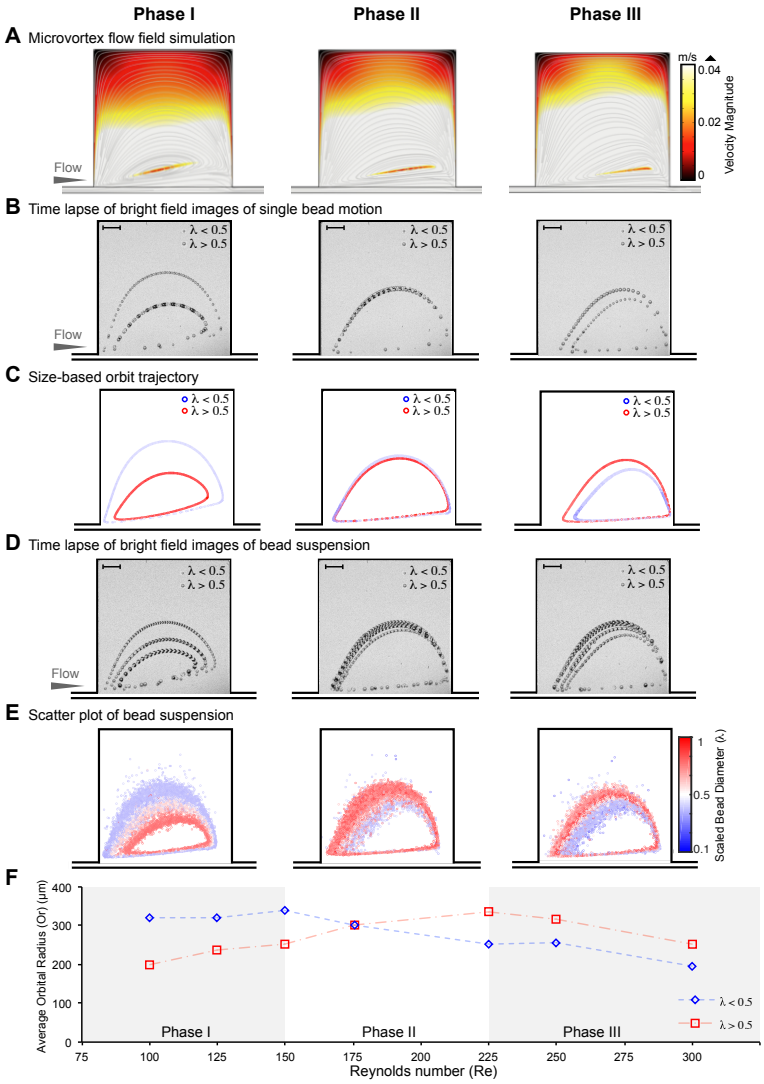

Figure 1.4: Radial migration phenomena description at different inertial flow conditions (Re): Each three columns of images (a-e) represent an example of an inertial flow condition in phase I ($Re = 100 - 175$), phase II ($Re = 175 - 225$) and phase III ($Re = 225 - 300$). (a) Flow streamlines (grey lines) and velocity distribution (color contours) of laminar vortical flow in the cavity with aspect ratio ($AR = 1$) at $Re = 150$, 200 and 300. The color scale represents the velocity magnitude (m/s). We specified the range of velocity magnitude were it saturates at (0.04 m/s) to show the vortex core of each microvortex flow. (b) Time-lapse of high-speed image of single polystyrene particles show the transition of equilibrium orbits in each capture phase. (c) Particle tracing inward radial migration switch between large particle ($\lambda > 0.5$) (red) and small particle ($\lambda < 0.5$) (blue). (d) Bright field images captured with high-speed recording of polystyrene particle suspension illustrates their motion transition between phases. All scale bars represent 120 μm. (e) Scatter plot of polydisperse polystyrene beads illustrate orbital transition towards vortex core between phase I and phase III. The color scale represents scaled bead diameter (λ). (f) Average orbital radius (O_r) of polydisperese beads over different inertial conditions (Re) illustrates the switch of size-dependent orbital radius in different flow rates.

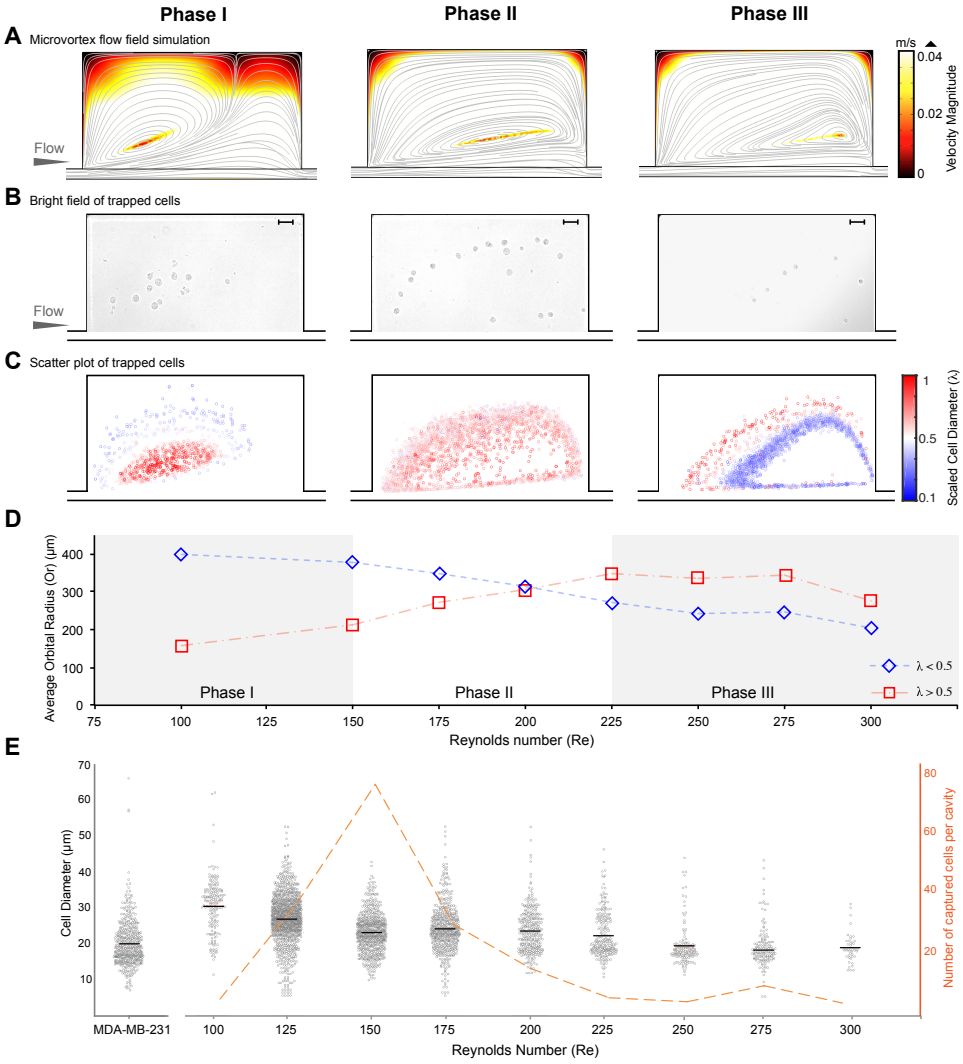

Figure 1.5: Relationship of size-dependent vortex capture and average orbital radius of cells. Each three columns of images (a-c) represent an example of an inertial flow condition in phase I ($Re = 100 - 175$), phase II ($Re = 175 - 225$) and phase III ($Re = 225 - 300$) (a) Flow streamlines (grey lines) and velocity distribution (color contours) of laminar vortical flow in cavity with aspect ratio ($AR = 2$) at $Re = 100$, 200 and 300. The color scale represents the velocity magnitude (m/s). (b) MDA-MB-231 cell lines self assemble in different size-selective trapping phases. All scale bars represent 60 μm. (c) Size distribution scatter plot of tracked cells inside microvortex flow from different experiments. The color scale represents scaled cell diameter (λ). (d) Average orbital radius O_r of polydisperese cells over different inertial conditions (Re) show the switch in size-based equilibrium orbits after phase II. (e) MDA-MB-231 cell line size distribution and captured cells in different Reynolds number (Re). Each Reynolds number form a micro-vortex with specific capture efficiency. Plot of single capturing unit (one cavity) efficiency (secondary axis on the right)

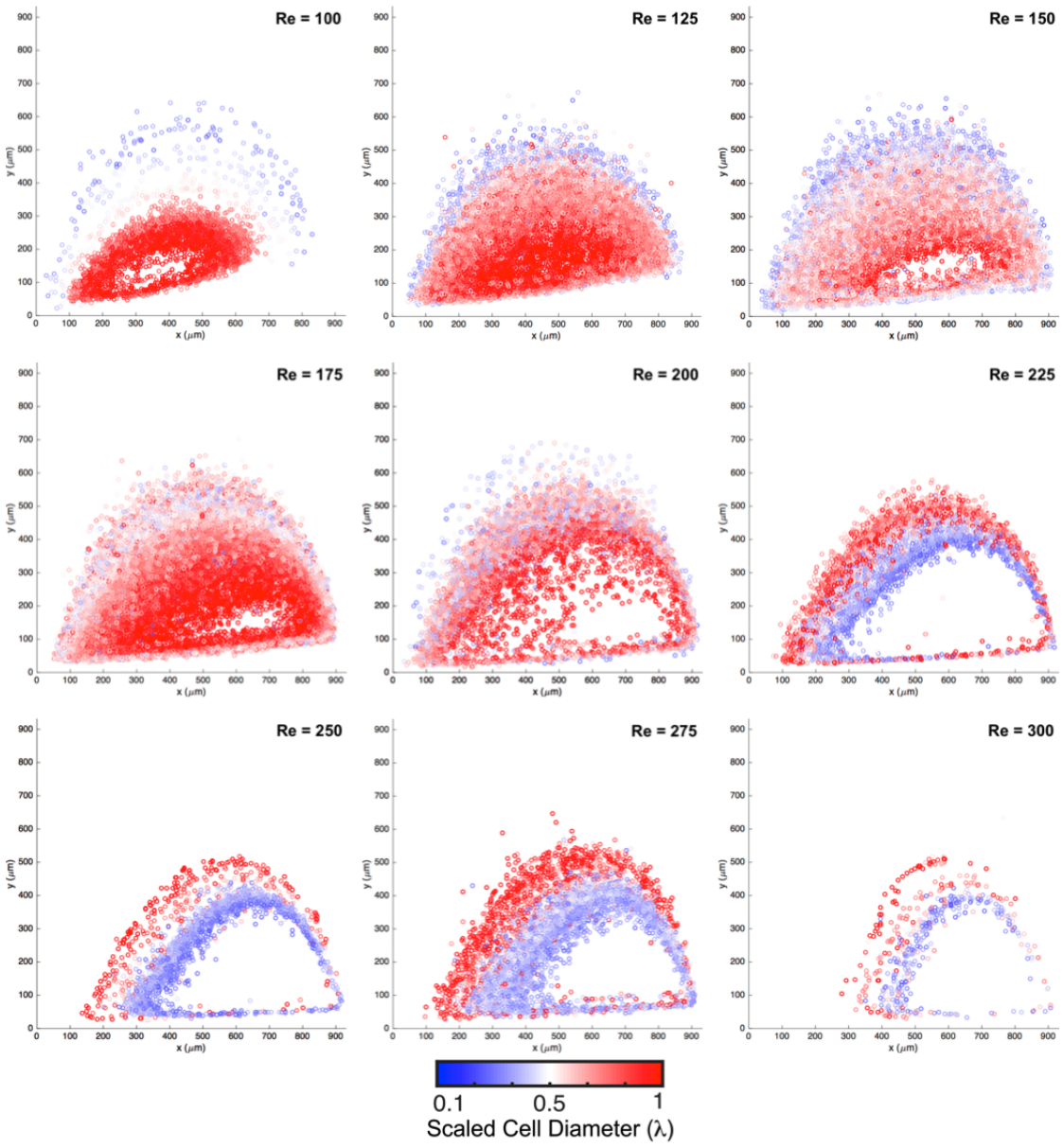

Figure 1.6: Scatter plot of captured cells size distribution and their orbit trajectories in AR = 1 cavity. Cell motion and progression in micro-vortices illustrates size selective orbit transition in increasing flow conditions at Reynolds number (Re) 100, 125, 150, 175, 200, 225, 250, 275 and 300.

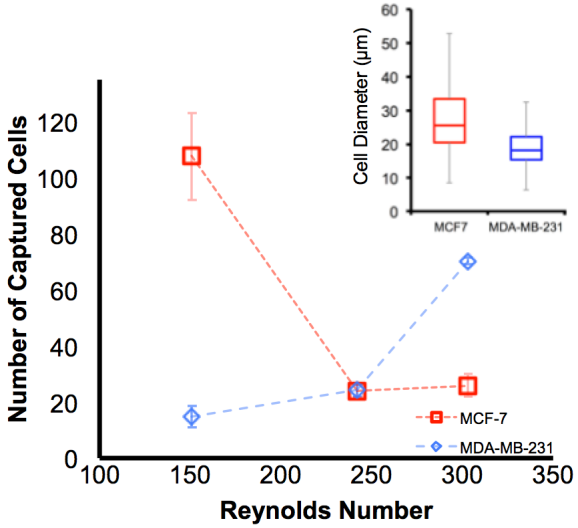

Figure 1.7: Microvortex loading capacity for MCF-7 ($\lambda > 0.5$) cells) and MDA-MB-231 ($\lambda < 0.5$). Flow of concentrated cell suspension for five minutes followed by PBS wash for five minutes in three inertial conditions at Re = 150, 240 and 300. Microvortex capture of MCF-7 with mean cell diameter = 25 μm and MDA-MB-231 = 18 μm show size-selective capacity in phase I (Re = 150) and phase III (Re = 275) respectively.

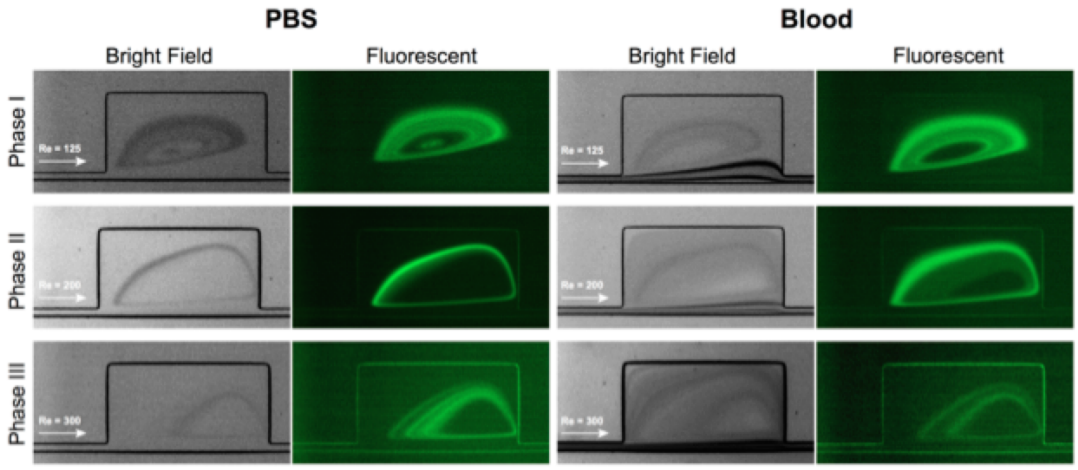

Figure 1.8: Captured MDA-GFP orbit trajectories in microvortex flow with PBS and blood. Bright field (left) and fluorescent (right) images of PBS and 20x diluted blood spiked with MDA-GFP cell lines in microvortex flow show consistent orbit trajectories. Fluorescently labeled cancer cell line MDA-GFP orbit trajectories observed in phase I (Re = 125), phase II (Re = 200) and phase III (Re = 300).

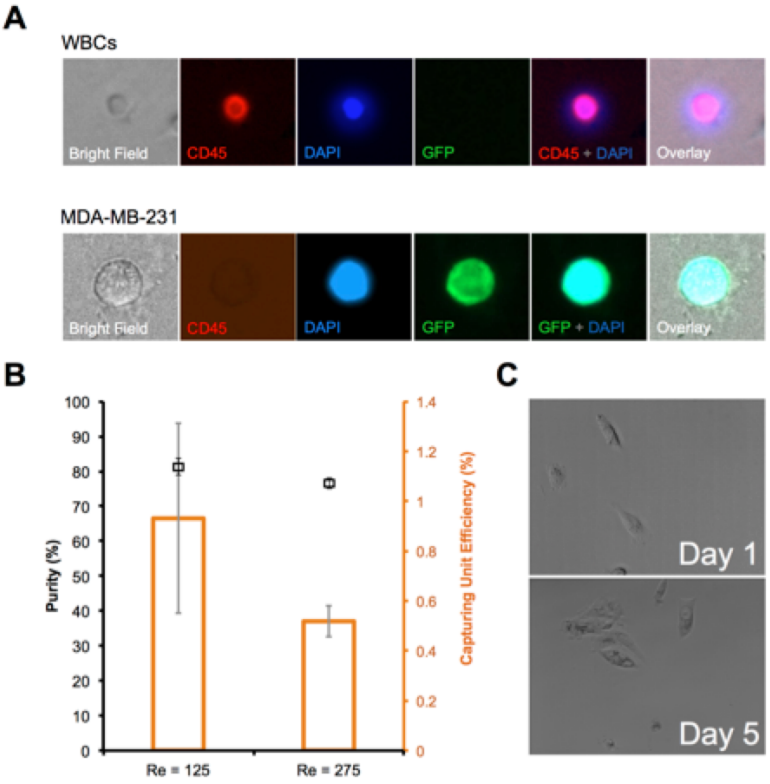

$$\text{Purity (\%)} = \frac{\text{Number of Target cells captured}}{\text{Total number of cells captured}}$$

$$\text{Capturing unit efficiency (\%)} = \frac{\text{Number of cells captured in the cavity}}{\text{Total number of target cells passed over one cavity}}$$

Figure 1.9: Device performance of rare cells capture from blood samples. (a) Immunofluorescent staining and classification criteria. Collected cells were classified according to immunostains against GFP (green) and CD45 (red), as well as DNA stained with DAPI (blue). MDA-GFP cells are identified as GFP+/CD45-/DAPI+ and WBCs as GFP-/CD45+/DAPI+. (b) Purity and capturing unit efficiency of collected MDA-GFP spiked in blood. (c) Cells released from microvortex flow are able to grow and proliferate after 4 days.

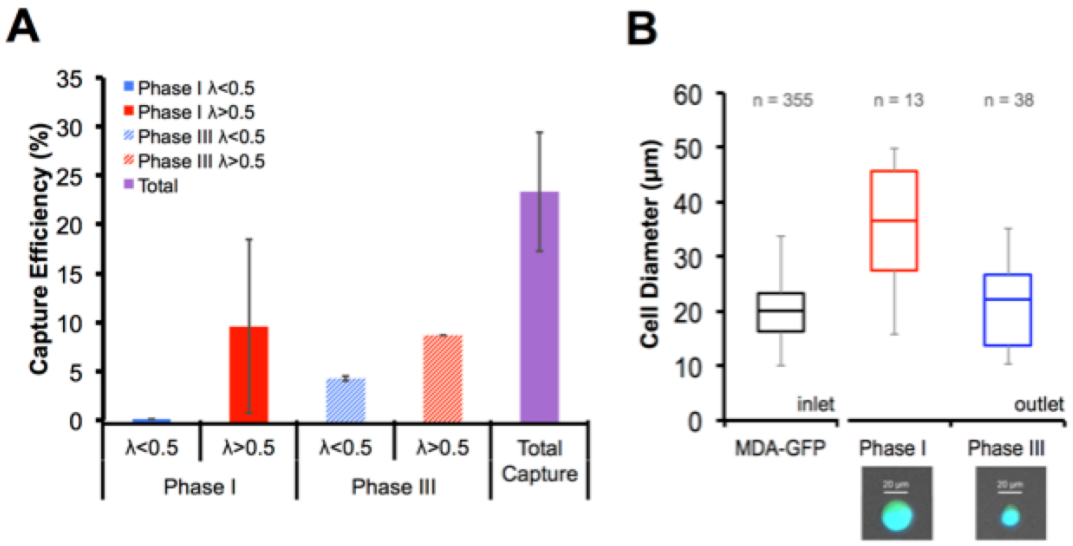

$$\text{Capture Efficiency (\%)} = \frac{\text{Number of target cells captured}}{\text{Total number of target cells passed } (\lambda < 0.5 \text{ or } \lambda > 0.5)}$$

Figure 1.10: Vortex HT device capture efficiency and size selectivity for MDA-GFP in blood. Isolation and capture of MDA-GFP cells spiked in 20X diluted blood were tested on a High-Throughput vortex device under phase I and phase III flow conditions. (a) The captured MDA-GFP population were segmented to large cells with diameter (a $>$ 25 μm, $\lambda > 0.5$) and small cells (a $<$ 25 μm, $\lambda > 0.5$). Phase I shows high capture efficiency for large cells ($\lambda > 0.5$) while phase III shows high capture efficiency for small cells ($\lambda < 0.5$). (b) The size distribution of captured cells from phase I and III, shows a consistent size selectivity for each flow condition with the vortex device.

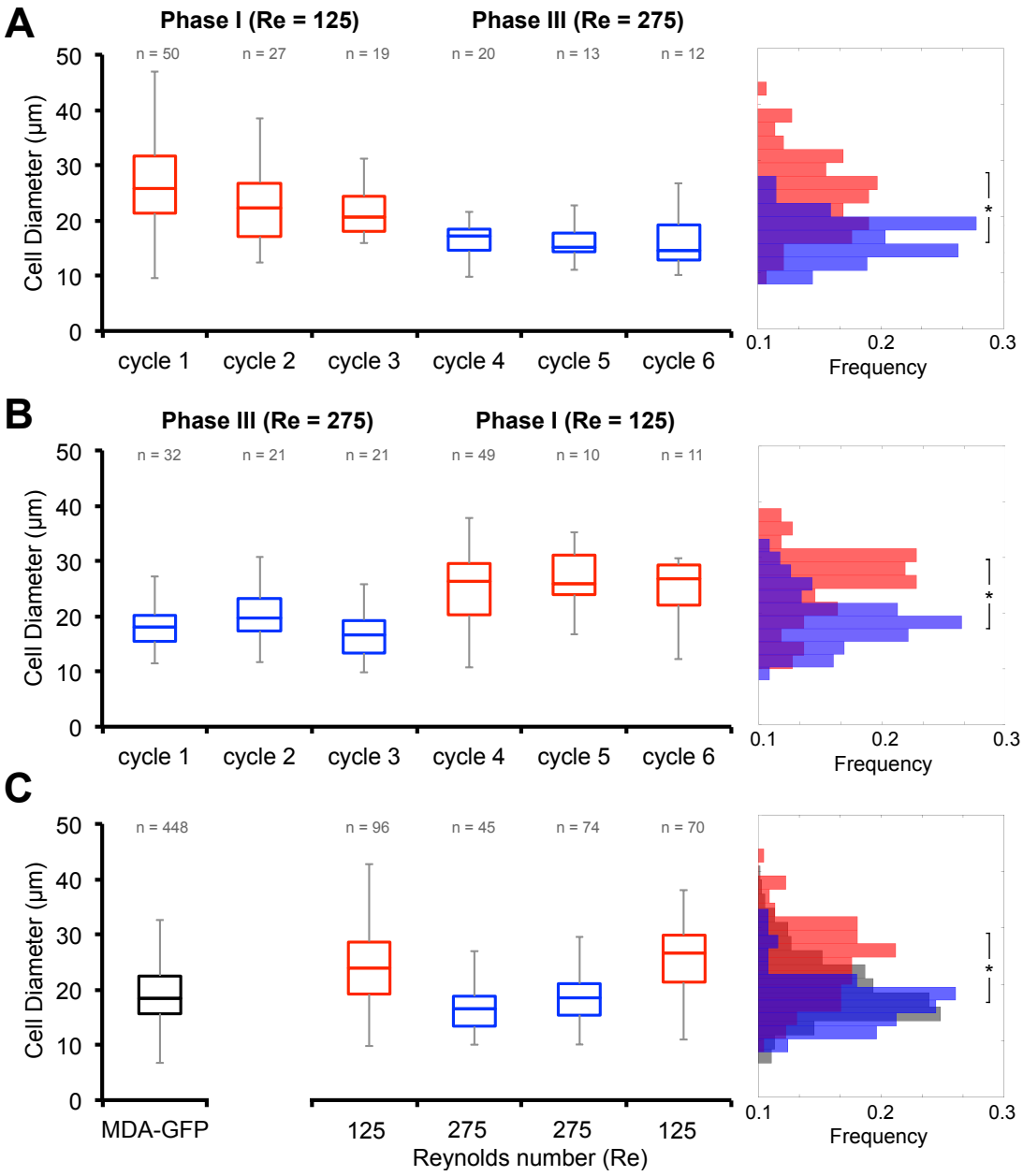

Figure 1.11: Size-based capture characterization of rare cells from the blood. (a) The size distribution of MDA-GFP isolated from blood starting phase I (Re = 125) flow conditions followed by phase III (Re = 275). The blood sample was recycled in the device in each phase. (b) The size distribution of isolated cells starting phase III (Re = 275) followed by phase I (Re = 125). (c) Captured cells in both phases and in different order show a significant difference in cell size distribution. Both phase I (Re = 125) (red) and phase III (Re = 275) (blue) are necessary to capture all MDA-MB-231 size distribution (grey). (*) p-value = 0.0001.

CHAPTER 2

3D Confined Microcavity Flow

2.1 Introduction

When flowing fluid with finite inertia in a channel that suddenly expands in cross-sectional dimension, an adverse pressure gradient can occur resulting in the formation of recirculating flow in the expansion region [9, 82, 8]. If the cross-sectional dimension is returned to the initial value further downstream, this creates a cavity, which can support a recirculating flow up to the cavity size [108]. The formation of recirculating flows in 3D-confined cavities can result in selective particle capture from the mainstream channel flow [64], an area attracting significant excitement for cell and particle separation and sorting [71]. For example, microcavities have been utilized in miniaturized diagnostic devices as well-controlled reaction chambers for trapped bio-particles [84, 48, 83]. Cavity flow capture phenomena also appear relevant in the assembly of biological self-replicating molecules in microvortices that arise in porous ocean rocks in the prebiotic era [113], as well as in micro-clot accumulation in aneurysms [103]. A better understanding of the conditions that give rise to recirculating confined cavity flows and mass transport into such cavities can help address a wide range of vortex capture phenomena. However, it has been challenging to visualize or predict the formation and growth of complex recirculating flows unfolding between channels and side cavities, especially in three-dimensional confined conditions. For example, unexpected complex flow patterns generate in 3D wall confined microchannels [6] and T-junctions [121].

Incompressible and unconfined (2D) cavity flow has been extensively studied in which the formation of a material flux boundary, or separatrix, between the main channel flow and open cavity flow is a defining feature [47, 86, 61, 94]. In contrast, for confined conditions, recirculating inertial flow is highly complex and un-folds in a qualitatively different manner in three-dimensional space [75]. Early phases of vortical flow formation in a confined 3D cavity has similar fluid physics to that of flow through a sudden expansion or backward facing step at low Reynolds numbers [14]. However, without the existence of a trailing wall to confine the flow laterally, secondary and tertiary separation bubbles occur downstream in the later stages of such flows [36, 7]. In the presence of the trailing wall, the recirculating wake grows and occupies the entire cavity where new flow structures occur at later stages of cavity flow development. Previous numerical studies on full cavity flows indicated that the recirculating wake could not be thought to contain a separatrix, as the flow from the mainstream is coupled to the recirculating cavity flow without a mass flux boundary [118, 54]. The enhanced mass transport coinciding with separatrix breakdown appears to be amplified at later stages, potentially resulting in reduced particle capture as outward fluid fluxes from the cavity dominant particle motion [55]. In this study, we experimentally determine how cavity flow development is coupled to separatrix breakdown and enhanced convective mass transport into the cavity.

2.2 Methods

2.2.1 Experimental methods

Device fabrication is described in detail in the previous chapter 1. Experiments were performed in a square cavity with a range of side lengths (X_s = 100-1000 μm), heights (H = 40-150 μm) and channel widths (40 and 100 μm). To follow the empirical formulation stated above (H/X_s), the flow was observed with fluores-

cent particle tracers in (x,y) plane with volumetric fraction $\Phi = 0.0001$. Cavity flow morphology in two-dimensional space was observed using Nikon Ti eclipse inverted microscope and CCD camera. The flow was recorded with 5 seconds increment to track the reattachment point transition along the cavity wall. The reattachment point develops and stabilizes after one minute of changing the flow rate (Fig. 2.4). Since PDMS devices are prone to expand with pressure and since the pressure is not equally distributed along a Poiseuille channel flow, we tested cavity flow progression at different locations along the channel. The location of the cavity along the channel had a negligible contribution to the development of cavity flow as the reattachment point measurements were similar (Fig. 2.8). Leica Confocal SP5 Blue microscope was used to visualize how cavity flow unfolds in a three dimensional confined space. The cavity flow development was recorded as a function of the reattachment point transition on the cavity wall. High spatial resolution images in the (x,y) plane were taken with 0.4-1 μm increment along the z-plane. Fluorescent dyes (Green: Fluorescein isothiocyanate Dextran, Red: Rhodamine B isothiocyanate Dextran) were injected in one of the four inlets upstream the channel to dissect the flow streamlines from the main channel that enter and spiral out of the cavity. Laminar streamlines from incremented initial locations of different inlets in the main flow were observed inside the cavity under different flow conditions and cavity geometry.

2.2.2 Numerical Simulation

Finite element software (COMSOL Multiphysics) was used to simulate vortex growth in cavity flow. Navier-stokes equation was solved for incompressible flow were no-slip condition is set to the channel and cavity walls. The flow rate was set from 100-1000 $\mu L/min$ and cavity geometry range 100-1000 μm. The physical properties of water was applied to the fluid in the simulation (density $\rho = 1000$ kg m^3 and dynamic viscosity $\mu = 10^3$ kg $m^{-1}s^{-1}$). The velocity of magnitude

(ms^{-1}) is calculated from the flow rate applied in the inlet velocity. We analyzed simulation results to locate vortex core by finding velocity minimum within cavity flow and the y-intercept of fluid velocity near the cavity wall to locate the reattachment point.

2.2.3 Scaling arguments

Through experimental and dimensional analysis we seek to establish a correlation between the reattachment point (x) as observed from a top-down perspective, and the critical states of mass transfer in cavity flow. Giving the fluid physical properties in the flow set up, Buckingham's pi theorem requires four independent dimensionless parameters to describe cavity flow behavior. Dimensionless groups expressing three shape parameters, the location of attachment point (x) in relation to the cavity side length (X_s) : (x/X_s), cavity aspect ratio with the cavity height (H) : (H/X_s), channel expansion ratio with the channel width (W) : (W/X_s) and lastly the ratio of inertial to viscous forces expressed in the Reynolds number (Re) of the channel flow above the cavity (Fig. 2.2a). Flow in the channel is defined by the Reynolds number (Re) as $Re = \frac{uH_d}{\nu}$, where u is the average velocity of the parabolic profile, H_d is the channel hydraulic diameter, and ν is the kinematic viscosity of the fluid. We next investigate the empirical and functional relation

$$\frac{x}{X_s} = f(\frac{H}{X_s}, \frac{W}{X_s}, Re) \tag{2.1}$$

The development of the reattachment point (x) is generalized by normalizing the transition over the sum of all cavity side walls. Our approach is to follow the development of flow separation and reattachment from the sudden expansion of the leading wall (x_1). The reattachment point (x) translates to the cavity side wall parallel to the channel wall (x_2). Lastly, stabilizes at the end of the trailing wall (x_3) in which the vortical flow saturates the cavity (Fig. 1.A). We assume

that all cavity side lengths ($\sum x_{i=number\ of\ side\ walls}$) starting from the leading wall (x_1), side wall (x_2) and trailing wall (x_3) are equal to cavity side length (X_s). The attachment point locations are divided by the sum of all cavity lengths $\sum X_s = \sum x_i = (x_1+x_2+x_3)$. This strategy generalize cavity flow characterization through the dimensionless parameter of the normalized reattachment point ($x* = \frac{x}{\sum x_i}$) on cavity walls of any length (Fig. 2.2b).

2.3 Results and discussion

2.3.1 Recirculating cavity flow formation and logistic growth

In a channel-cavity system with fixed channel flow conditions ($Re = \rho u D_\mathrm{h}/\nu$), where u is the average inlet flow velocity, D_h, hydraulic diameter of the channel, and mu is the kinematic viscosity of the fluid, the recirculating cavity flow develops in a square cavity as a function of the cavity height (H) and cavity side length (X_s) (Fig. 2.1). Thus, it is challenging to define and generalize conditions for recirculating flow formation in microcavities. However, one common defining characteristic shared by all cavity geometries is the transition of the reattachment line at which streamlines diverge along the stationary cavity wall [26](Fig. 2.2). The reattachment point (x^*) as observed from a top-down perspective, is a good surrogate for the reattachment line. The transition of the reattachment point can be rescaled to the sum of the side lengths (X_s) of a square cavity ($x^*=\frac{x}{\sum X_s}$), which can be generalized to different cavity geometries, and directly linked to the development state of recirculating flow in the cavity.

The evolution of the reattachment point in microcavity ($X_s = 250\mu m$, $H = 70\mu m$) was explored as a function of the channel's Reynolds number ($Re = 0.1 - 100$). At low Reynolds number, fluid flow passes with fore-aft symmetry through the cavity, as expected for Stokes flow, with no recirculation ($x^* = 0$). Flow separates at higher Reynolds number creating a circulating region. The vor-

tical flow first evolves over an order of magnitude in Reynolds number, with the reattachment point x^* remaining on the cavity-leading wall (x_1) as the Reynolds number increases. Then the reattachment point exponentially migrate along the cavity sidewall (x_2), over a Reynolds number range. Lastly, flow separation in the cavity reaches an asymptotic phase where the reattachment point stagnates at the end of the cavity trailing wall (x_3) ($x^* \approx 1$). The evolution of the reattachment point as a function of Reynolds number can be described by a logistic function (Fig. 2.2c).

$$x^* = \frac{1}{1 + e^{-k(Re-a)}} \tag{2.2}$$

In which x^* is the location of the reattachment point along the normalized cavity side length ($x^*=\frac{x}{\sum X_s}$), k is the curve steepness, and a is the value of the sigmoid's midpoint. Both simulation and experimental results reflect the logistic function behavior (Fig. 2.2c).

To identify the controlling dimensionless parameters we measured the effect of cavity geometry on the reattachment point as a function of different cavity side lengths ($X_s = 100 - 1000\mu m$) and Reynolds numbers ($Re = 0.1 - 500$) (Fig. 2.5a). When scaling by $Re(H/Xs)$ vortex reattachment point growth curves from different cavity side lengths collapse into the previously discussed logistic relation (Fig. 2.5b). Channel width ($W = 40 and 100\mu m$) did not contribute to cavity growth in the new dimensionless scale (Fig. 2.6). Using this scaling and the logistic function, one can define a condition at Re = a when the vortical flow occupies half of the total cavity volume, i.e. $Re_{0.5} = Re_{(x*=0.5)}$.

$$0.5 = \frac{1}{1 + e^{-k(Re_{0.5}\frac{H}{X_s}-a)}} \tag{2.3}$$

$Re_{0.5}$ is substituted in terms of the logistic function to derive a universal formula that estimates half cavity flow of any cavity side length, height, and main

channel velocity.

$$Re_{0.5} = a(\frac{X_s}{H}) \tag{2.4}$$

2.3.2 Separatrix breakdown

Next, we look at how the recirculating wake unfolds in the cavity and flow exit to the channel in three-dimensional space. Fluorescently labeled laminar streamlines from incremented initial locations in the main flow are observed inside the cavity as a function of cavity flow development stages defined by the reattachment point (x^*) transition (Fig. 2.10). At $x^* = 0$, streamlines enter and exit with fore-aft symmetry as observed in the previous section (Fig. 2.11a). $x^* > 0$, at higher flow conditions, where recirculating flow starts developing and a separation bubble forms on the leading cavity wall x_1 (Fig. 2.11b). Due to the no-slip on the upper and lower stationary cavity walls, fluid flow far from the wall rotates more freely where both swirling flow from each side of the symmetry line connect in the middle.

The recirculating flow starts to form at the upper and lower walls of the cavity. The small side vortices get connected in the middle of the cavity at ($x^* \geq 0.1$) when flow separates from the mainstream channel to the side cavity. At x^*=0.5, streamlines from different initial inlet locations (Q1-Q3) unfolds differently inside the three-dimensional confined space of the cavity. Flow from inlet Q1 and Q2 interacts with the cavity walls. Flow from inlet Q3 does not interact with the recirculating wake region (Fig. 2.12). The vortex core is viewed at the symmetry line with 2D fluorescent images showing laminar mixing of cavity flow.

At $x^* \approx 0.9$, vortex core shift to the trailing wall (x_3) and two dominant vortical flow form in each side of the cavity. When the vortex core completely moves towards the trailing wall, separatrix breakdowns where flow exit from the

side of the cavity in a swirling motion to the channel mainstream flow (Fig. 2.13). Recent theoretical investigation suggests the same manner of continuous mass exchange between the channel and the cavity when reach full cavity flow [26]. In a previous vortex particle entrapment studies, we notice an empty vortex core after circulating flow reach full cavity flow [71]. This suggests the fluid exiting from the vortex core to the channel resulting in a shift from an attractive limit cycle state to particle repeller after separatrix breakdown [54]. At later stages of $x^* \approx 1$, flow starts to unfold differently and swirling vortex disappears. A higher form of flow complexity is formed at higher Reynolds number values, we observe a secondary and tertiary corner vortices that won't be covered in this study.

To validate our previous finding, we build a step in the outlet region of the cavity to see if streamlines from the vortex core shifts due to the no-slip flow condition of the step. Fluorescently stained streamlines from the vortex core divert from the step into the channel. This proves streamlines from the vortex core exiting the cavity flow due to direct mass transport to the channel flow (Fig. 2.14).

2.4 Summary

Flow in channels and ducts with adjoining cavities are relevant to a number of natural and engineered systems and has garnered renewed attention as an approach to selectively isolate particles. Cavity-channel mass exchange for three-dimensional 3D confined channels is relatively unexplored compared to 2D systems in which a separatrix forms that limits mass transport between an open cavity and the main channel. Here we report on 3D confined cavity flow formation and development. Separatrix breakdown, where streamlines from the main channel flow join the recirculating cavity flow is observed for conditions when the recirculating wake saturates the cavity. These findings extend our understanding of flow entry

and exit in cavities with finite confinement and suggest conditions where convective mass transport into and out of cavities would be amplified and microvortex particle capture are reduced.

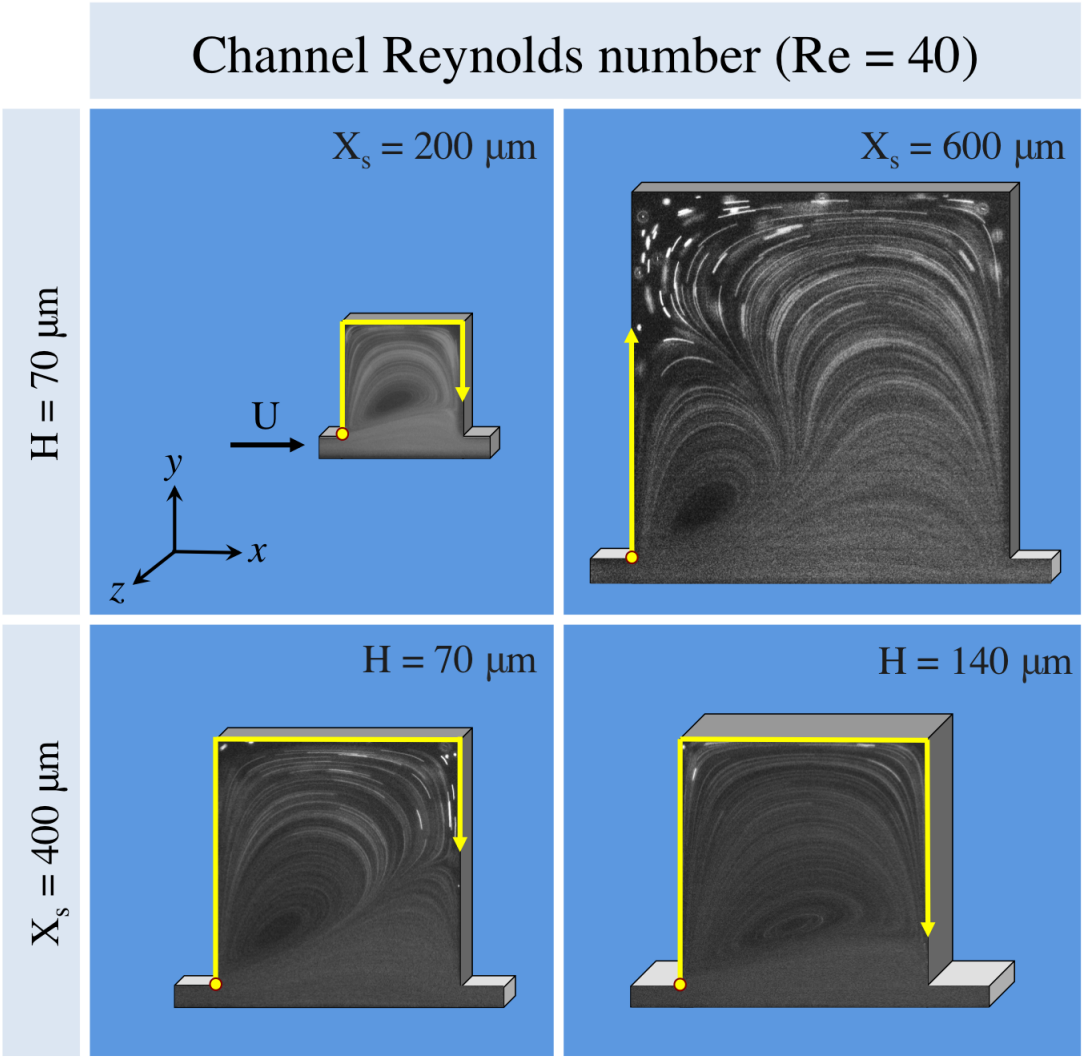

Figure 2.1: Cavity geometry dictates the vortical flow growth state at the same channel Reynolds number. Fluorescent microscope images of cavity flow shows the significant contribution of the cavity aspect ratio (H/X_s) to the flow growth in three dimensional confined cavities, where H = cavity height = channel height (μm), X_s = cavity side length (μm). The channel Reynolds number ($Re = \frac{UD_h}{\nu}$) were held constant across different cavity geometry, where the channel hydraulic diameter $D_h = \frac{2(WH)}{(W+H)}$ (m), U = fluid velocity (m/s), W = channel width (μm) and ν = kinematic viscosity (m^2/s).

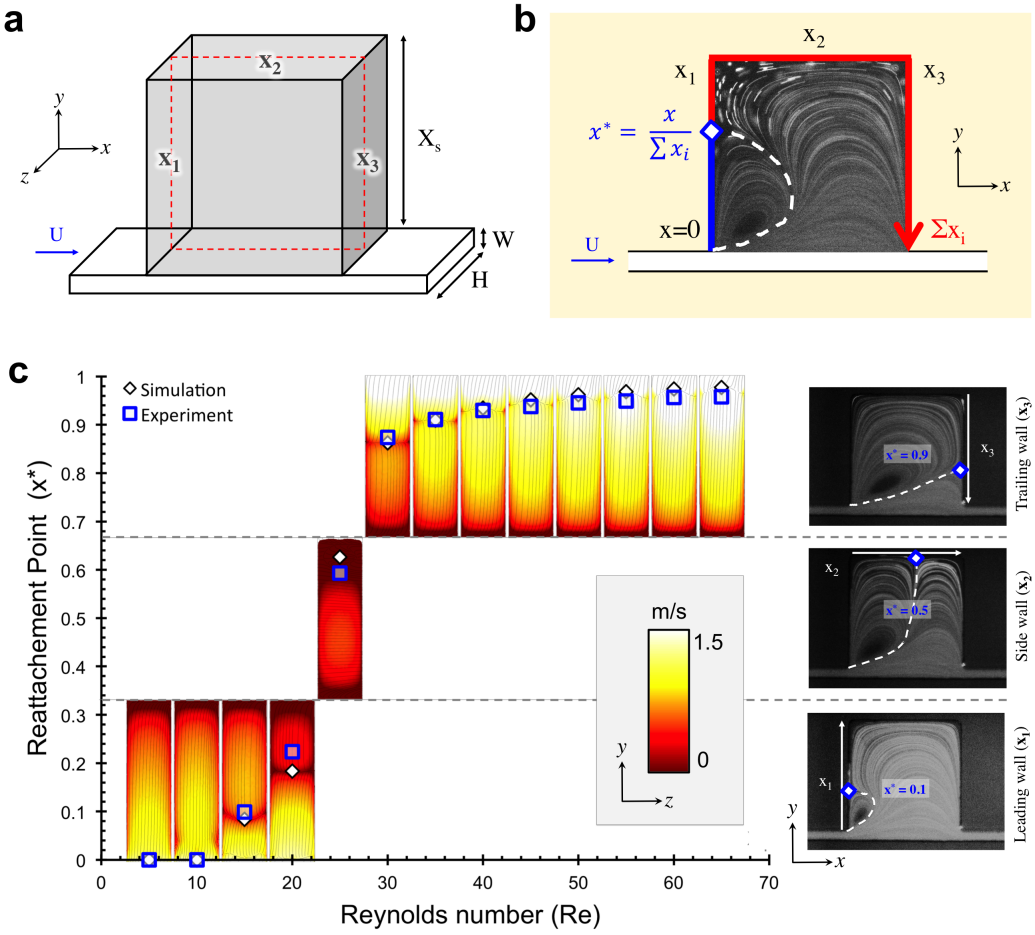

Figure 2.2: Logistic growth of three-dimensional confined cavity flow. (A) Three dimensional cavity diagram with leading wall (x_1), side wall (x_2) and lagging wall (x_3). (B) Top down view of the experimental set up for confined cavity flow characterization by the transition of reattachment point (x^*) on all stationary cavity walls ($\sum x_i$). (C) Experimental ($\square$) and numerical simulation ($\diamond$) evidence of the logistic progression of the reattachment point (x^*) on the cavity walls with cavity side length ($X_s = 250\ \mu m$) and cavity height (H = 70 μm) as a function of the channel's Reynolds number with $70 \times 40\ \mu m$ ($H \times W$) channel height and width. Color bar indicate the velocity profile (m/s) around the reattachment point on the cavity wall (white: fast, dark red: slow).

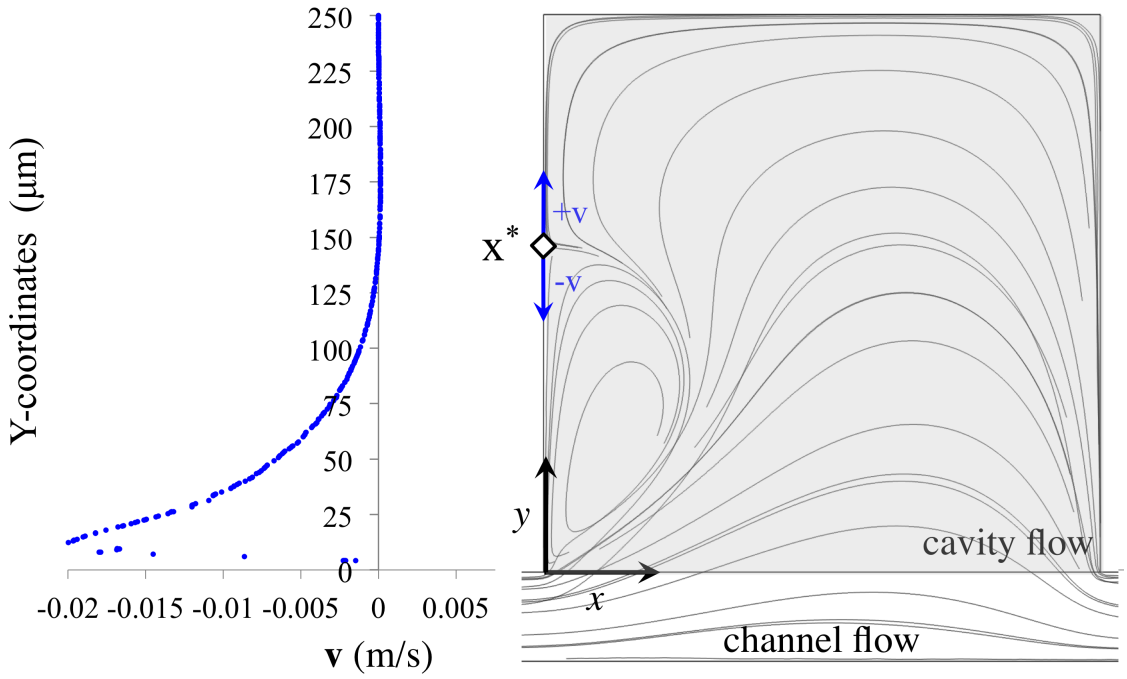

Figure 2.3: Reattachment point (x^*) calculation in numerical simulation results. The reattachment point is located when the y-component velocity (v) along the midpoint symmetry line on the cavity wall equals zero. On leading wall (x_1) flow going to the channel ($+v$) and flow going back to the cavity ($-v$). Similar to (x_3) with opposite velocity component signs. In the side wall (x_2), x-component velocity (u) is measured along the wall to determine the reattachment point.

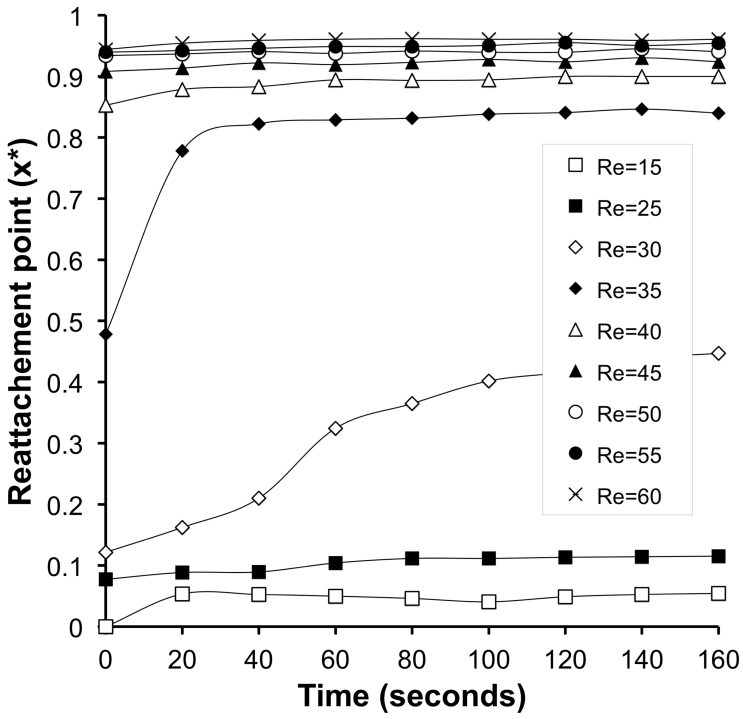

Figure 2.4: Spatiotemporal plot of the reattachment point (x^*) progression. Experimental measurement of the reattachment point progression of different Reynolds's numbers as a function of time t(sec). Reattachment point stabilizes after one minute of changing the flow rate. A pronounced transition of cavity wall on the side wall (x_2) parallel to the direction of channel flow.

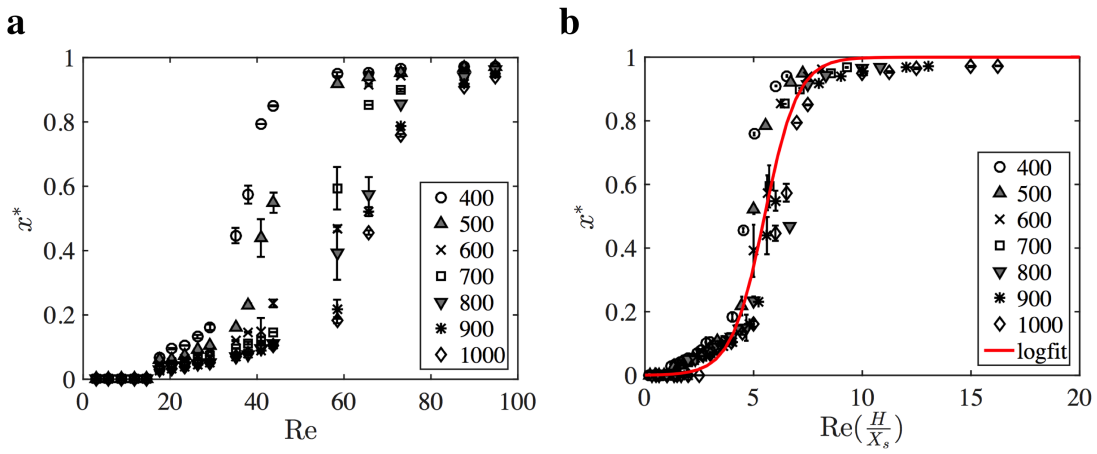

Figure 2.5: Universal scaling of cavity flow development through following the reattachment point evolution on the cavity wall. The figure shows the phases of cavity flow growth in the channel's Reynolds number (Re) versus the scaled channel's Reynolds number by the cavity aspect ratio (Re (H/X_s)). (A) Experimental result of the reattachment point (x^*) transition in different cavity side lengths ($X_s = 400 : 100 : 1000\ \mu m$) as a function of the channel's Reynolds number. (B) Empirical data of vortex growth data for different cavity sizes collapse when plotted as a function of the cavity geometry ratio and Reynolds number. The data set were fit in a logistic function presented in a solid red line (-) with parameters used in Eq. (2.1).

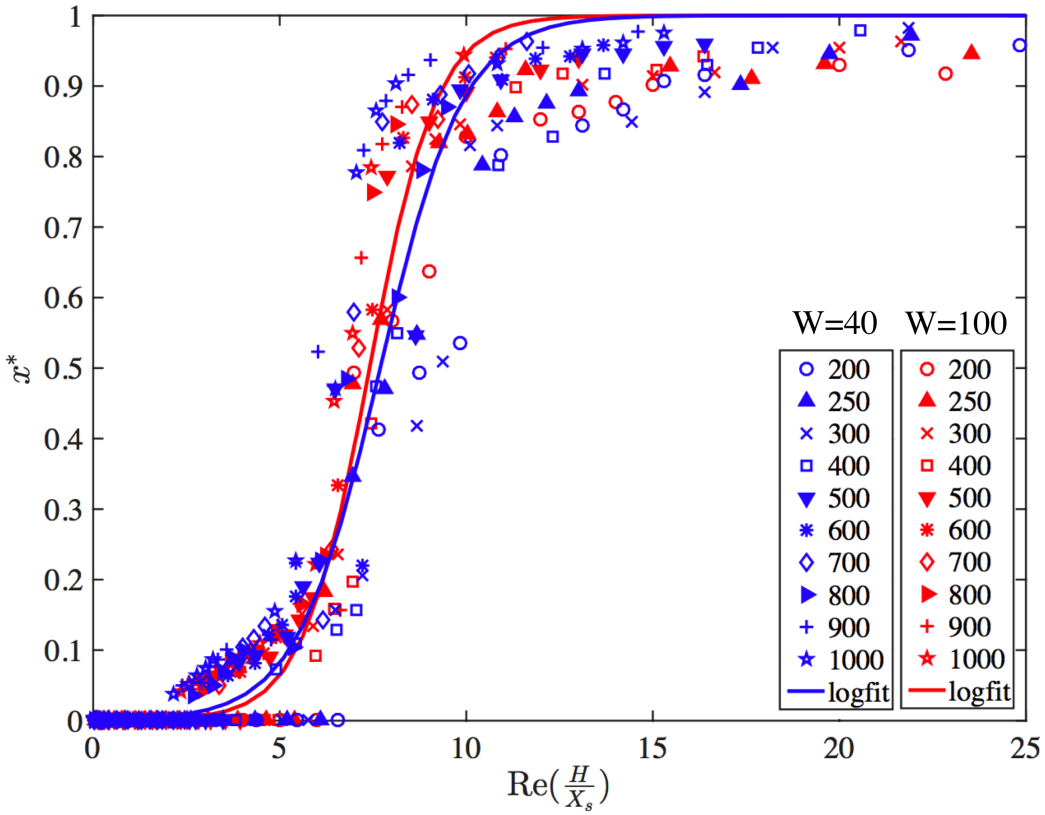

Figure 2.6: The channel width does not significantly contribute to the cavity circulating flow development with the scaled Reynolds number. The reattachment point (x^*) progression plotted against the scaled Reynolds number show no significant shift or difference with two channel widths W = 40 μm (blue) and 100 μm (red).

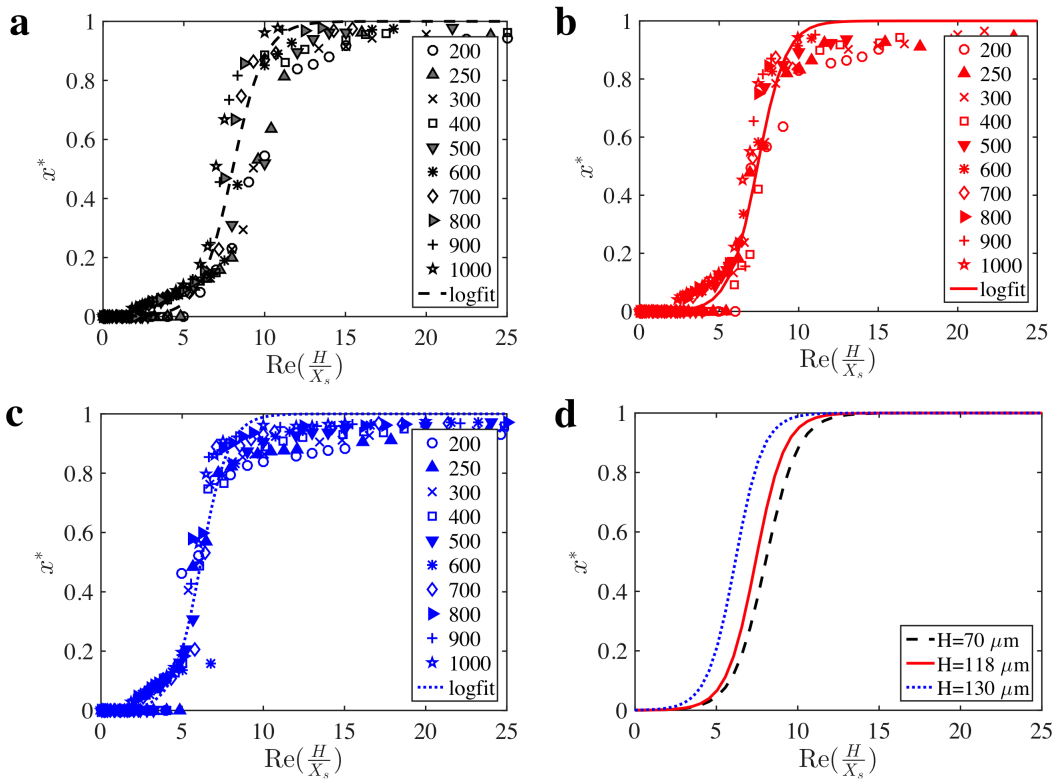

Figure 2.7: Universal scaling of microcavity flow logistic growth and correlation with cavity height. Colored symbols denote results of different cavity heights, (A) H= 70 μm (black), (B) H= 118 μm (red) and (C) H=130 μm (blue). (D) collection of all log-fit of different heights.

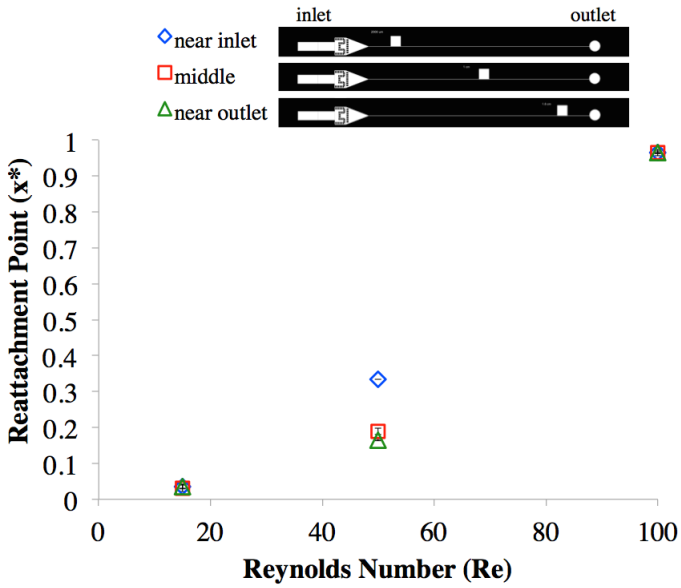

Figure 2.8: Reattachment point (x^*) measurement across different cavity locations along the channel validate the use of PDMS device for cavity flow study. Reattachment points (x^*) are plotted at different downstream cavity location ($\diamond$) near the inlet (high pressure region), ($\square$) middle of the channel and ($\triangle$) near outlet (low pressure region). Cavity flow develop similarly in different pressure points in PDMS device. Flow in the side wall x_2 is less uniform than other measurements.

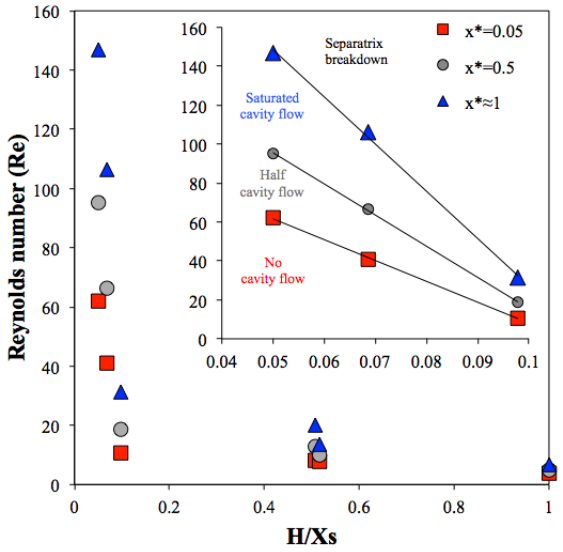

Figure 2.9: Phase diagram showing three different flow transition of cavity flow (no cavity flow, half cavity flow and full cavity flow) as a function of the cavity aspect ratio (H/Xs).

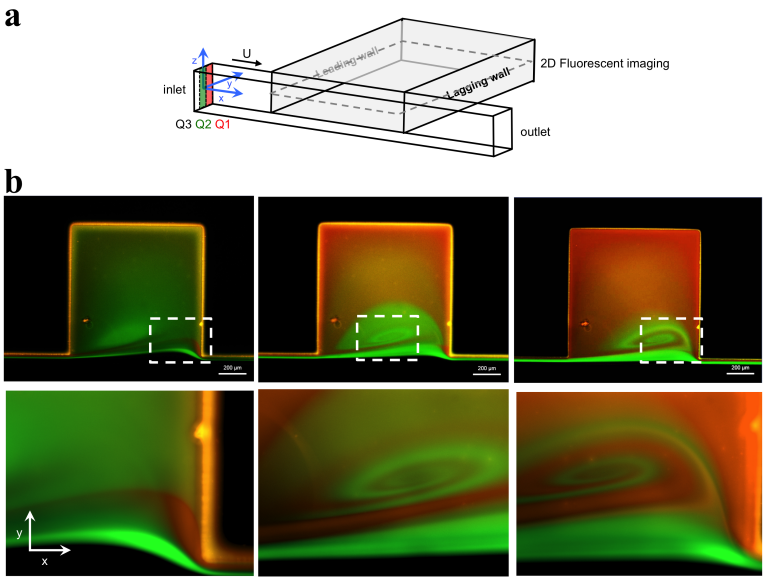

Figure 2.10: (a) Schematic illustration of 2-D cavity flow imaging and experimental setup. The device with three inlet (Q1-Q3) flow, where two different fluorescent dyes Q1 (red rhodamine), Q2 (green fluorescein) label the streamlines near the channel-cavity flow, and Q3 colorless water on the other side of the channel. (b) Progression and formation of the circulating streamlines at different reattachment points reaching to full cavity flow.

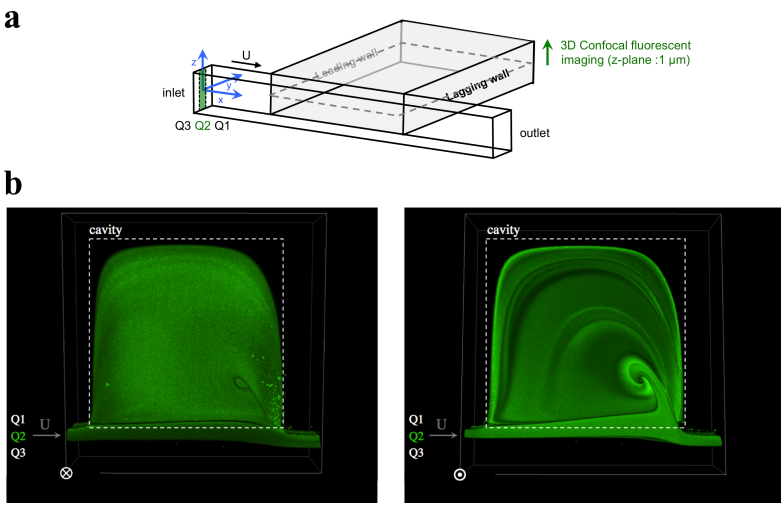

Figure 2.11: (a) Schematic illustration of 3-D cavity flow confocal imaging and experimental setup by capturing 2D images with 1 μm increment for high spatial resolution. Fluorescent dye is applied in the midline of the inlets (Q2) to visualize how the flow unfold and exit from the cavity flow. (b) Separatrix breakdown of the vortex core near the trailing wall in confined cavity flow. Images are taken from the middle to the upper side of the cavity show flow symmetry with two dominant vortical flow exiting near the cavity upper and lower walls to the main channel flow.

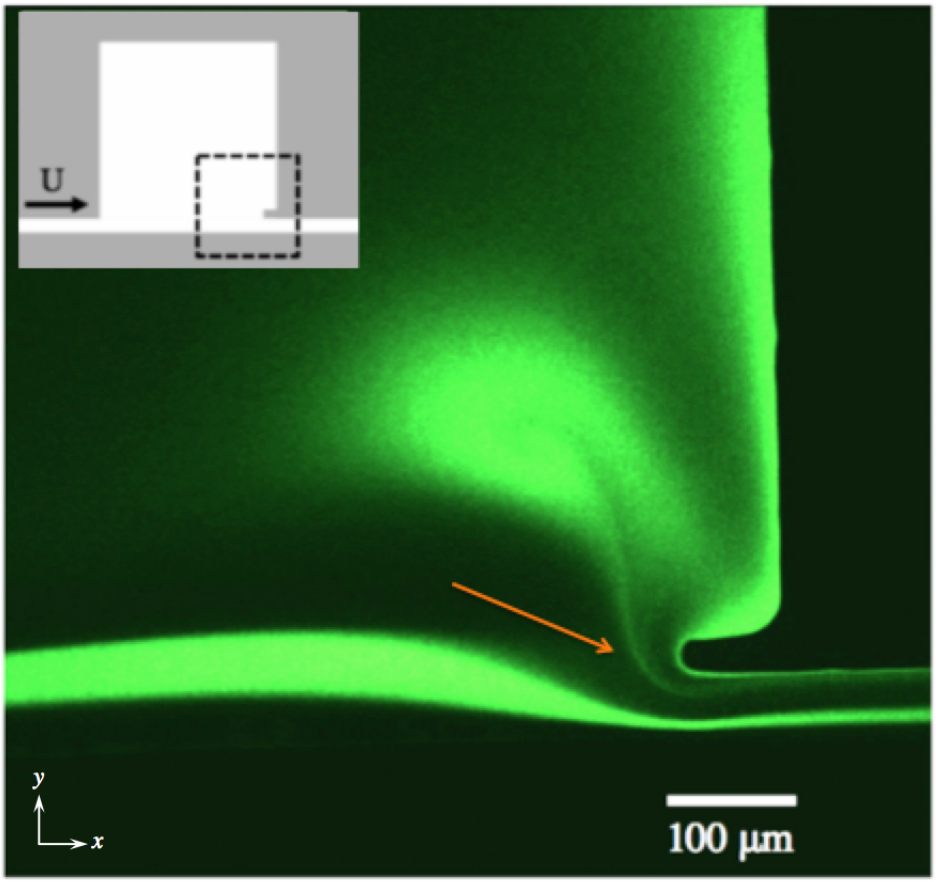

Figure 2.12: 2D fluorescent image of separatrix breakdown in cavity flow with swirling streamlines exiting from the cavity to the channel.

CHAPTER 3

Motor-driven Microfluidics

3.1 Introduction

Artificial intelligence has lead to the automation of data analysis for biomedical researchers [42]. Large-scale learning of complex inter- and intra-cellular differences has minimized human bias in defining subcellular classifications [117]. However, continuous cross-talk between AI software and wet lab hardware is necessary to achieve full AI convergence for data-driven cell sorting with minimal human handling and intervention. Thus, there is a growing interest in interfacing current wet lab hardware infrastructure including manual labor-intensive pipetting or automated closed microfluidic instrumentation with AI software [56]. Conventional manual liquid handling tools allow scientists to collect data with dynamic bandwidth (volume of information/unit time) from variable cells [15]. However, the low-throughput (number of cells/unit time) of manual data collection is limiting for data-intensive training. Processing a large number of cells through automated microfluidic instrumentation enable interfacing high-throughput data analysis with AI software tools. The key challenge in current automated systems is the fixed bandwidth since the instruments are not designed to expand more functionalities to collect more information from sorted cells (e.g. 3D spatial infromation, 4D time-dependent functions). Automated microfluidic cell sorting devices are not accessible for biologists to modify assay protocols to serve multi-purpose testing. A programmable microflow infrastructure with dynamic bandwidth and high throughput are required for AI integration to learn complex cellular heterogeneity.

Therefore, there is a need for a flexible open-platform microfluidic hardware to bridge the technology gap between accessible manual liquid handling and closed high-throughput microfluidic systems for processing and analyzing cells.

The trade-off between bandwidth (i.e. volume and complexity of data) and throughput (i.e. speed) is the main technical barrier for intelligent computer-assisted image-based cell sorting systems. Previous studies demonstrated microfluidic systems integrated with image analysis software to perform high throughput intelligent single-cell sorting and analysis [93]. However, the fixed back-end hardware of closed microchannel flow lacks modularity to handle heterogeneous cellular and multicellular size and shape variability. Preprocessing steps are required for filtering out cell clusters or large cellular structures to prevent microchannel blockage. Large multicellular structures like spheroids and organoids are important in drug discovery and cell therapy but they are not compatible with current continuous flow microfluidics platforms [45, 76]. Scaling the flow inertial forces for large cellular structures ($Re_{particle}$) require high shear flow that damage complex 3D structures and also cause turbulent flow that disturbs in-situ microflow control [32]. Lastly, loss of three-dimensional information is a recurrent problem of suspended large structures (e.g. distribution of cells in organoids) and require an advanced optical setup for 3D scanning [70]. Manual pipetting and confocal microscopy are the current available technologies to attain rich 3D information, but they are not scalable for fast AI-enabled automated organoids sorting [12].

In this research, we present an alternative microflow control approach by developing motor-driven microfluidics with compatible functionalities to automation and artificial intelligence. (Fig. 3.1) We demonstrate real-time data-driven cell sorting scalable to a wide size range (e.g. single-cell microcarriers [127] or droplets [77], cell clusters, spheroids, and organoids). 3D inspection is performed on large cellular structures without changing the device or optical system. As a proof of

principle, non-binary image-based sorting is performed on cells in droplets based on the cell count with the potential to expand on multiple phenotypic properties (e.g. cell size, shape, and fluorescent intensity). Programmable motor-driven microfluidics is accessible to biomedical researchers. It expands the basic functionalities of the current microfluidic systems without microchannel fabrication in a clean room facility or high-end pressure-driven pumps for precise microflow control.

3.2 Results and Discussion

3.2.1 Motor-driven flow

The basic flow-driving unit is composed of two co-axial motors immersed in fluid (Fig. 3.2a). Assuming circular motor shafts with equal radius ($a = a_1 = a_2$) rotating in opposite sense (clockwise = $-\Omega_1$, anticlockwise = Ω_2) at the same angular velocity ($|\Omega| = |\Omega_1| = |\Omega_2|$), the flow has Reynolds number ($Re = ua/\nu$), where u is the motor velocity ($u = \Omega a$) and ν kinematic viscosity. We annotate the space between the rotor centroids by L, and the space between the two motors shaft walls by ($l = L - a$). We represent the distance ratio (h=a/L) between two motors of any size to determine the flow type and direction between and around motors. The characteristic length ($h = 1$), when the motor walls are in contact ($l = 0$). $h > 0.5$ when the two motors are placed close together ($l < a$) and $h < 0.5$ when the motors are placed far apart ($l > a$). We analyzed the flow field between and around rotating motors placed at different proximities (h=0.1-0.9) and at a range of Reynolds number (Re=0.05-100). We aim to produce Jeffery's flow where fluid at a certain distance upstream the motors are allowed to pass in between the motors (Fig. 3.2b) [66, 119]. Closed streamlines are formed around the two motors and far fluid flow is quiescent at infinity. In the next section, we select Jeffery's flow at viscous flow conditions Re < 5 and proper motor distance

$h < 0.25$, for the purpose of precise microflow control in between an ensemble of rotating micromotors.

3.2.2 Modular microflow control

In this section, we aim to reproduce basic flow control functions of confined microfluidics systems (e.g. driving and shaping flow) in an unconfined motor-driven flow. The sample is introduced upstream in the midline (x-axis) between suspended DC motors in an open petri dish with a viscous carrier fluid. In this case, the convection of the viscous carrier fluid will dominate over the sample fluid diffusion, allowing precise control of sample fluid or suspension along the directed paths between the motors. Since the device is operating in a linear stokes viscous regime, inertial terms can be neglected [9]. The flow, in this case, has no memory and therefore suspended particles reach equilibrium positions in flow at all times [52]. This property is essential to reach a steady motion at selected initial conditions. Additional flow-driving units are added and aligned laterally downstream the midline to push sample flow further at a desired length (Fig. 3.3a). Motor wall rotation will actuate the rotation of the surrounding carrier fluid. At the carrier-sample fluid interface, the rotating flow will move the sample fluid through the midline between the motors then pass the flow downstream to the next flow driving unit. An ensemble of flow-driving units can push the sample fluid continuously to a certain downstream distance or shape at a macro and micro scale (Fig. 3.b-c). To vary the sample flow rate, simulated and experimental results show the effect of different motor velocities on the fluid flow between the motors (Fig. 3.4). The bulk fluid velocity can be adjusted to different flow rates reaching up to 1 m/s comparable to the flow speed in microchannel pressure-driven flow. Motors with different size, shape, and angular velocities allow a dynamic mass transfer of the sample fluid to stop, reverse, slow or speed up the flow at different spatial points for modular microflow control. Therefore motor-driven flow can produce

precise and predictable in-situ spatiotemporal microflow control without the use of external pressure-driven pumps or fabricated microchannels.

3.2.3 Automated modular sorting

The linear relation between motor rotation and fluid motion enables proportional control of fluid or suspended particles movement by a computer-assisted linear feedback control system [112]. Flow stops and moves instantaneously with the motor actuation. We interfaced two motor driving units with an in-house image analysis code for real-time data-driven sorting of cells, droplets, and organoids. Different size structures are sorted in the same device with the same response time. 3D scanning was performed by actuating motor rotation with the same orientation (e.g. clockwise or anti-clockwise) creating rotational flow. Organoid's 3D spatial information is collected while rotating in the motor-generated rotational flow with a basic microscope set up to bypass the use of complex optical equipment (Fig. 3.5). A joystick is connected to the motor system for user input to override the computer command in case more investigation is needed by the researcher. Non-binary image-based sorting of droplets cell count (0 cells (down), 1 cell (right), 2 cells(left)) were achieved with 86% accuracy (Fig. 3.6). Additional complex phenotypic properties of cells (e.g. morphology or fluorescence intensity) can be sorted by motor actuation of diagonal and orthogonal flow directions to increase the capacity of cell sorting options up to 8 different outlets.

3.3 Materials and methods

3.3.1 Simulation

COMSOL simulation was conducted to find the optimal distance (L = 0.1-50 mm) between two rotating cylinders with radius (R = 400 μm - 3 mm) and linear

velocity of rotor cylinder wall is ($u_{\theta(r=R)}$ = 0.1-3 m/s) in a carrier fluid with viscosity (η). We assumed incompressible fluid in steady state laminar flow in the computational model based on Navier-Stokes equation:

$$\rho(\frac{\partial u}{\partial t} + u \cdot \nabla u) = -\nabla p + \eta \nabla^2 u \tag{3.1}$$

with u, p, ρ and η representing the velocity, pressure, density and dynamic viscosity of the fluid respectively. No-slip boundary conditions are applied on the motor walls and the fluid container. The carrier fluid is assumed to be water and glycerol at room temperature, T= 300 K. The reference point of the system (x_0, y_0) is centered in the midline ($\alpha = 0$) between the motors to evaluate the forward and back flow upstream and down stream the motors. Velocity components (u and v) in this set up show a negative value in back flow and positive value in forward flow driven by motors. The heat color map shows blue color for forward and red color for backward flow. A cutline before, after and between the motors are set to analyze the flow field at different motor and fluid conditions.

3.3.2 Imaging

Flow between the motors was viewed using a microscope (Nikon Ti-U) connected to high-speed Phantom V2010 camera (Vision Research Inc., Wayne, NJ, USA). Images were recorded at 1000 frames per second for characterizing bulk flow velocity between motors. In-house image processing code was developed with MATLAB to track particle motion. The fluorescence images are captured by CCD Coolsnap HQ2 camera (Roper Scientific, Evry, France). Particle tracers are imaged at 2 frames per second for analyzing long-term behavior of bulk flow between motors.

3.3.3 Micro-motor operation

A coreless micro-motors powered by DC voltage is used to build viscous micro-pumps set-up. Electromagnetic field generated by the power supply actuates shaft rotation. Rotor angular velocity is controlled by the voltage input. We tested different input voltage and observe rotation of the motor with high-speed camera to calculate angular velocity (Rotation Per Minute RPM). Motors are fixed on top of the fluid container at different distances. In-house image analysis code is connected to the motor control unit to actuate the motor rotation via continuous feedback control.

3.3.4 Carrier fluid, particle suspension and droplets

Carrier viscous fluid in the micro-pump set-up is fluorescently labeled with rhodamine and fluorescein to track flow between motors. Fluorescent polystyrene particles with mean diameter 30 μm are purchased from (Phosphorex, Hopkinton, MA) is used to trace the bulk flow around the motors. MCF-7 (30 2004, ATCC, Manassas, VA) was cultured in DMEM medium (ATCC 30-2002). The medium was supplemented with 10% fetal bovine serum (Invitrogen, Carlsbad, CA) and 1% penicillin streptomycin (Invitrogen, Carlsbad, CA) at 37 °C under 5% CO_2 conditions. Cells were passaged once they reached an 80% confluence. The cells and medium tested negative for mycoplasma. Droplets are made by step emulsification and produced to the system by pipetting upstream the motors. Droplets and cell encapsulation method is described in detail in [77].

3.4 Summary

In the past two decades, researchers envisioned a viscous micro-pump set-up [29] to achieve autonomous and modular microflow control. Localized flow generated

by wall slip velocity of the micromotors in confined channels has been heavily studied in many theoretical models [126]. This has inspired many research studies to develop methods of fabricating and actuating micromotor rotation by different technologies [81, 3, 4, 123, 96, 65, 35, 19, 37, 69, 122]. However, micro-motor flow in confined microchannels did not translate to practical applications due to the flow dampening effect of the confined channel walls. We have developed an open channel motor-driven system to translate and automate practical biomedical applications in cell sorting and 3D inspection. Continuous crosstalk between machine learning image analysis software and computer-assisted control of motor-driven flow enable the automation of biomedical research in understanding cell heterogeneity without the need of soft-fabrication or the use of external pumps.

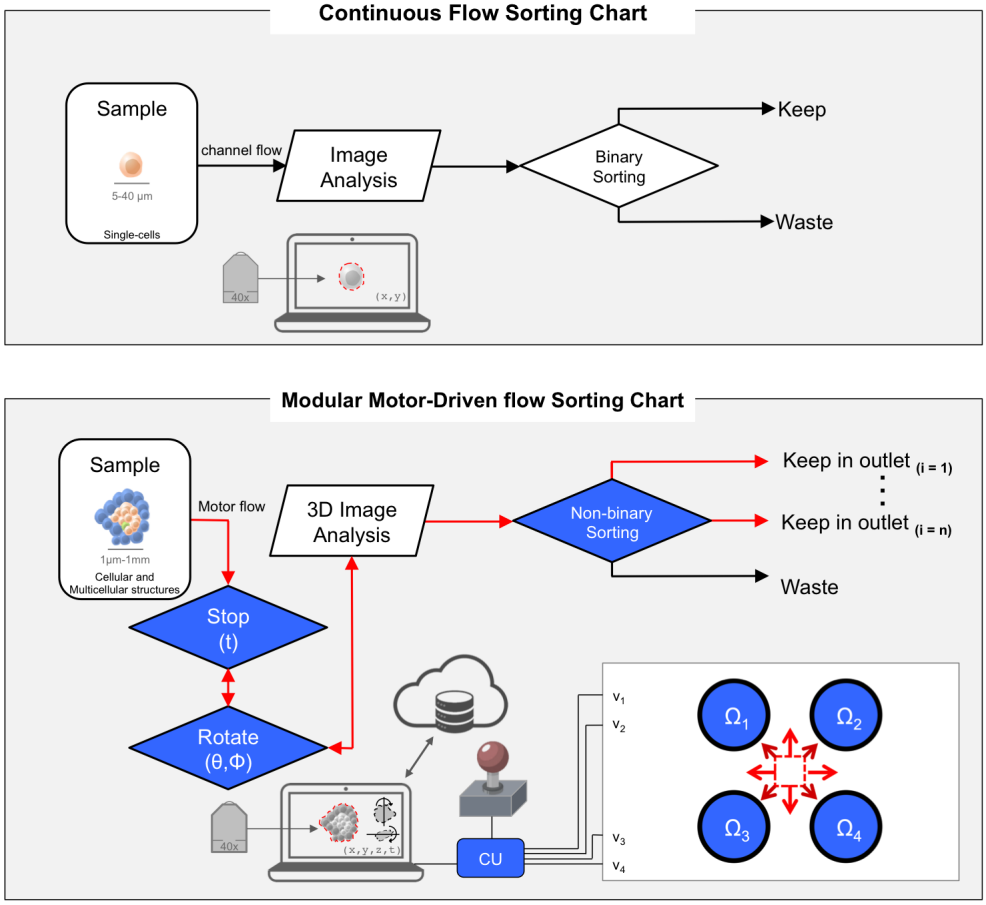

Figure 3.1: Schematic of automated motor-driven microfluidics work-flow for modular sorting systems. The top box illustrates continuous flow microfluidics work-flow for image-based binary sorting systems limited to single-cells. The bottom box illustrates modular unconfined motor-driven flow functionalities for automated non-binary sorting systems with intelligent 3D inspection of a wide size range of cellular and multicellular structures.

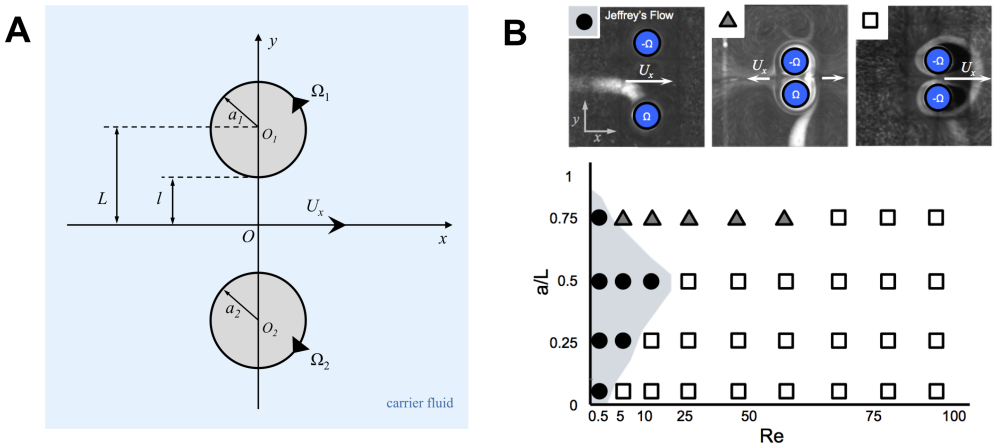

Figure 3.2: (a) Two side-by-side rotating motors suspended in fluid with opposite angular velocities ($\pm\Omega$) and identical circular shaft radius (a) with distance between the motor centroids ($|O1O2|/2 = L$). (b) Phase diagram showing motor-driven flow type development as a function of the Reynolds numbers and the distance between the two motors.

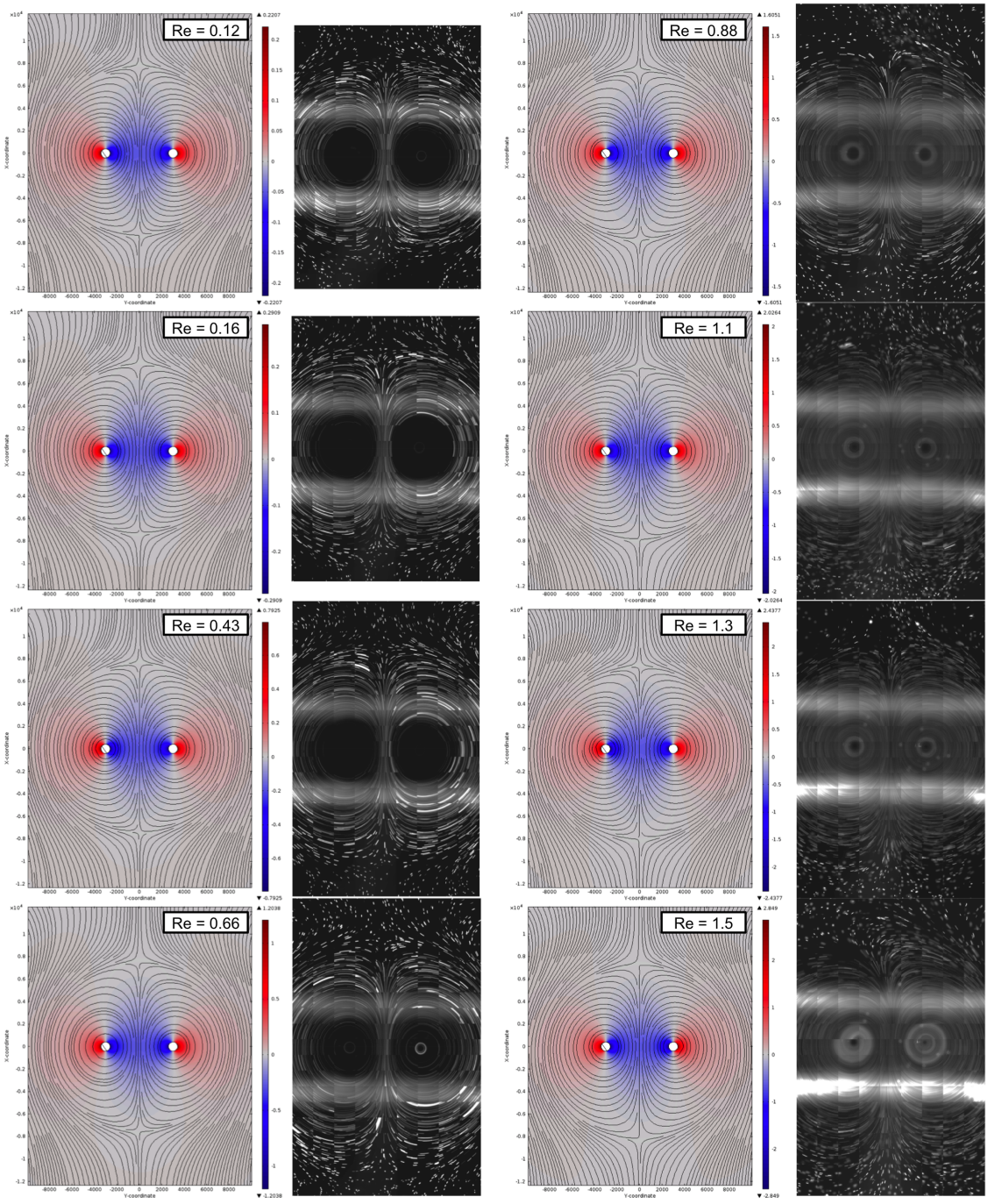

Figure 3.3: Spatio-temporal microflow control of one motor-driven flow unit at h=0.1 and a range of Re (0.12-1.5) show the ability to change the sample flow rate. Simulation and particle tracing experiments illustrate uniform Jeffery's flow at different motor angular velocity.

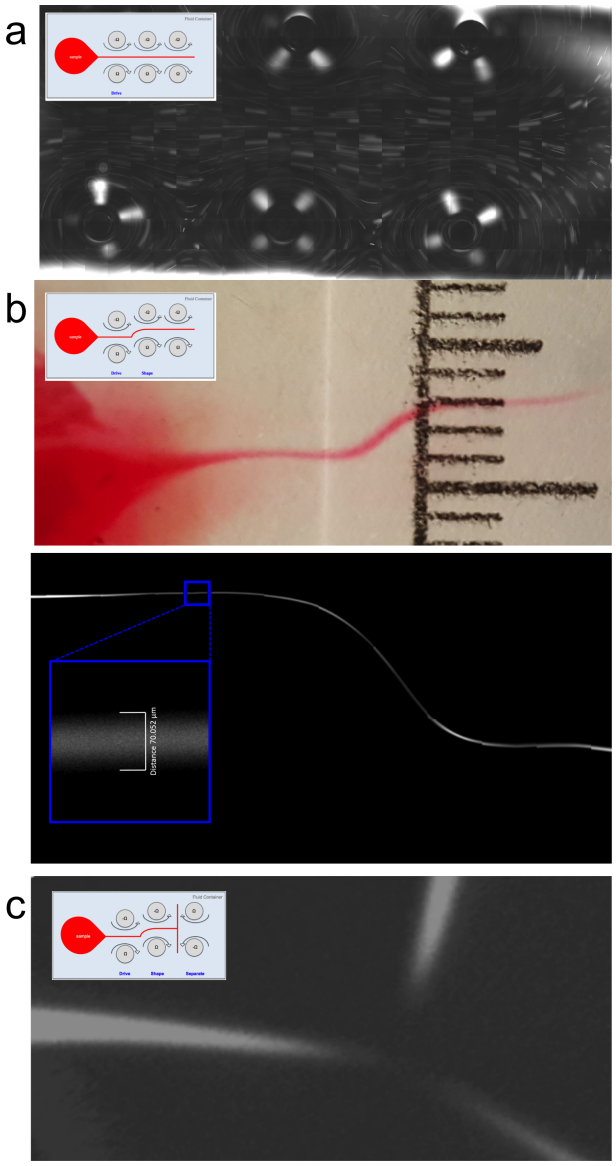

Figure 3.4: Modular microflow control via motor-driven microfluidics. An ensemble of micromotors can substitute the basic functions of confined microchannel pressure-driven flow like driving (a) shaping (b) and separating (c) the flow of a sample fluid.

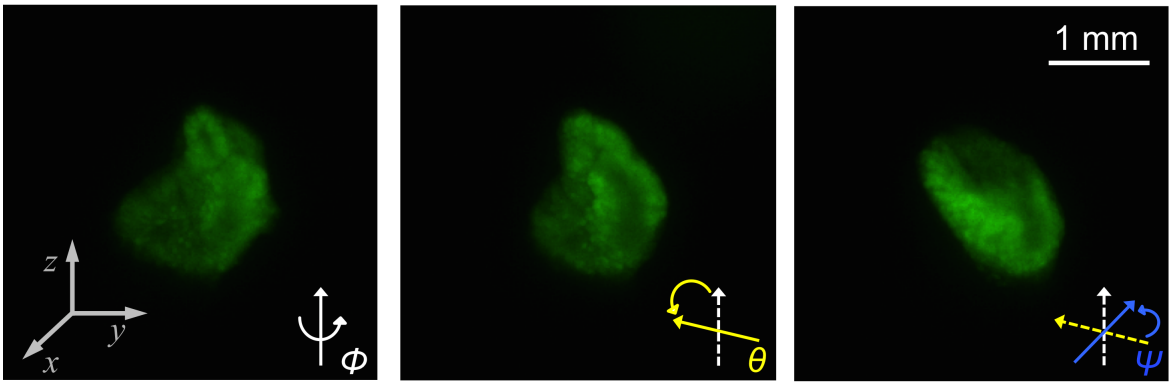

Figure 3.5: 3D inspection before sorting. Computer-assisted modular rotational flow allow 3D scanning of large cellular and multicellular structures spatial information (cells are stained with calcein green) with conventional fluorescent microscopy.

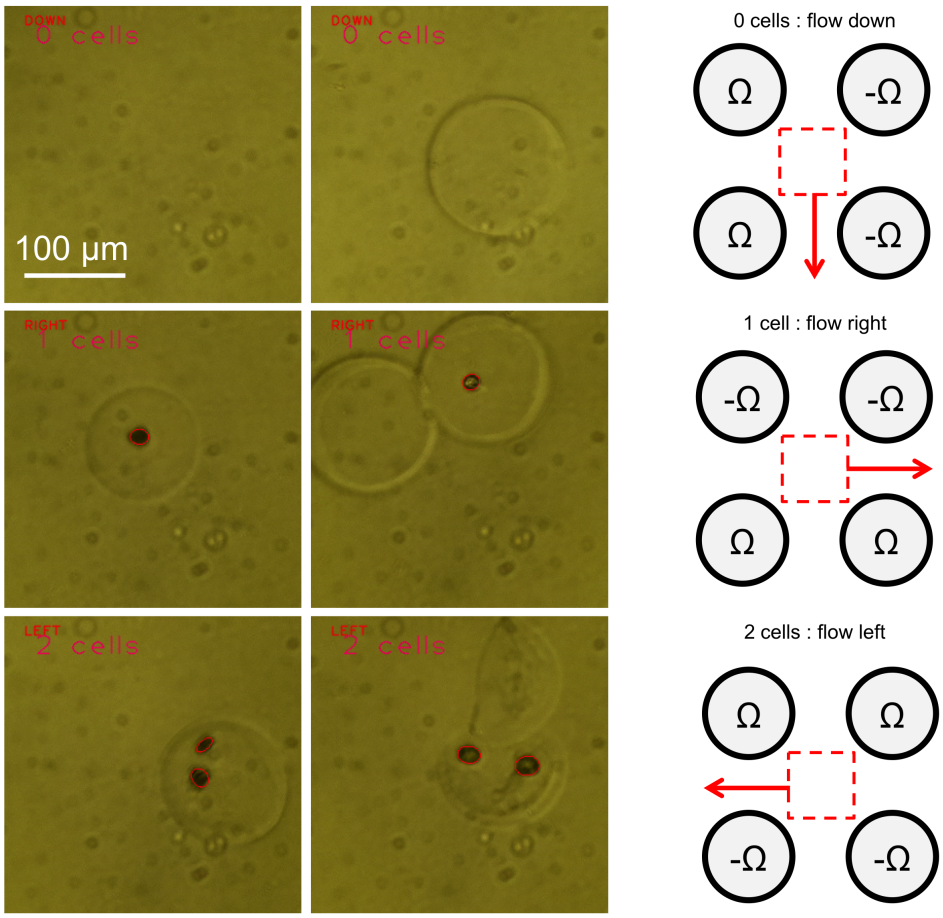

Figure 3.6: Automated modular motor-driven microfluidics sorting of droplets. The top panel shows the default state of motors flowing the sample and carrier fluid down when cells are not detected. When cells are detected in droplets, cells are then sorted based on their number to two different outlets.

CHAPTER 4

Cytocompatible Magnetostrictive Microstructures for Nano- and Microparticle Manipulation on Linear Strain Response Piezoelectrics

4.1 Introduction

The continuously increasing interest in nanoscale magnetic devices has encouraged researchers to develop new methods of controlling magnetism at the nanoscale. One such method involves artificial multiferroic heterostructures, where strain induced in piezoelectric materials is transferred to a magnetoelastic material layer to enable control of magnetism via an electric field. Compared to conventional electric current-control of magnetism, electric-field-driven control of magnetism in multiferroic heterostructures has several advantages. For example, the multiferroic approach allows for reduction of power dissipation in small scale applications, and the accompanying potential for highly arrayed and localized device actuation. This multimodal control holds promise in the development of new energy-efficient applications, including nonvolatile memory devices [11, 2], actuators and transducers [27], and miniature antennae [135]. Furthermore, the potential of electric-field-controlled magnetism in biomedical applications has been explored in the manipulation of magnetic particles [109]. Recently, manipulating magnetic particles with local magnetic fields has emerged as an appealing method for transporting bio-particles labeled with these magnetic beads [87, 90]. While extended exposure to dielectrophoretic traps [105] or optical tweezers [92] could damage

cells, transport and trapping via magnetic particle manipulation is a nondestructive alternative. In addition, magnetic particle affinity to particular proteins, introduced through antibodies or other recognition elements conjugated to the particle surface, provides cell-type specificity to manipulations.

While using localized magnetic forces for manipulating magnetic microbead motion (e.g. magnetic tweezers [28]) allows remote control, the prevalent approaches for controlling the movement of magnetic beads along with bound bioparticles are not capable of operating with a large array of individually addressable elements. Previous approaches involve either external rotating magnetic fields or microfabricated electromagnets, with the former being bulky and de-localized [109] and the latter posing problems such as on-chip heating [78]. On the other hand, using an electric field to control magnetic domain motion arises as a viable solution which not only benefits from magnetic force control with high precision, but also avoids problems such as joule heating and the need for bulky external magnets.

Moreover, it is of paramount importance to separate and manipulate cells and other bio-particles individually and in parallel for rapid biological analyses [106, 71]. By employing magnetic domain walls whose motion is tunable via electric-field using multiferroic heterostructures and combining the device with microfluidics, 'lab-on-chip' devices can be developed that are capable of controlling the movement of detected entities with high precision, for downstream sorting, sequential reaction, and analysis. Controlling the coupling of the beads to the domain wall movement along with parallel optical imaging and analysis technologies [50] opens up opportunities to a myriad of applications for rapid cell analysis in sorting based on complex phenotypes [15]. Large arrays of individually addressable cells are particularly important for sorting rare cells in a population that may be useful diagnostically (e.g. antigen-specific T-cells, circulating tumor cells, etc) or for selecting rare clones with useful properties for cell therapies or cell-based

bio-manufacturing.

[Pb(Mg1/3Nb2/3)O3] 1 -x - [PbTiO3] x (PMN-PT) is one of the most commonly used ferroelectrics in such multiferroic heterostructures. PMN-PT with composition close to the phase boundary (x $\approx$ 0.32 - 0.34) will undergo a morphotropic phase transformation [97, 46] with giant electromechanical response. Sohn et al [109] have previously demonstrated strain-mediated deterministic domain wall motion in Ni rings on single crystal (011) [Pb(Mg1/3Nb2/3)O3] 1 - x - [PbTiO3] x (PMN-PT, x $\approx$ 0.34) with morphotropic phase transformation, which induces a large hysteretic strain jump at an electric field of 0.5 MV m^{-1}. Such strain change induces domain motion in the ring structures, which subsequently results in abrupt particle motion. Magnetoelectric Ni/(011) PMN-PT heterostructures with different compositions have been extensively researched [80, 128, 133, 17, 59] with magnetization reorientation controllable by electric-field, providing the groundwork for further optimization and applications. While Ni (λ s(Ni) = -33 x 10-6) has been a popular choice for the ferromagnetic component in these systems, FeGa with an order of magnitude higher magnetostriction (λ s(FeGa) = 350 x 10-6) is attracting more attention due to the potential enhanced magnetoelectric coupling figure of merit applicable to a broad range of uses, such as being a promising candidate for memory devices [2].

In this work, we describe the fabrication process for magnetostrictive Ni and FeGa microstructures on piezoelectric PMN-PT. We chose Ni because it has been widely investigated in multiferroic systems in spite of the fact that it possesses only a moderate magnetostriction coefficient. We also include results on FeGa because its higher magnetostriction coefficient enables greater control of its magnetic state. We then demonstrate tuning of the magnetic state of nanoscale structures using electric fields, as shown by x-ray microscopy. The device behavior was also examined with nanoscale superparamagnetic beads, and the electric-field-driven steady speed bead motion with response to the linear strain variation was captured

by a high-speed camera.

Compared to the work of Sohn et al [109] using PMN-PT with morphotropic strain transformation, this work features PMN-PT with a linear strain. The benefit of actuating the particle movement using PMN-PT with linear strain is that it allows us to operate in a regime where the particle displacement is proportional to the applied electric field. The domain motion is activated at a comparable smaller strain with the applied field in the range of 0.16− -0.32 MV m^{-1}. While recent work has demonstrated the inhomogeneous nature of strain distribution in the single crystal PMN-PT [18], this response of the bead's continuous rotational behavior along the perimeter of the ring corresponds well to the linear macrostrain profile of the [Pb(Mg1/3Nb2/3)O3]0.69 - [PbTiO3]0.31. Localized capture of single particles with nm to μm diameters at the onion state domain wall of Ni and FeGa rings, and at the corners of squares with partial closure domain are observed by optical and fluorescence microscopy [74]. The advantage of using these microstructures with localized domains is to enable single particle capture at specific locations rather than agglomerates of beads. In addition, a successful attempt to settle cells to the surface of the device were demonstrated, and cell viability under applied electric field from 0 to 0.8 MV m^{-1} was confirmed.

4.2 Methods

4.2.1 Fabrication of microstructures on piezoelectric substrate and magnetization state initialization

The multiferroic heterostructure consists of a (011) cut [Pb(Mg1/3Nb2/3)O3] 1 - x - [PbTiO3] x (PMN-PT, x $\approx$ 0.31) single crystal substrate (Atom Optics Co., Ltd, Shanghai, China). The piezoelectric coupling coefficient d33 of the substrates is between 8001200 pC/N when poled in the [011] direction, and the d31 is -410 pC/N. 5 nm Ti and 50 nm Pt thin films are deposited on both sides of the 1 cm x 1

cm ÃŮ 500 μm thick substrate as electrodes to actuate the substrate in a parallel plate capacitor geometry. Electron beam lithography defines sub-micron features in PMMA A2 resist onto the Ti/Pt surface. Prior to deposition, the PMN-PT is electrically pre-poled in the out-of-plane direction with an electric field of 0.4 MV m^{-1}. A 5 nm Ti adhesion layer and a 15 nm polycrystalline Ni layer were deposited by e-beam evaporation using a CHA Solution electron beam evaporator, with a deposition rate of 0.3 s^{-1}. FeGa (20 nm) was deposited via magnetron sputtering using an Ulvac JSP 8000 (base pressure less than 4 E-7 Torr) at 100 W and a sputtering pressure of 1.0 mTorr. Films were then patterned by a lift-off process, leaving a continuous Ti/Pt layer covering the PMN-PT substrate and sub-micron magnetic features defined on top of this metal layer.

Prior to applying an electric field through the substrate, magnetization states in the ring and square microstructures are initialized by applying and subsequently removing an in-plane external magnetic field (H_{init}) of 0.5 T. The magnetic field is applied in the direction bisecting the directions of the principal strain axes, [100] and [01-1] of the PMN-PT substrate. After the removal of H_{init}, the rings of interest will form 'onion states' [109, 72, 131, 73] with the two onion state domains aligned along the direction of H_{init}, as a result of competition between exchange energy and demagnetization energy. Depending on the aspect ratio between the ring width and ring diameter, the stabilized onion state has two forms of domain walls: transverse or vortex. On the other hand, the microsquares will fall into a full Landau state, or a partial Landau state due to physical imperfections [43, 63]. The direction of H_{init} is so chosen in order to allow a 45° C deterministic rotation of the initialized magnetic state, once the electric field is applied to the substrate [109, 80]. A schematic of the sample with its setup is shown in Fig. 4.1.

4.2.2 XMCD-PEEM for magnetic domain imaging

X-ray magnetic circular dichroism photoemission electron microscopy (XMCD-PEEM) at beamline 11.0.1.1 of the Advanced Light Source of the Lawrence Berkeley National Laboratory is used to image the magnetization contrast in our magnetic structures. Apart from high resolution imaging, other advantages of XMCD-PEEM include element-specificity and non-invasiveness during electric-field sweeps [25]. For this study, XMCD-PEEM is mainly used to characterize the initialized magnetization states in the Ni and FeGa microstructures of different dimensions on PMN-PT at room temperature.

4.2.3 Nanomagnetic particle preparation

Superparamagnetic (SPM) beads with diameter of 0.6 μm and 2 μm (Spherotech, Libertyville, IL) are suspended in distilled water in a 1.5 ml eppendorf tube. The surface of the superparamagnetic microbeads is functionalized with streptavidin to enable bioconjugation for future cell applications.

As shown by this part of the study, using the micro- and nanoscale SPM beads is a powerful method to detect the location of the domain walls on a magnetostrictive microstructure based on the magnetic stray field emanating from it. When methods such as XMCD-PEEM are not easily accessible, this alternative method provides a lab-based tool to image the magnetic domain wall distribution in a straightforward manner. With fluorescent beads, this method allows for imaging with a large field of view where, in this case, arrays of microstructures can be imaged simultaneously. Fig. 4.2 shows the normalized magnetic hysteresis loop of the SPM beads 0.6 μm in diameter, measured by superconducting quantum interference device (SQUID) magnetometry (Quantum Design MPMS 3). For preparation, a drop of beads suspended in the solution was dried on a plastic chip prior to the SQUID measurement.

4.2.4 Trapping of superparamagnetic beads by stray field from Ni and FeGa microstructures

Nanomagnetic particles provide a simple detection method of the magnetic stray field of microstructures. The surface of the nanoparticles is functionalized by different chemical groups to react with specific biological elements. In contrast to conventional methods to detect magnetic domain wall at the nanoscale such with XMCD-PEEM or magnetic force microscopy (MFM), this technique is highly accessible, non-invasive and compatible with in vitro downstream applications.

SPM sub-micron sized beads were introduced to the patterned sample after passivating the surface with pluronic F-127 to prevent non-specific interactions. The beads were allowed to settle and sediment to the sample surface. Non-magnetically attached SPM beads (i.e., non-specific adhesion) were washed off with low flow rates. In the experiments with electric-field induced strain in the PMN-PT, the SPM solution is applied at the center of the sample surface.

4.2.5 Electric-field-driven particle motion

Samples were initialized in an electromagnet and then mounted on a custom chip carrier, after which a droplet of fluid containing SPM beads was placed on the sample surface. Sedimentation and trapping of beads at magnetic domain walls was observed. Upon confirmation of the bead capture, the voltage was increased in steps of 40 V from 0 to 200 V, corresponding to a 0.0-0.4 MV m^{-1} electric field within the piezoelectric PMN-PT substrate. When an electric field is applied to the substrate, the induced strain will alter the magnetic energy landscape, which determines the preferential magnetization direction in either the Ni or FeGa. When a sufficient strain is applied, the magnetization states in both magnetostrictive materials will be modified. Since the magnetostriction coefficients, λ s, of Ni and FeGa have opposite signs, the easy axis in Ni will be reoriented towards the

compressive strain direction [100], while the easy axis in FeGa will be reoriented towards the tensile strain direction [01-1] of (011)-cut PMN-PT.

4.2.6 Optical microscope and Fluorescent microscope imaging and data analysis

The device was viewed using an inverted microscope Nikon Ti-U (Nikon, Melville, NY) illuminated by a mercury arc lamp with 40x and 100x objectives. Fluorescent SPM nanobeads captured on a magnetic array were imaged with a CCD Coolsnap HQ2 camera (Roper Scientific, Evry, France). Images were processed by NIS Elements software (NIS-Elements Package Ver. 4.00, Nikon) to locate in high resolution the trapping location on the domain wall. High-speed videos of microstructures to capture Brownian motion and electric-field-driven motion experiments were recorded using a Fastec IL3 high-speed camera at 1000 frames per second under bright field illumination.

4.2.7 Microfluidics integration

A PDMS device was fabricated with standard soft-photolithography to form a channel (H = 100 μm, W = 0.5 cm, L = 0.5 cm), as shown in Fig. 4.2. The master wafer was patterned with KMPR 1050 (Microchem Corp., Woburn, MA, USA). PDMS (Sylgard 184, Dow Corning, Midland, MI, USA) was mixed with a curing agent at a 10:1 weight ratio. The mixture was poured onto the master wafer and degassed to remove air bubbles. The PDMS was cured at 100 °C overnight. Microchannel devices were cut out and aligned on the surface of Ni/(001)-PMN-PT and FeGa/(001)-PMN-PT multiferroic heterostructures after an inlet and outlet were punched connecting to upstream and downstream portions of the channel. The bonded microchannels are capable of steering the flow and perform washing steps to test multiple SPM bead trapping events on the same device. Fig. 4.3

shows the integration of the microfluidic chip on the surface of the magnetoelectric device.

4.2.8 Cell viability test

Jurkat leukemia cells (ATCC, Manassas, VA) were grown in RPMI 1640 media containing 10 % fetal bovine serum (Invitrogen, Carlsbad, CA). Cells are cultured at 37 °C in a humidified atmosphere of 5% CO2. Cell viability is determined by Calcein AM green fluorescence stain (Thermo Fisher, Waltham, MA).

4.3 Results and discussion

4.3.1 XMCD-PEEM imaging of the microstructure arrays and localized fluorescent bead trapping

Upon removal of the initializing magnetic field (H_{init}), Ni and FeGa rings relaxed into onion state domains while squares relaxed into Landau states due to energy minimization between exchange and demagnetization contributions. XMCD-PEEM characterized the domain configuration in the microstructures by spatially resolving the magnetization contrast, where black and white indicate the magnetic orientation pointing to the right (0°) or to the left (180°), respectively, in the figures below.

Fig. 4.4a displays the XMCD-PEEM images of Ni microstructures at initialization, showing onion states in rings. Fluorescent SPM micro- and nanobeads are used to pinpoint the location of the onion state domain walls, which are local sources of magnetic stray field, and bead trapping locations using the same magnetic initialization protocol as used for the XMCD-PEEM samples. As an overlay of bright field and fluorescent microscope images, Fig. 4.4b presents arrays of Ni rings of outer diameters 2 μm - 6 μm capture fluorescent beads at the DWs

location of the onion state. A series of time-lapse images of an array of Ni rings with OD of 4 μm, and w of 350 nm capturing beads is shown in Fig. 4.4c.

Fig. 4.3d shows the XMCD-PEEM images of Ni square forming a Landau flux-closure state with four triangular domains (magnetic vortex state [18]). Although the Landau state forms to minimize the demagnetization energy, the magnetization at the center of such vortex state points out of the plane to avoid drastic increase in exchange energy. Both Hall micromagnetometry and micromagnetics simulation studies on Landau state by Breitenstein et al [16] suggested that the z-component of the stray field from the vortex core with a few nm in size becomes completely masked by the stray field from the domain walls from the four triangular domains at around 90 nm in their permalloy squares of 2 μm in length and 20 nm in thickness. This helps to explain that with magnetic particles with diameter more than 0.5 μm, the trapping by the vortex core with only a few nanometers in diameter and limited z-direction stray field range was not observed. Instead, consistent trappings occur at multiple corners of the squares (see Fig. 4.4e), indicating the partial flux-closure domain state produces high stray fields at the corners. Furthermore, according to a recent XMCD-PEEM study based on Ni microsquares on PMN-PT [18], the squares do not always form 'perfect' flux-closure Landau state (see Fig. 4.4d). Fig. 4.4f shows the time-lapse images of a square of 2 μm in length capturing a bead at the corner. Combined with the bead trapping experiment, it can be observed that the initialized magnetic vortex state produces strong stray field at the corners of the squares. Such partial closure domain occurs due to several reasons: (1) physical imperfections of the fabricated micron scale structure with 15-20 nm in thickness, and (2) initial non-uniform magnetic uniaxial anisotropy could also contribute to the deviation from a perfect Landau state.

When no flow is applied and particles are simply allowed to sediment, high-speed camera footage of the trapping event shows that motion stops quickly upon

interaction of the particle with the domain wall of a Ni ring, confirming the strong magnetic interaction between the bead at the domain wall that has sufficient energy to overcome thermal energy. In particular, prior to the moment of capture, the particle moves randomly (see Fig. 4.5, suggesting that the observed motion is from Brownian diffusion and/or environmental vibration. The sudden decrease of the amplitude of this motion upon encountering the domain wall and its failure to reoccur thereafter must be from a localized pinning potential the particle experiences, in this case due to the magnetic field gradient from the domain wall.

To investigate whether higher magnetostrictive FeGa microstructures follow similar paradigm of Ni microstructures, microstructures of similar dimensions are also examined. Fig. 4.6a shows the XMCD-PEEM images of individual FeGa rings with outer diameters (OD) of 6 μm, 4 μm, and 2 μm, and widths (w) of 300 nm, 350 nm and 300 nm, respectively. With the desired onion states confirmed by XMCD-PEEM, fluorescent SPM micro- and nanobeads are used to confirm the one-to-one correspondence between the location of the onion state domains (see Fig. 4.6b). For FeGa squares of 2 μm in length, the beads are observed to be trapped on the corners, as shown in Fig. 4.6c. Fig. 4.7 shows the time-lapse images of an array of FeGa rings capturing beads, along with the process of bead capturing by the rightmost No. 3 ring. The three rings shown here have a diameter of 2 μm and width of 300 nm.

4.3.2 Strain profile characterization

Previously, Sohn et al [5] demonstrated the morphotropic transformation when PMN-PT transitioned from rhombohedral to orthorhombic in (011)-cut PMN-PT, inducing a large, nonlinear strain jump to the substrate at 0.5 MV m^{-1} [5]. The transformation initiated abrupt particle motion to a full 45° rotation instantaneously. This study focuses on a PMN-PT with a different composition, resulting in a linear strain profile with electric field, as shown in Fig. 4.8. The

strain profile was measured by attaching a biaxial strain gauge onto the surface of the sample. As we apply electric field of various magnitudes, the induced strain will result in a change in the electrical resistance that is proportional to the strain magnitude. With a linear strain profile, we expect a smoother modulation of the magnetic particle position along the perimeter of the ring as the electric field is applied across the substrate.

4.3.3 Electric-field-driven particle displacement

Though electronically actuated particle motion in multiferroic heterostructures like these has been demonstrated previously using PMN-PT substrates with a nonlinear strain response [5], actuation using linear strain response is more desirable due to the potential for controllable, continuous particle motion. Due to the linear strain, within a certain range of applied fields the particle displacement is also expected to be proportional with respect to the electric field. However, as the magnitude of the strain response is lower in these linear strain samples, it was necessary to demonstrate that actuation of domain wall motion is still possible at nondestructive electric field strength. To this end, stepwise voltage was applied to PMN-PT substrate with Ni microstructures after particle trapping.

Successful, electrically driven continuous particle motion was observed for particles trapped on Ni rings, wherein a trapped magnetic particle rotated through several intermediate angles as the applied voltage was increased until aligned with the compressive strain axis [100] of the PMN-PT substrate (see Fig. 4.9). No other motion of the trapped particles during this process was observed, including any reoccurrence of the random diffusive motion described above, suggesting that the particles remain trapped during the domain wall motion. This distinguishes these motions from the large, nonlinear strain-mediated displacements observed in Sohn et al [5], in which the particles were moved in one step or even ejected from the domain wall due to the sudden DW rotation.

Interestingly, however, magnetic beads trapped at the corners of the squares of 2 μm, either in Ni or FeGa, remain stationary after the application of electric field, with an example of a Ni square shown in Fig. 4.10. Lo Conte et al [18] has recently reported more details of electrical-field induced domain state change in Ni 2 μm squares. One explanation is that as the magnetic vortex state (Fig. 4.10a left) becomes a two-domain state whose domain wall aligns with the compressive strain axis in [100], the high energy density of the magnetic stray field still exists at the diagonal corners of the square. Taking into account the non-uniformly distributed strain in the substrate and imperfections from fabrication, the domain wall of the two-domain state does not always overlap perfectly with the diagonal of the square, leading to the locations of the bead trapping laying slightly away from the corner of the square. However, compared to the particle motion with respect to the ring, the particle captured by the corner of the square stabilizes at the same location. The different responses of magnetic particles to the two different geometries of the microstructures suggest a way to pattern various microstructures on the same device with different degrees of freedom for strain-mediated particle control, when compared to micropatterned magnetic arrays without such multiferroic control.

4.3.4 Cell viability on magnetoelectric devices

To investigate the cell viability [111] on the magnetoelectric devices with applied electric fields up to 0.8 MV m^{-1}, live Jurkat cells are stained with Calcein AM green fluorescent dye. Cell membrane damage causes the green dye to escape, indicating cell death. Stained cells were settled on the Pt electrode covering the PMN-PT substrate. Cells remained viable when voltage was applied up to 400 V, corresponding to an electric field of 0.8 MV m^{-1} (Fig. 4.11). This indicates cytocompatibility of the platform for in vitro cell biomedical applications while actuating a magnetoelectric device with adequate packaging.

4.4 Summary

In summary, we have demonstrated the trapping of sub-micron magnetic particles by magnetostrictive Ni and FeGa microstructures at specific locations, including onion state domain wall of the ring structures, and partial flux-closure domain at the corner of squares. XMCD-PEEM shows the magnetic domains in both Ni and FeGa microstructures, while optical and fluorescent microscope captures how the beads interact with the domain walls, highlighting an alternative non-destructive method of indirectly visualizing the domain wall locations in these magnetostrictive microstructures. The linear strain response when electric field is applied through the thickness of the PMN-PT substrate enables a steady and continuous translational movement of the magnetic bead to the newly electrically introduced magnetic easy axis. The cytocompatible device provides a promising pathway to develop multiplex particle and cell manipulation platforms with sub-micron precision.

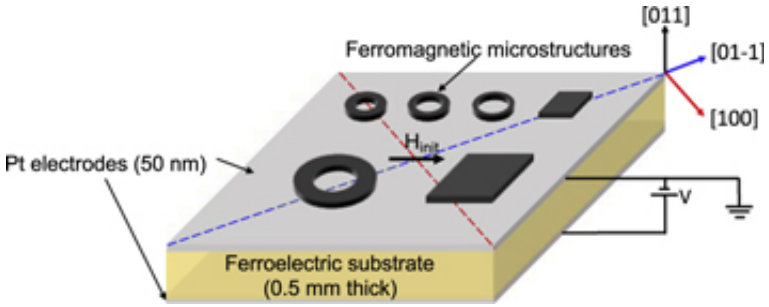

Figure 4.1: Schematic of the sample and the relative orientations between the initial field direction and the PMN-PT principal strain axes. After the initialization field, H_{init}, is removed, an electric field is applied through the thickness of the ferroelectric PMN-PT via the top and bottom electrodes made of Pt thin films, inducing a differential in-plane strain.

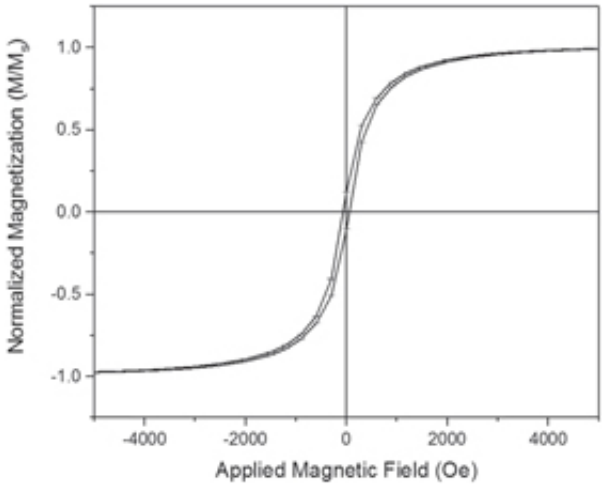

Figure 4.2: Magnetization hysteresis loop measured by SQUID magnetometry for a suspension of the superparamagnetic nanobeads (600 nm in diameter) used for the fluorescent imaging.

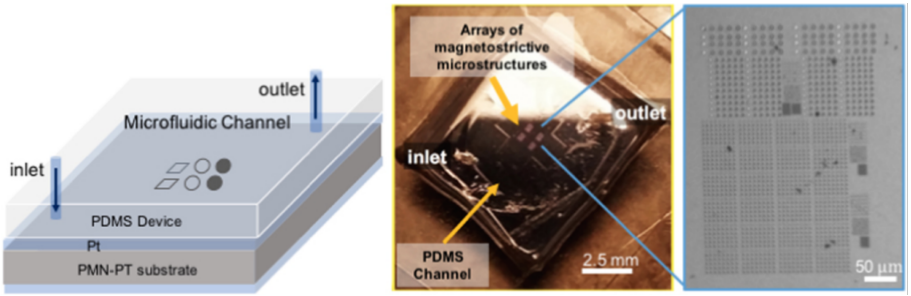

Figure 4.3: Microfluidic chip integrated on the top surface of the magnetoelectric device. Arrays of magnetostrictive micropatterns are located at the center of the device, viewed by optical microscopy.

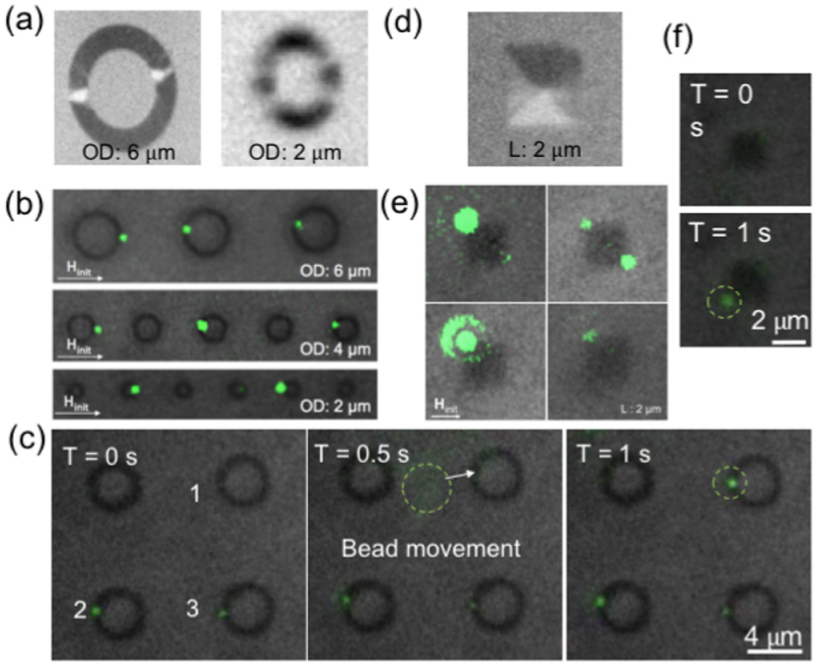

Figure 4.4: Fluorescent beads of 0.6 μm (green) trapped and localized on the magnetic domain walls of the Ni microstructures. (a) XMCD-PEEM images of Ni rings. (b) Overlay of bright field and fluorescent microscope images of fluorescent beads coupled to rings of 6 μm, 4 μm, and 2 μm in diameter. (c) Time-lapse images of 4 μm Ni rings capturing fluorescent bead (0.6 μm in diameter) in the microfluidic channel, corresponding to the location of the DWs of Ni rings, as shown in the PEEM images. (d) XMCD-PEEM images of Ni squares with 2 μm in length. (e) Overlay of bright field and fluorescent microscope images of fluorescent beads captures at the corners of 2 μm squares. (f) Time-lapse images of FeGa squares of 2 μm in length capturing fluorescent bead at the corner. Dashed circle highlighted the position of the fluorescent bead.

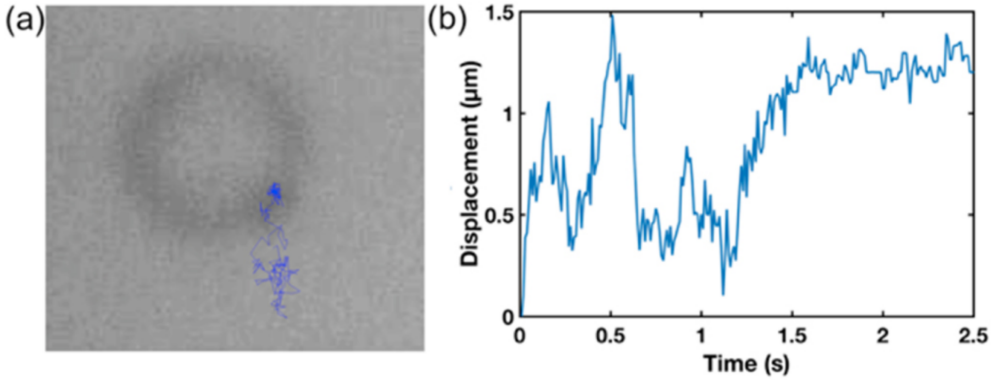

Figure 4.5: (a) Representative particle trapping event in the absence of flow (1 μm particle, 4 μm diameter ring. Left: particle path overlaid on image of 4 μm Ni ring. (b) Particle displacement relative to position at time 0 (Euclidean distance) vs time over the course of the trapping event. Trapping occurs around 1.5 s and most random motion ceases.

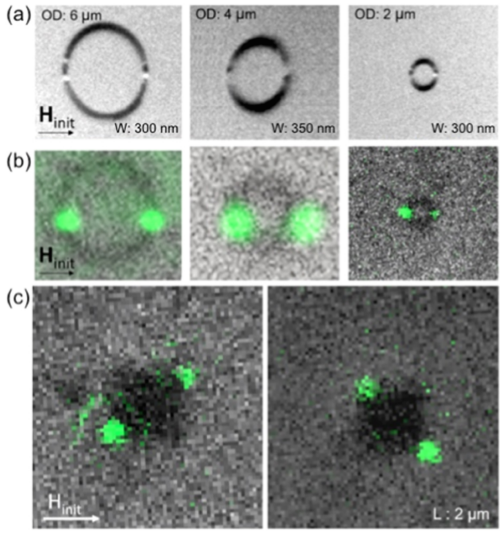

Figure 4.6: (a) Initialized onion states in polycrystalline FeGa rings of varied width and diameter, with a thickness of 20 nm, observed by XMCD-PEEM. (b) Rings of various sizes in (a) trapping fluorescent nanoparticles via the magnetic stray field emanating from the onion state domain. (c) Squares of 2 μm in length trapping fluorescent particles on the corners.

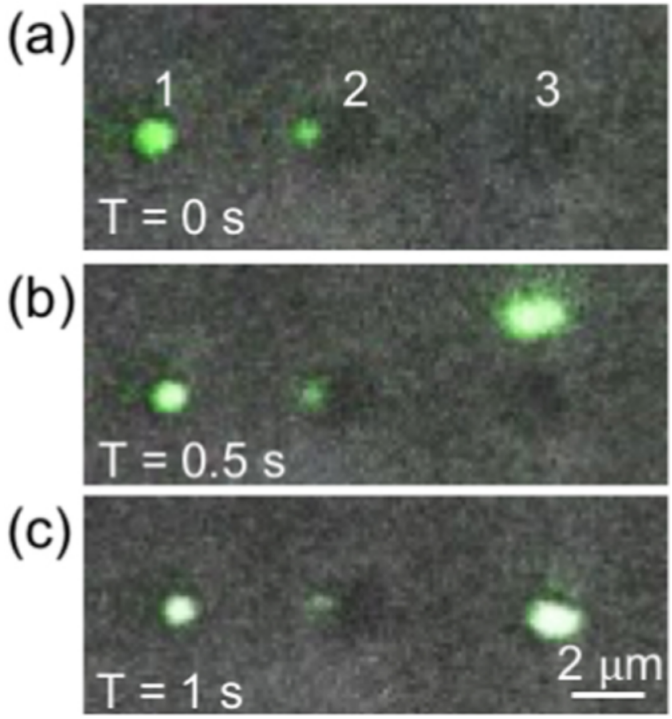

Figure 4.7: Time-lapse images of 2 μm ring (No. 3) capturing a fluorescent bead in the microfluidic channel, corresponding to the location of the DWs of FeGa rings, as shown in the PEEM images. Ring No. 1 and No. 2 have captured beads prior to No. 3. All the three rings trapped beads locally along the x direction, in which H_{init} was applied.

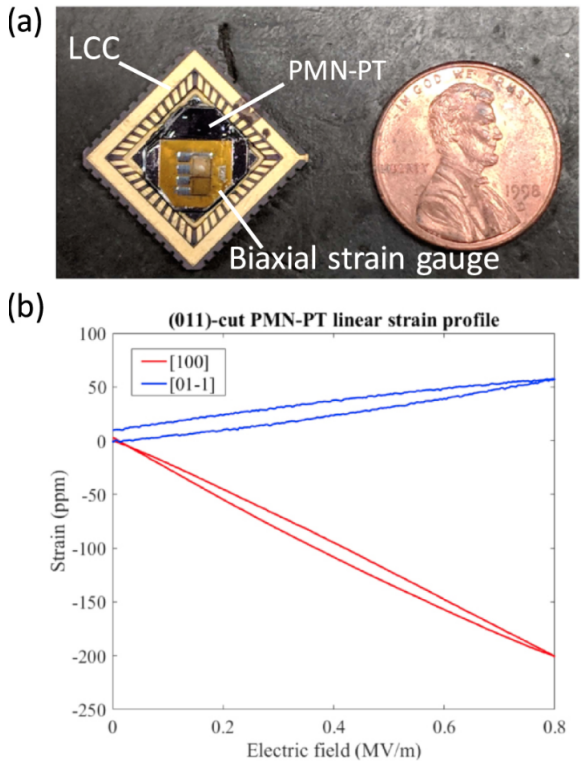

Figure 4.8: (a) Magnetoelectric device is mounted on a leadless chip carrier (LCC), and a biaxial strain gauge is mounted on the surface of the device for strain profile characterization. (b) Linear strain response along the [01-1] and [100] directions of the PMN-PT substrate to the applied electric-field is measured using the strain gauge.

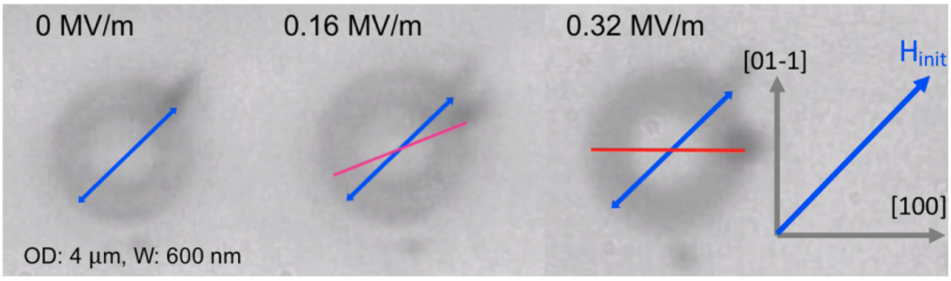

Figure 4.9: Continuous magnetic bead movement, driven by applied electric field to the PMN-PT with linear strain response, along the perimeter of the Ni ring, 4 μm in diameter and 600 nm in width, captured by optical microscope. The diameter of the bead is 1 μm.

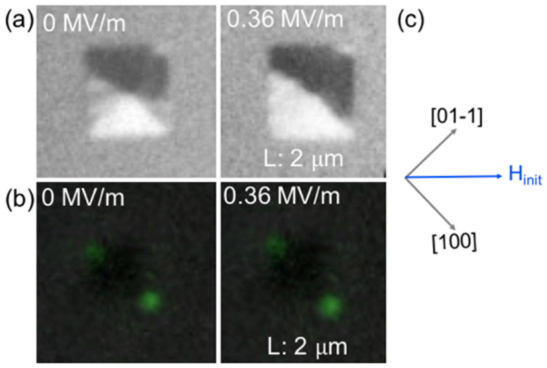

Figure 4.10: (a) XMCD-PEEM images of a Ni square with a magnetic vortex state at zero electric field, and evolves into a two-domain state at 0.36 MV m^{-1}, (b) a Ni square of 2 μm in length trapping fluorescent beads on the corners before and after applying voltage and (c) Sample orientation with respect to the initialization magnetic field direction.

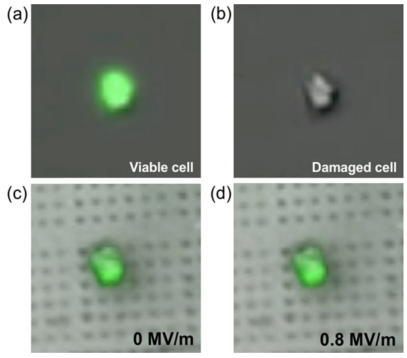

Figure 4.11: Viability test on multiferroic heterostructure platform using Calcein AM stain (a) stained viable cells, (b) stain leakage of damaged cells, (c) before applying voltage and (d) after ramping up the voltage to 400 V applied to the top and bottom electrodes, with corresponding electric field up to 0.8 MV m^{-1}, the cells are viable for downstream bio-applications.

CHAPTER 5

Programmable Single Domain Terfenol-D Micromagnets for Single-cell Manipulation

5.1 Introduction

Sorting engineered cells with unique properties or functions from a larger population is a promising method to improve the function of cell therapies [40, 39]. Cells can be imbued with magnetic properties by binding specific cell membrane proteins with functionalized superparamagnetic particles [87]. Once functionalized, an external magnetic field ($\mathbf{B}$) can remotely control the bulk migration of magnetically labeled cells in complex fluids (e.g. blood) [116]. This approach has allowed for separating specific subpopulations of cells from a mixture based on surface antigen expression. However, surface antigen expression alone may not uniquely define cells in a functional manner of importance to new single cell-based assays. For example, a single-cell possesses many other medically relevant phenotypic properties like the level of cell receptor expression and kinetics [101], cytokine secretion [89], cell-cell interactions [114] and phosphorylation state of signaling pathways [10]. Thus, there is a need to individually select the best performing cells based on multiple phenotypes. To achieve this, programmable and localized control of a magnetic array is needed to individually manipulate cells based on different phenotypes.

A bulk external magnetic field ($\mathbf{B}$) with a high field gradient is unnecessary for cell localization and can be detrimental for accurate control. Only a few

micrometers of attractive magnetic field are needed to hold micrometer-scale labeled magnetic particles on a cell membrane. For bulk fields, the long-range magnetic bulk migration of cells causes cell clumping and aggregation preventing single-cell separation and release for downstream analysis. In addition, external magnetic field ($\mathbf{B}$) inhomogeneity over larger distances can inhibit the ability to array single-cells in a 2D space to image and analyze the phenotypic heterogeneity between individual cells. Coupling soft magnetic elements with a bulk field can improve single-cell localization, but large-scale inhomogeneous magnetic field gradients ($\mathbf{B}$) still lead to non-uniformity in arraying cells [22]. This also causes cells to be held with different magnetic forces which hinders the ability to uniformly and precisely control specific single-cell release using other non-magnetic competing forces (e.g. hydrodynamic, optical, acoustic, electrical). Lastly, the presence of a bulky permanent magnet or electromagnets hinders real-time imaging and phenotypic profiling for a visually controlled cell sorting decision [95].

The need for an external magnetic field ($\mathbf{B}$) to magnetize ferromagnetic elements can be overcome by using magnetoelastic materials with strong and tunable intrinsic magnetic properties at the micro/nanoscale [102]. Magnetoelastic materials have been extensively studied in the past decade for a broad range of energy-efficient applications, including non-volatile memory [13], actuators [136] and transducers [49], but have never been explored for cell manipulation applications. Stray fields (H_s) associated with single magnetic domains can be set at the microscale by an initialization field (H_{init}) replacing inhomogeneous external magnetic fields ($\mathbf{B}$). However, highly localized stray fields associated with typical single magnetic domains nanostructures are too small and weak for magnetic particle capture alone (Table 3). Microstructures of magnetoelastic materials form multi-domain state [41] and yield non-uniform magnetic flux near microstructures. Larger single domain states (> 1 μm) can be more effective for magnetic trapping and manipulation due strong (1 M_r) uniform stray field (H_s) (Fig. 5.1), but

have been unachievable with current magnetoelastic microstructures.

This work demonstrates the largest effective single domain ever reported in magnetoelastic Terfenol-D microstructures. The magnetically initialized single domain in Terfenol-D is 10 fold larger than previous studies with a remnant magnetization Mr of 0.85 the saturation magnetization Ms, exhibiting a coercivity 100 fold larger than that of soft magnetic elements like Permalloy. These enhancements of magnetic properties lead to the independence from external magnetic field (**B**) with a strong localized stray field (H_s) trapping of 2.5 μm from the microstructure surfaces. Highly localized and uniform magnetic fields around each microstructure enabled coupling of external hydrodynamic forces to specifically control cell release from stable and cytocompatible Terfenol-D micromagnetic cell traps. This technology introduces a new level of capability to magnetic cell sorting through the precision control of magnetic field direction and magnitude using precisely manufactured micro-magnets. More importantly, it paves the way to high-throughput multiferroics-based cell sorting driven by localized electrically induced strain, to modulate magnetic field in an addressable manner across a parallel array of microstructures.

5.2 Results and discussion

5.2.1 Terfenol-D single domain micromagnets

Terfenol-D ($Tb_{0.3}Dy_{0.7}Fe_{1.92}$) microdisks are highly coercive with 0.23 T of coercivce field and 710 and 600 emu/cc of saturation (M_s) and remanent (M_r) magnetization, respectively, as measured by the superconducting quantum interference device (SQUID) (Fig. 5.2b). Single domain states were imaged for 3 μm Terfenol-D microdisks after being saturated with an in-plane magnetic field H_{init} of 0.5 T. Terfenol-D microdisks formed single domain magnetic states at remanence in both 3 μm and 20 μm disks. Magnetic Force Microscopy images (MFM) of 3

μm disks yielded evidence of single domain, (Fig. 5.2a). Similarly, using X-ray magnetic circular dichroism photoemission electron microscopy (XMCD-PEEM), we visualized effective single domain states in individual 20 μm Terfenol-D microdisks (Fig. 5.2c). Some magnetic moments are slightly canted away in-plane from the initialization field direction, as indicated by the grey grains in the PEEM micrographs of the disks, while the entire disk functions collectively as a single domain for particle and cell trapping purposes. Other magnetoelastic materials break into multi-domain state (right side) around 1 μm in diameter (Fig. 5.3, table 3).

5.2.2 Single domain uniform micromagnetic trapping

Real-time imaging of micro-particle capture/release dynamics is enabled by patterning Terfenol-D microstructures on transparent sapphire (Fig. 5.4s). Magnetic particles without an external magnetic field (**B**) were specifically attracted to the x-axis poles stray field (H_s), the direction of initialization of Terfenol-D microstructures, with saturation magnetic field (H_{init} = 0.5 T) (Fig 5.4b). In contrast to multi-domain FeGa of the same microstructures, Terfenol-D exhibit precise and symmetric localization of magnetic particles (Fig. 5.5). Uniform magnetic localization and trapping are observed across the micropattern (Fig. 5.6). Presumably this is due to single domain state that is lacking in FeGa. Stray field (H_s) trapping surface space r(θ) can be tuned by disk diameter to control forces around the targeted single-cell size. Functional and similar behavior of uniform and localized single domain trapping in a variety of thin film microstructure geometry proves the ability of manufacturing micro-magnets with consistent uniform single domain field in any arbitrary microstructure (Fig. 5.7).

The stray field (H_s) attracts suspended magnetic particles within 2.5 μm from surface of the magnetized poles of Terfenol-D microdisks (Fig. 5.8a). Microparticles exhibit random Brownian motion then exponentially accelerate towards

the magnetic pole and settle in the magnetization axis ($\theta = 0$)(Fig. 5.8b). To create a functional trapping array, distance between two neighboring microstructures should be larger than stray field range of influence. Small gaps (<5 μm) in the microarray, where interference occur between stray fields (H_s) from neighboring microdisks, leads to low particle trapping and accumulation (Fig. 5.8c). At sufficient gap distance, dipole interactions are more pronounced in which magnetic beads (diameter < 5um) formed chains and bridges between magnetized axes of Terfenol-D disks (Fig. 5.8d).

5.2.3 Single-domain magnetic localization

Another unique property of magnetoelastic single domain Terfenol-D microstructures is the ability to precisely program or tune magnetic trapping location by changing the initiation magnetization $H_{init}(\theta)$ axis. Magnetic particles in flow are trapped on the programmed y-axis and a diagonal line (θ=45 °) separately on all Terfenol-D microstructures with high precision. (Fig. 5.9). Programmed micro-trapping locations can be utilized to attach two different particles on one micromagnet with two magnetization steps. After nanoparticles are localized along the initial magnetization x-axis (θ=0 °) (green fluorescence), the same sample is later magnetized again along the y-axis (θ=90°). While nanoparticles from the previous step remain attached, other particles that are added in the second step (orange fluorescence) are localized along the y-axis, in close proximity (1 μm away from the first nanoparticle) (Fig. 5.10).

In the presence of an external permanent magnet, micromagnetic particles are moved toward the external magnetic field ($\mathbf{B}$), but once it enters the micropattern region, it dramatically change their trajectory toward the magnetized poles of the Terfenol-D microdisk (Fig. 5.11). Trapped particles are not removed outside the programmed trapping domain of the microdisk by external field of the permanent magnet, which demonstrates the dominating high coercivity of the programmed

Terfenol-D micropattern over the limited influence external magnetic field (**B**). However, micromagnetic particles are instantly detached and reassembled back to their programmed magnetized locations when disturbed by a water drop. This demonstrates uniform and strong magnetic stray field (H_s) near its surface and the capability to couple external non-magnetic forces to tune particle release from the programmed micro-location, which is discussed in the next section.

5.2.4 Programmable multiferroic magnets for particle and cell capture/release

Uniform and localized magnetic particle binding force (F_m) is held constant across the single domain Terfenol-D microarray, which is key to array addressability. Overlaying a competing external non-magnetic force to one magnetic microdisk enabled selective particle and cell release from the microarray while others are still attached. An experimental demonstration of magnetic particle/microstructure stray field (H_s) interference by external hydrodynamic drag force (F_d) at different flow conditions show three stages of particle capture, tumble and release on Terfenol-D micropattern (Fig. 5.12). (1)- magnetic particles are captured or maintained on Terfenol-D microdisks when magnetic binding force dominates over hydrodynamic drag ($F_m > F_d$). (2)- when the magnetic binding force and hydrodynamic drag are similar ($F_m \approx F_d$) at higher flow rates, magnetic particle tumble or jump between Terfenol-D trapping regions with a short stop (i.e. binding time) on the magnetized axis. The average binding time of the particles on the Terfenol-D disk decrease at higher flow rates as particles move faster across the magnetic trapping domain. (3)- lastly, when hydrodynamic drag dominates over magnetic binding force ($F_m < F_d = 14$ pN), magnetic beads are released instantly with limited stray field (H_s) influence of the downstream neighboring disks in Terfenol-D micropattern (Fig. 5.13a). Interestingly, the magnetic binding forces of different size beads (2.8 and 9.1 μm) were very similar (Fig. 5.13b). This

result is explained by the uniform decay of the low stray field gradient (H_s) (2.5 μm), which interacts with similar magnetic content regardless of the particle size.

Magnetic cell capture by Terfenol-D microdisks (20 μm) with large surface stray field (H_s) are used to match the same size scale of single-cells (average diameter = 10 μm) to array one cell per micromagnet (Fig. 5.14a). Cells were uniformly arrayed and precisely captured on the magnetization axis poles of the microstructures. Centroids of cells on microdisks without clumping. To trap large cell clusters, we switch the magnetization axis to align them between two microdisks gaps. To test selective cell capture/release in flow, cells were captured by Terfenol-D micropattern with flow conditions where magnetic binding force dominates over hydrodynamic drag ($F_m > F_d$) (Fig. 5.14b). Then higher flow condition are applied ($F_m < F_d$) were all captured cells are uniformly released. Captured cells are cultured and grown on fabricated Terfenol-D disk arrays that prove cytocompatibility for selective cell expansion for downstream cell therapy applications (Fig. 5.14c). The utility of capture/release goes beyond cells, as encapsulated cell droplet captured and released. Lastly, single-particles and cells were released from Terfenol-D micro-magnets on pmn-pt substrate by voltage induced strain (Fig. 5.15).

Autonomous and tunable magnetic trapping via single domain microstructures enables uniform single-cell captures and release in large arrays. This finding enable visually controlled selective cell expression of multiplexed medically relevant properties, and individually release and expand cell lines that show high performance phenotypic properties.

5.3 Methods

5.3.1 Film deposition and micropatterning

Terfenol-D thin films were deposited by DC magnetron sputtering using a Tb0.3 Dy0.7 Fe1.92 (Terfenol-D) alloy target obtained from TdVib LLC. USA. The following process parameters were used for the Terfenol-D deposition onto a 100 mm diameter Silicon (100) wafer and a 50 mm diameter (0001) sapphire wafer. The sputtering parameters are 250 Watts of sputtering power, substrate-to-target distance of 5.5 cm, Ar gas pressure of 5 mTorr, and a substrate temperature of 250 °C. Prior to the Terfenol-D deposition, 10 nm thick Tantalum metal (Ta) was deposited onto the substrates as a barrier layer and after the Terfenol-D deposition, 4 nm thick Ta was deposited as a protective layer to avoid oxidation. Following Ta deposition, the film was post-annealed in-situ at 450 °C for 4 hours at chamber pressure below 5 x 10-6 Torr. Terfenol-D micropatterns were fabricated using a conventional photolithographic method. The process consists of (i) spin coating of negative photoresist AZ nLOF 2020 on the Ta capping layer, (ii) UV exposure using Karl Suss mask aligner to transfer the pattern (3 and 20 micron diameter disks) from the mask onto the thin film by hardening the photoresist, (iii) development of the photoresist with AZ MIF 300 developer by dissolving the unexposed soft photoresist, (iv) loading the film with hardened photoresist into STS-AOE etcher to etch away the unexposed film with Ar ions. The etched films were ultrasonicated in acetone to remove the photoresist.

5.3.2 Scanning electron microscopy imaging (SEM) and Magnetic Force Microscopy (MFM)

The micrographs of the arrays of Terfenol-D microdisks were acquired by a Hitachi S4700 scanning electron microscope (SEM). The magnetization state of the 3 μm disks was characterized with magnetic force microscopy (MFM), using a BRUKER

ICON Magnetic Force Microscope where the tip was raised 50 nm away from the sample surface, and with a 75KHz.

5.3.3 Magnetic hysteresis loop: Superconducting quantum interference device (SQUID)

The room temperature in-plane magnetization versus applied magnetic field plot for the crystallized Terfenol-D film using SQUID magnetometer procured from Quantum Design, USA. The measurements are made by sweeping between -1 T and 1 T. The magnetic hysteresis loop measured by SQUID for the etched 3 μm disk arrays has a saturation magnetization M_s of 810 emu/cc, close to the bulk Terfenol-D M_s of 800 emu/cc. This suggests that the hybrid crystallization process, substrate temperature and post annealing produce a reasonable M_s. The square hysteresis loop suggests a relatively hard magnetic material with (Mr/Ms) of 0.85. The coercive field value is 2300 Oe, suggesting a hard magnetic material which is not representative of the soft bulk Terfenol-D. The large coercivity and remanence values are largely attributed to the intrinsic residual stresses that arise during the deposition process. While there is a small contribution from the thin films shape anisotropy this is insufficient to produce the large values measured. The residual stresses produce a large magnetoelastic induced in-plane easy axis producing both high coercivity and high remanence.

5.3.4 Magnetic domain imaging by X-ray magnetic circular dichroism photoemission electron microscopy (XMCD-PEEM)

The magnetization orientations in Terfenol-D microstructures were characterized by x-ray magnetic circular dichroism photoemission electron microscopy (XMCD-PEEM) at beamline 11.0.1 of the Advanced Light Source, Lawrence Berkeley National Laboratory. Prior to imaging, the sample was plasma etched in-situ

in the vacuum chamber by Argon for an hour to etch off the 4 nm Ta capping layer which prevents the Terfenol-D microstructures from oxidizing. The sample was subsequently transferred into the PEEM chamber from the etching chamber. The x-ray absorption spectrum (XAS) of Fe was acquired by scanning the photon energy in the range of 695 to 730 eV. The measured XAS matched that of unoxidized Fe, implying the Ta capping layer protected well the reactive Terfenol-D microstructure. The x-ray energies were then tuned to the energies of Fe L3 (706.9 eV) and L2 (719.9 eV) absorption edges, respectively. Two images were taken at the same location for each absorption edge energy by left and right circularly polarized x-ray. A numerical division of the two images pixel by pixel provided the XMCD-PEEM image. In addition, the XMCD-PEEM images were also taken at the energy of Tb and Dy M5 edge to confirm the coupling behavior between the elements and ferrimagnetic behavior of Terfenol-D. The measurements were performed in vacuum at room temperature with no external magnetic field.

5.3.5 Microfluidic device integration

Two microfluidic devices were designed to charachterize trapping regions of Terfenol-D microstructures and to perform indirect measurement of magnetic binding forces of stray field (H_s). A PDMS microchannel is fabricated with standard soft-photolithography and replica molding described previously. PDMS (Sylgard 184, Dow Corning, Midland, MI, USA) was mixed with a curing agent at a 10:1 weight ratio. The mixture was poured onto the master wafer and degassed for one hour to remove air bubbles then cured at 100 °C overnight. Microchannel devices were cut out and aligned on the surface of Terfenol-D micropattern on sapphire. All surfaces are passivated to prevent non-magnetic binding or adhesion with surfactant (Pluronic F127). Magnetic beads with diameter of 0.4-9.1 μm (Spherotech,Libertyville, IL) are suspended in distilled water. Magnetic microbeads surface is functionalized with fluorescent dye to enable localization of

beads on Terfenol-D microdisks.

5.3.6 Microscopy imaging and image analysis

The device is viewed using an inverted microscope Nikon Ti-U (Nikon, Melville, NY) illuminated by a mercury arc lamp with 4x - 100x objectives. Fluorescent micro and nanobeads captured on a magnetic array were imaged with a CCD Coolsnap HQ2 camera (Roper Scientific, Evry, France). Images were processed by NIS Elements software (NIS-Elements Package Ver. 4.00, Nikon) then analyzed by an in-house MATLAB code to overlay fluorescent images of beads distribution on Terfenol-D microdisks.

5.3.7 Cell Culture and labeling

Jurkat leukemia cells (ATCC, Manassas, VA) were grown in RPMI 1640 media containing 10 fetal bovine serum (Invitrogen, Carlsbad, CA). Cells are cultured at 37°C in a humidified atmosphere of 5 %CO2. Cell viability is determined by Calcein AM green fluorescence stain (Thermo Fisher, Waltham, MA). Cells are then cultured on the surface of fabricated Terfenol-D disks in media.

5.4 Summary

A precise control of magnetic fields at the microscale can enable interfacing at the scale of cellular and molecular biology. We demonstrate patterned microstructures of a magnetoelastic material, Terfenol-D with the largest magnetically initialized single domain state. Terfenol-D microstructures controlled the localization of magnetic particles with sub-micron precision. Magnetically labeled cells were also captured without an external biasing magnetic field. Magnetic cell separation and manipulation based on control of individual micro-magnetic elements in an array

can provide a platform for parallelized cell sorting based on complex phenotypes.

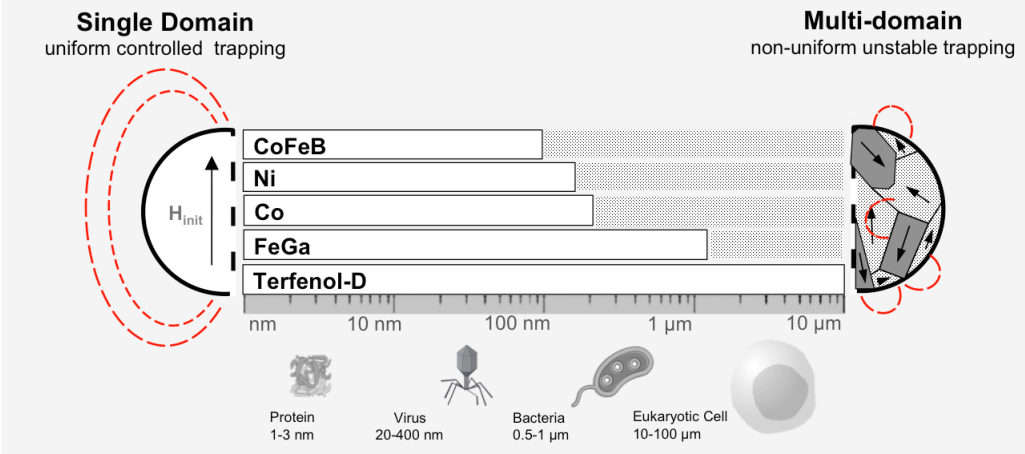

Figure 5.1: Schematic of single-domain magnetics potential upgrade in bio-applications precision and control at the micro-scale. Single-domain size limit (left side) of magnetically initialized magnetoelastic material. Terfenol-D has the largest single domain state (20 μm). Single-domain stray field (red dotted lines) are strong, uniform and tunable to magnetically control a wide range of cell sizes. Other magnetoelastic material breaks in multi-domain state (right side) around 1 μm in diameter.

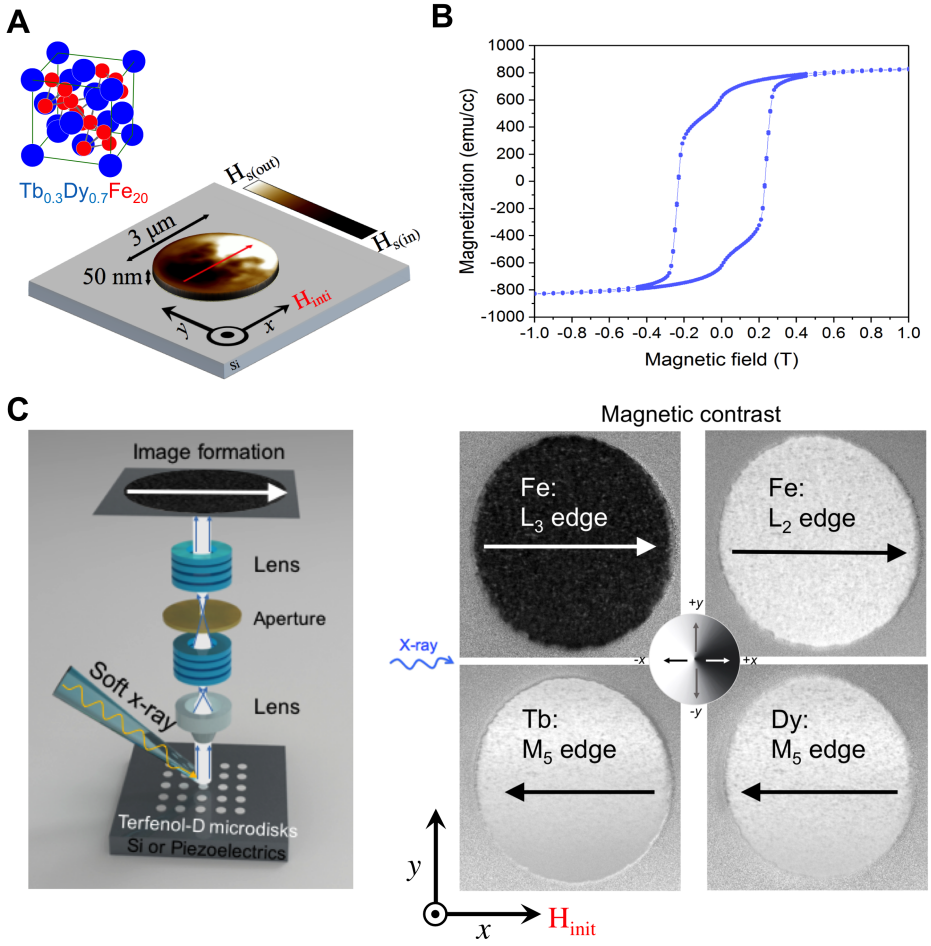

Figure 5.2: Magnetic characterization of Terfenol-D microstructures. (A) Terfenol-D microdisks on Si 50 nm thick, diameters of 3 μm and 20 μm) show single domain configuration with Magnetic force microscopy imagin.(B) Magnetic hysteresis loop of the Terfenol-D disks of 3 μm in diameter shows large saturation magnetization of 780 emu/cc and a coercivity of 0.23 T, as measured by SQUID. A large fraction of the magnetization is retained upon the removal of saturation magnetic field. (C) The x-ray absorption spectrum with the Fe edges confirms the non-oxidized state of the Terfenol-D microstructure. The XMCD-PEEM image is acquired after in-situ etching that removes the 4 nm thick protective Ta layer on the Terfenol-D. Magnetic contrasts taken by PEEM at the elemental absorption edges of all three elements (Tb, Dy, Fe) in the Terfenol-D confirm the single domain configuration in the 20 μm Terfenol-D microstructures. The black contrast indicates the magnetization is pointing along the +x direction; the white indicates the magnetization is pointing in the -x direction. The entire disk functions nearly as a magnet with single domain.

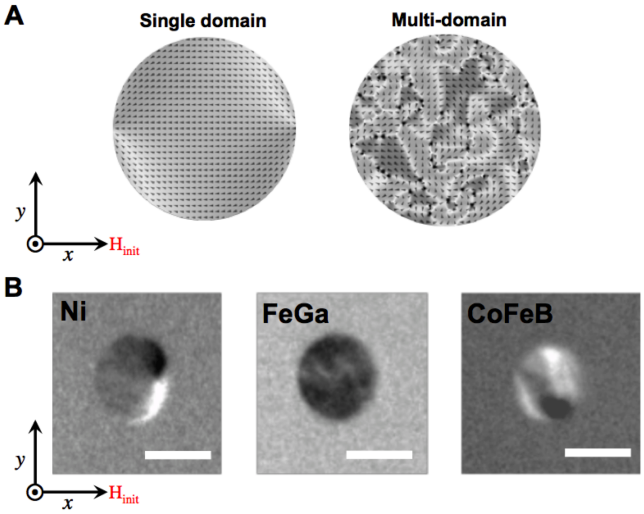

Figure 5.3: An example of single domain and multi-domain in disks at relaxation, simulated by mumax micromagnetics modeling . B.XMCD-PEEM micrographs of magnetoelastic disks of 2 um in diameter, and 20 nm in thickness (polycrystalline Ni, Fe81Ga19 and Co40Fe40B20). Compared to polycrystalline Terfenol-D disks with single domain on the micron scale, these microdisks already exhibit multidomain behavior at 2 um in diameter, implying the domain configuration in even larger structures including disks will fall into multidomains.

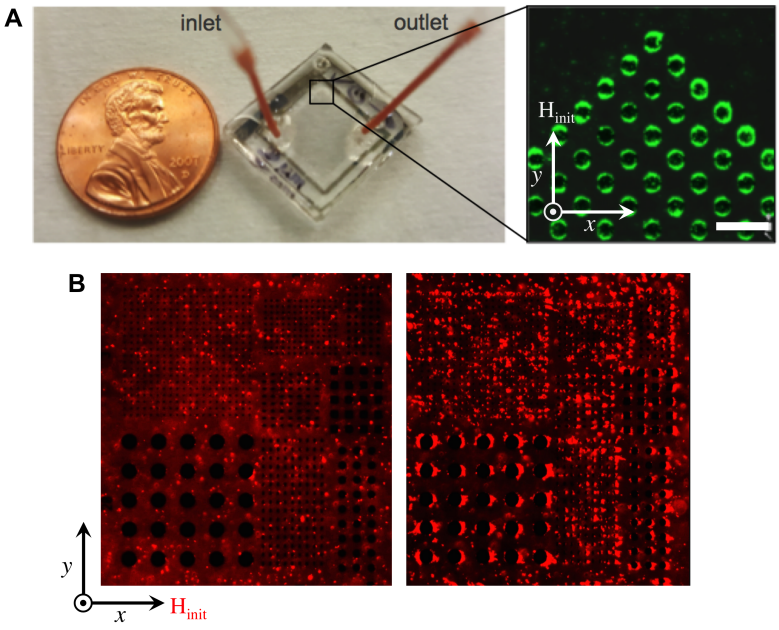

Figure 5.4: Microfluidic device integration with magneto-elastic microstructurs substrate. (A) Microfluidic channel integration with Terfenol-D micropattern on sapphire substrate to visualize magnetic beads (fluorescent label : green) trapping. (B) Before (left) and after (right) magnetic bead (fluorescent label : red) localization on the x-axis poles on different Terfenol-D microstructures.

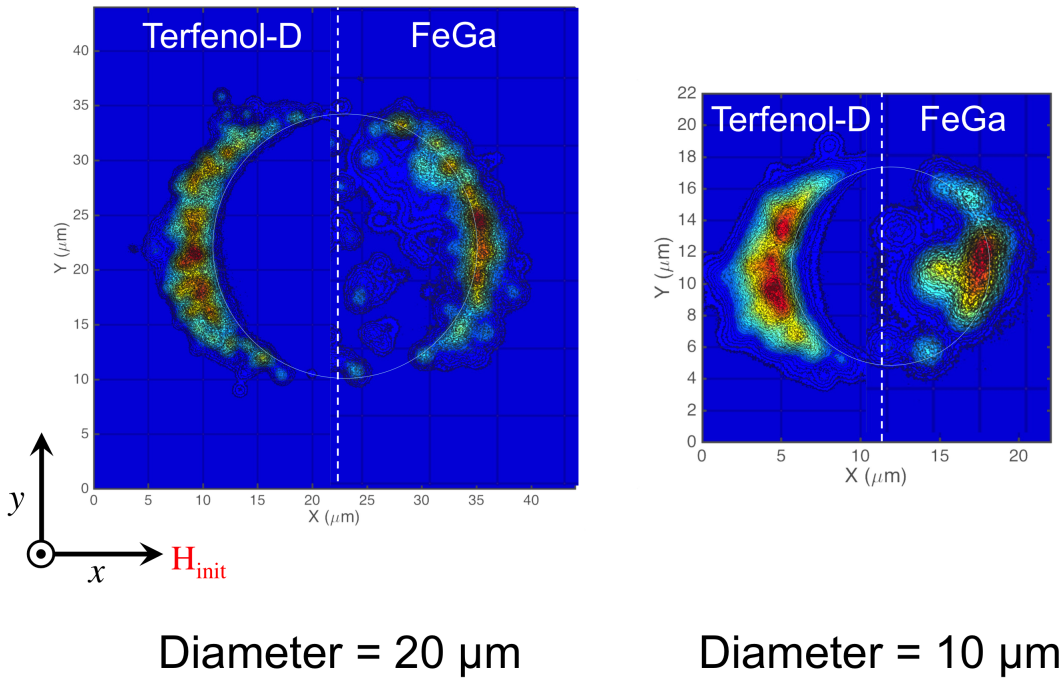

Figure 5.5: Uniform single domain trapping vs non-uniform multi-domain trapping. Heat map of beads trapping locations on magnetically initialized (x-axis) Terfenol-D (TdDyFe) (right) and Galfanol (FeGa) (left) of 10 and 20 μm disks. Magnetic beads are trapped only on the x-axis poles of the Terfenol-D while scattered around the x-axis poles of FeGa.

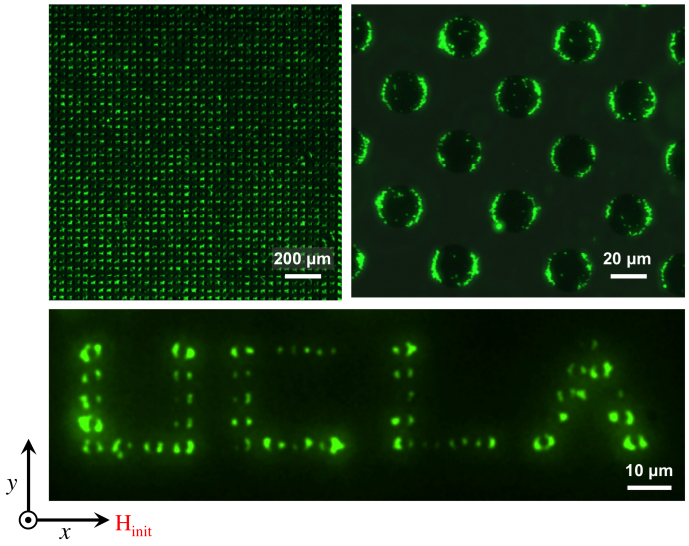

Figure 5.6: Uniform localized stray field gradient of Terfenol-D magnetostrictive microstructures. Fluorescent nanomagnetic particle (green) capture with high trapping rate and precision.

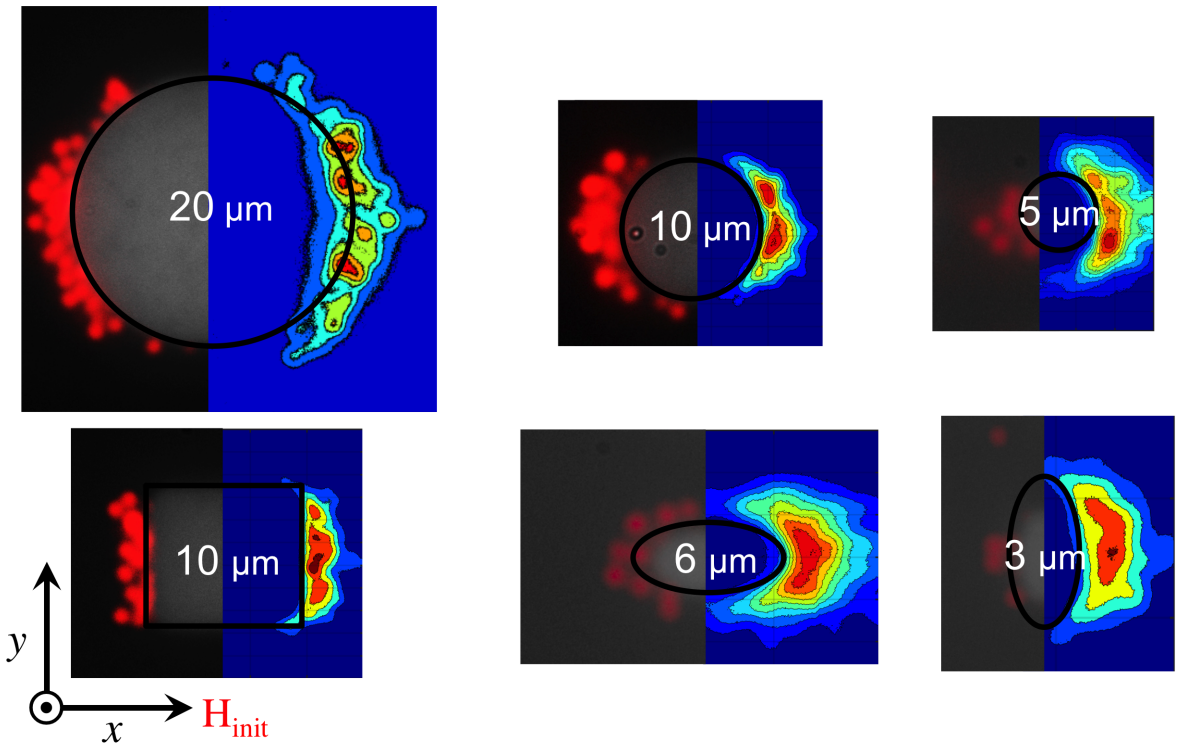

Figure 5.7: Magnetic bead trapping maps on Terfenol-D and Galfenol microstructures 20, 10, 5, 3 μm disks, 10 μm square, x=3 μm and y=6 μm vertical ellipse and finally x=6 μm and y=3 μm horizontal ellipse. Fluorescent images of labeled magnetic beads of more than 20 microstructures are overlaid and analyzed. Contour plot darker red regions correspond to high magnetic beads trapping region and lighter areas depicts low trapping regions. This exhibits precise localization and magnetic trapping of single domain Terfenol-D over various thin film structures.

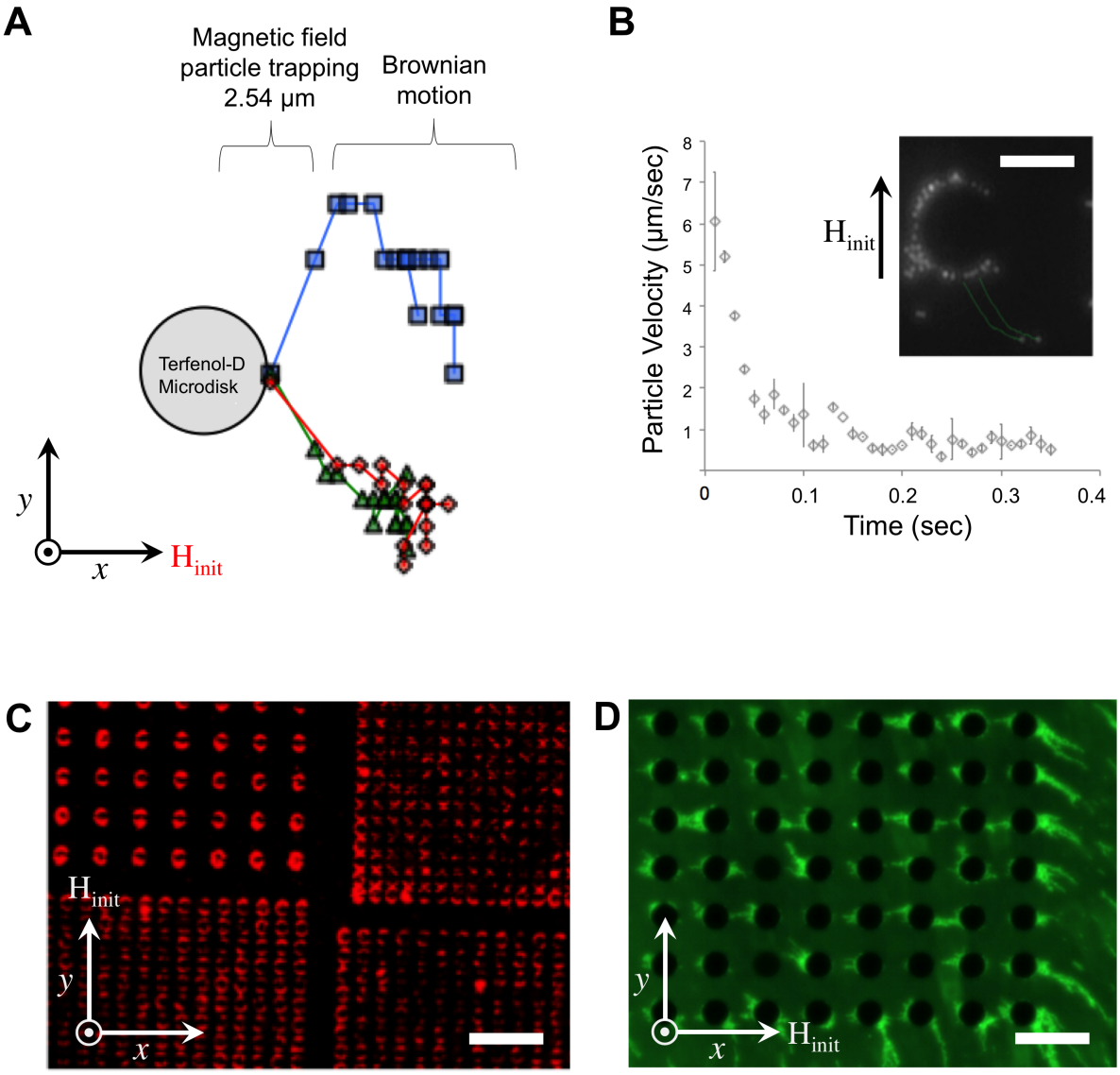

Figure 5.8: Stray field magnetic trapping range from the surface of the the Terfenol-D magnetized poles. (a) Magnetic bead trapping trajectory around Terfenol-D show a transition from random brownian motion to particle displacement towards the magnetized pole of the microdisk. This suggests the effective trapping region of stray field is (2.54 μm).(B) Magnetic particle trapping trajectory show particles accelerating towards the magnetized poles before trapping (scale bar = 20 μm). (C) Small gaps between Terfenol-D microdisk pattern result in less trapping and accumulation of magnetic beads (fluorescent label : red) (scale bar : 100 μm). (D) Magnetic particles (fluorescent label : green) trapped and aligned on the stray field lines and form bridges between Terfenol-D microstructures (scale bar : 50 μm).

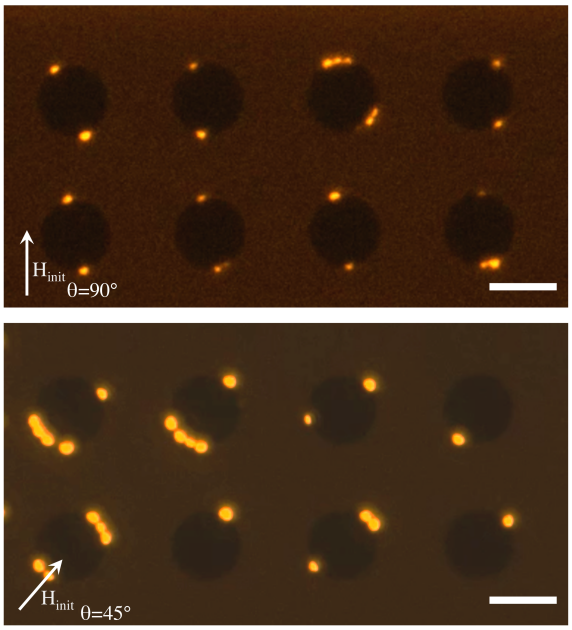

Figure 5.9: Programmable magnetic trapping poles on 20 μm Terfenol-D microdisks magnetized on the y-axis (top) and diagonally (bottom). This demonstrates the programming ability to control magnetic beads (fluorescent label : orange) trapping locations at a micro-scale. (scale bar = 20 μm)

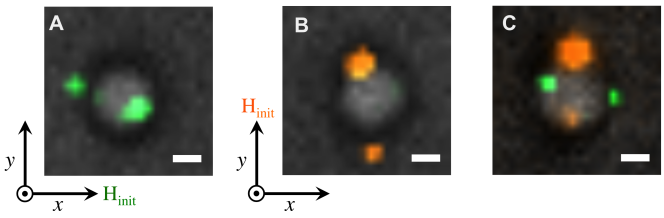

Figure 5.10: Nanomagnetic controlled assembly. Controlled assembly of two different functionalized magnetic nano -particles on single magnetic Terfenol-D disks (3 μm) via two magnetization steps in the x -axis (fluorescent label : green) and y -axis (fluorescent label : orange)(scale bar = 1 μm).

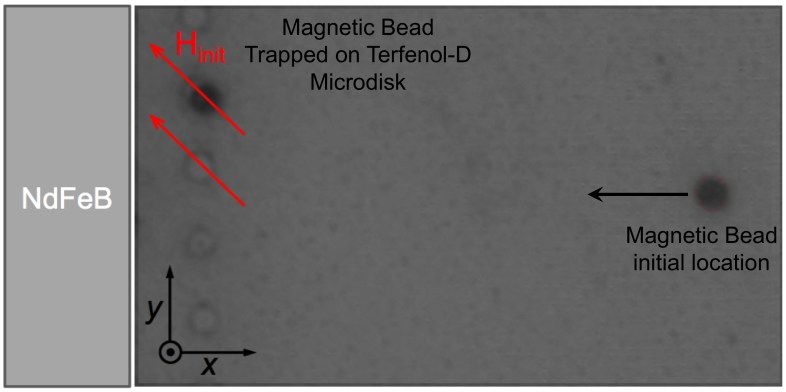

Figure 5.11: Stray field (H_s) initialized diagonally trap magnetic beads moving towards and external magnetic field (B) from large permanent magnet (NdFeB).

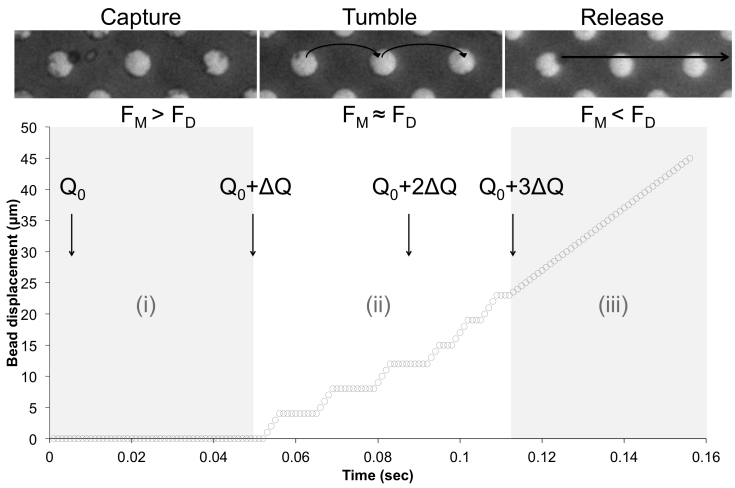

Figure 5.12: Experimental study of fluid born particle interaction with Terfenol-D magnetostrictive microstructures. Three particle-Terfenol-D disk interaction states (i) stagnant particle at initial flow rate (Q_0) when magnetic force dominates over hydrodynamic drag force ($F_m > F_d$). (ii) Increasing flow rate by ($\triangle Q$) demonstrates particle tumbling between Terfenol-D magnetic domain walls when Magnetic binding force is equal or similar to hydrodynamic force ($F_m \approx F_d$). Binding time decrease when hydrodynamic drag force starts to dominate over magnetic binding force. (iii) Last state is particle release when hydrodynamic drag dominates over magnetic binding force ($F_m < F_d$).

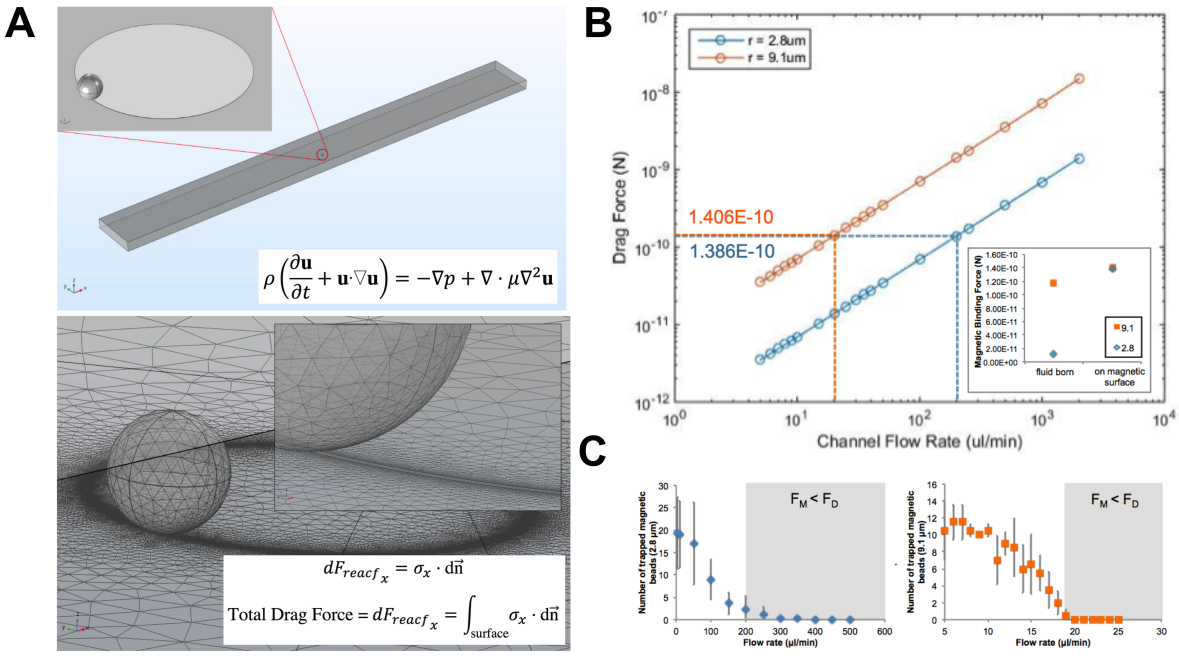

Figure 5.13: Calculation of Hydrodynamic simulation of magnetostrictive microstructure interaction with particle in flow. The drag calculations were performed using COMSOL Multiphysics software Finite Element Method (FEM) to solve the partial differential equations that dictate the physical system to simulate the fluid-particle interactions.

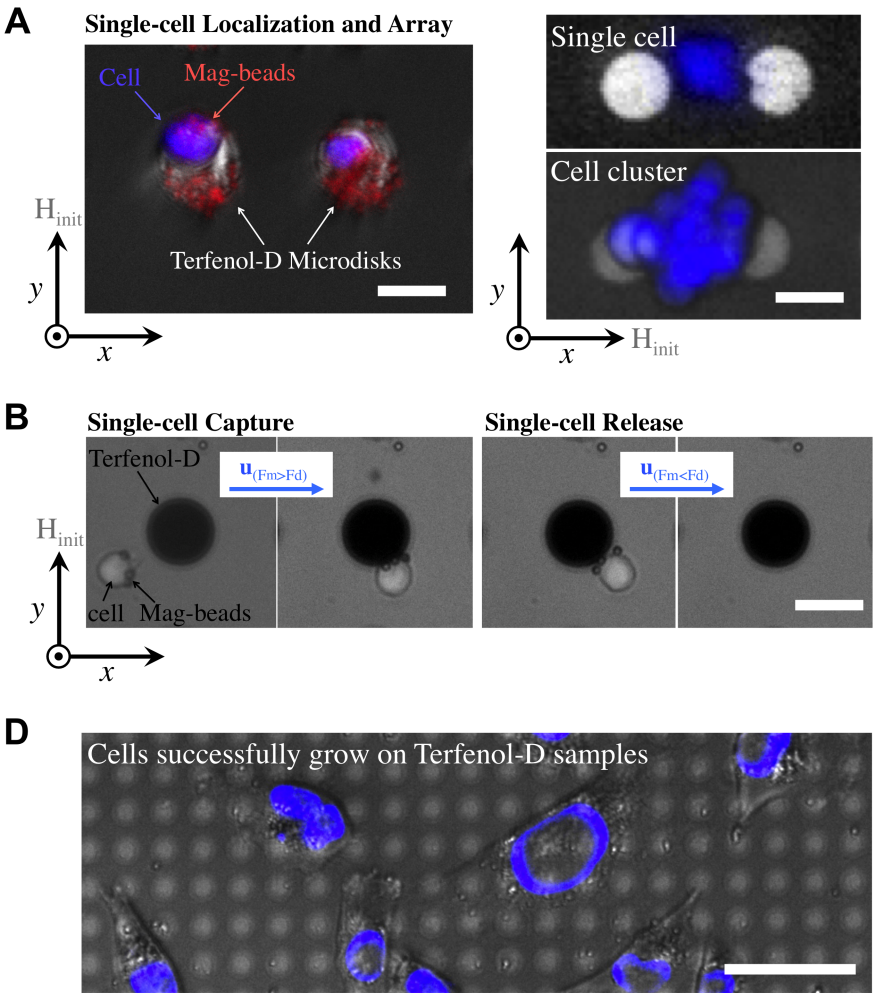

Figure 5.14: Cell manipulation with Terfenol-D micromagnets. (A) Single-cell labeled with magnetic beads were localized in Terfenol-D magnetized poles. Large cells and cell clusters are trapped between two Terfenol-D microstructures. (B) Cells captured by Terfenol-D at low flow were then released by increasing the flow rate, in which hydrodynamic drag dominated over the magnetic binding force. (C) Captured cells were successfully grown on the Terfenol-D micropattern submerged in media.

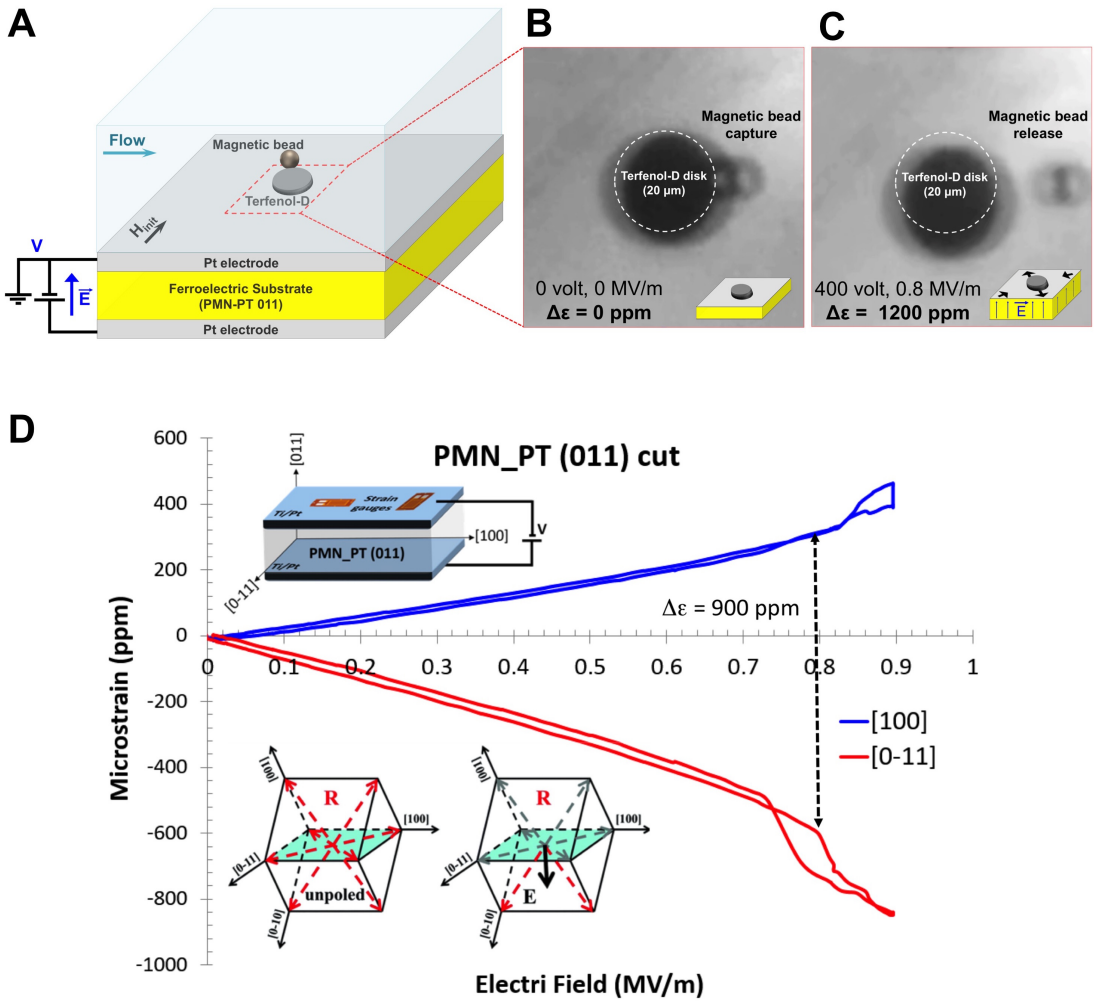

Figure 5.15: Programmable multiferroic micromagnets for single cell capture/release. (A) schematic of magnetoelastic microstructure Terfenol-D on ferroelectric PMN-PT substrate. (B) Magnetic bead capture on Terfenol-D microdisk (diameter = 20 μm). (C) Magnetic bead release due to the rotation of the initial magnetization state of Terfenol-D disk via voltage induced strain when electric field is applied through PMN-PT substrate. (D) An electric field of 0.8 MV m^{-1} induces compressive strain of 900 ppm along [100] direction and tensile strain of 300 ppm along [0-11] direction. The resulting total strain of 1200 ppm, perturbs the single domain state due to magnetic anisotropy variation following which magnetic beads were released from the TerfenolÂŋ-D micromagnets to the outlet of the microchannel.

References

[1] Daniel L Adams, R Katherine Alpaugh, Stuart S Martin, Monica Charpentier, Saranya Chumsri, Massimo Cristofanilli, Diane K Adams, Olga V Makarova, Peixuan Zhu, Shuhong Li, et al. Precision microfilters as an all in one system for multiplex analysis of circulating tumor cells. *RSC advances*, 6(8):6405–6414, 2016.

[2] Hasnain Ahmad, Jayasimha Atulasimha, and Supriyo Bandyopadhyay. Reversible strain-induced magnetization switching in fega nanomagnets: Pathway to a rewritable, non-volatile, non-toggle, extremely low energy straintronic memory. *Scientific reports*, 5:18264, 2015.

[3] Chong H Ahn and Mark G Allen. Fluid micropumps based on rotary magnetic actuators. In *Micro Electro Mechanical Systems, 1995, MEMS'95, Proceedings. IEEE*, page 408. IEEE, 1995.

[4] Ala'aldeen Al-Halhouli, Stefanie Demming, Andreas Waldschik, Stephanus Büttgenbach, et al. Implementation of synchronous micromotor in developing integrated microfluidic systems. *Micromachines*, 5(3):442–456, 2014.

[5] Catherine Alix-Panabières and Klaus Pantel. Challenges in circulating tumour cell research. *Nature Reviews Cancer*, 14(9):623–631, 2014.

[6] Hamed Amini, Elodie Sollier, Mahdokht Masaeli, Yu Xie, Baskar Ganapathysubramanian, Howard A Stone, and Dino Di Carlo. Engineering fluid flow using sequenced microstructures. *Nature communications*, 4:1826, 2013.

[7] Bassem F Armaly, F Durst, JCF Pereira, and B Schönung. Experimental and theoretical investigation of backward-facing step flow. *Journal of fluid Mechanics*, 127:473–496, 1983.

[8] A Baloch, P Townsend, and MF Webster. On two-and three-dimensional expansion flows. *Computers & Fluids*, 24(8):863–882, 1995.

[9] George Keith Batchelor. *An introduction to fluid dynamics*. Cambridge university press, 2000.

[10] Sean C Bendall and Garry P Nolan. From single cells to deep phenotypes in cancer. *Nature biotechnology*, 30(7):639, 2012.

[11] Manuel Bibes and Agnès Barthélémy. Multiferroics: Towards a magnetoelectric memory. *Nature materials*, 7(6):425, 2008.

[12] Axel Birchler, Mischa Berger, Verena JaÌĹggin, Telma Lopes, Martin Etzrodt, Patrick Mark Misun, Maria Pena-Francesch, Timm Schroeder, Andreas Hierlemann, and Olivier Frey. Seamless combination of fluorescence-activated cell sorting and hanging-drop networks for individual handling and culturing of stem cells and microtissue spheroids. *Analytical chemistry*, 88(2):1222–1229, 2016.

[13] Ayan K Biswas, Supriyo Bandyopadhyay, and Jayasimha Atulasimha. Energy-efficient magnetoelastic non-volatile memory. *Applied Physics Letters*, 104(23):232403, 2014.

[14] G. Biswas, M. Breuer, and F. Durst. Backward-facing step flows for various expansion ratios at low and moderate reynolds numbers. *Journal of Fluids Engineering*, 126(3):362, 2004.

[15] Csilla Brasko, Kevin Smith, Csaba Molnar, Nora Farago, Lili Hegedus, Arpad Balind, Tamas Balassa, Abel Szkalisity, Farkas Sukosd, Katalin Kocsis, et al. Intelligent image-based in situ single-cell isolation. *Nature communications*, 9(1):226, 2018.

[16] Lena Breitenstein, Peter Lendecke, Stellan Bohlens, Guido Meier, and Ulrich Merkt. Stray field of a landau magnetization pattern. *Journal of Applied Physics*, 104(8):083909, 2008.

[17] M Buzzi, RV Chopdekar, JL Hockel, A Bur, T Wu, N Pilet, P Warnicke, GP Carman, LJ Heyderman, and F Nolting. Single domain spin manipulation by electric fields in strain coupled artificial multiferroic nanostructures. *Physical review letters*, 111(2):027204, 2013.

[18] Barbaros Çetin and Dongqing Li. Dielectrophoresis in microfluidics technology. *Electrophoresis*, 32(18):2410–2427, 2011.

[19] Hakan Ceylan, Joshua Giltinan, Kristen Kozielski, and Metin Sitti. Mobile microrobots for bioengineering applications. *Lab on a Chip*, 17(10):1705–1724, 2017.

[20] James Che, Albert J Mach, Derek E Go, Ish Talati, Yong Ying, Jianyu Rao, Rajan P Kulkarni, and Dino Di Carlo. Microfluidic purification and concentration of malignant pleural effusions for improved molecular and cytomorphological diagnostics. *PloS one*, 8(10):e78194, 2013.

[21] James Che, Victor Yu, Manjima Dhar, Corinne Renier, Melissa Matsumoto, Kyra Heirich, Edward B Garon, Jonathan Goldman, Jianyu Rao, George W Sledge, et al. Classification of large circulating tumor cells isolated with ultra-high throughput microfluidic vortex technology. *Oncotarget*, 7(11):12748–12760, 2016.

[22] Peng Chen, Yu-Yen Huang, Kazunori Hoshino, and John XJ Zhang. Microscale magnetic field modulation for enhanced capture and distribution of rare circulating tumor cells. *Scientific reports*, 5:8745, 2015.

[23] Yuchao Chen, Peng Li, Po-Hsun Huang, Yuliang Xie, John D Mai, Lin Wang, Nam-Trung Nguyen, and Tony Jun Huang. Rare cell isolation and analysis in microfluidics. *Lab on a Chip*, 14(4):626–645, 2014.

[24] Julian Cheng, M Arifur Rahman, and Aaron T Ohta. Optical manipulation of cells. In *Microtechnology for Cell Manipulation and Sorting*, pages 93–128. Springer, 2017.

[25] XM Cheng and DJ Keavney. Studies of nanomagnetism using synchrotron-based x-ray photoemission electron microscopy (x-peem). *Reports on Progress in Physics*, 75(2):026501, 2012.

[26] NJ Cherry, R Hillier, and MEMP Latour. Unsteady measurements in a separated and reattaching flow. *Journal of Fluid Mechanics*, 144:13–46, 1984.

[27] Jizhai Cui, Joshua L Hockel, Paul K Nordeen, David M Pisani, Cheng-yen Liang, Gregory P Carman, and Christopher S Lynch. A method to control magnetism in individual strain-mediated magnetoelectric islands. *Applied Physics Letters*, 103(23):232905, 2013.

[28] Iwijn De Vlaminck and Cees Dekker. Recent advances in magnetic tweezers. *Annual review of biophysics*, 41:453–472, 2012.

[29] David DeCourtye, Mihir Sen, and Mohamed Gad-el Hak. Analysis of viscous micropumps and microturbines. *International Journal of Computational Fluid Dynamics*, 10(1):13–25, 1998.

[30] Manjima Dhar, Reem Khojah, Andy Tay, and Dino Di Carlo. Research highlights: microfluidic-enabled single-cell epigenetics. *Lab on a Chip*, 15(21):4109–4113, 2015.

[31] Manjima Dhar, Jessica Wong, Armin Karimi, James Che, Corinne Renier, Melissa Matsumoto, Melanie Triboulet, Edward B Garon, Jonathan W Goldman, Matthew B Rettig, et al. High efficiency vortex trapping of circulating tumor cells. *Biomicrofluidics*, 9(6):064116, 2015.

[32] Dino Di Carlo. Inertial microfluidics. *Lab on a Chip*, 9(21):3038–3046, 2009.

[33] Dino Di Carlo, Jon F Edd, Katherine J Humphry, Howard A Stone, and Mehmet Toner. Particle segregation and dynamics in confined flows. *Physical review letters*, 102(9):094503, 2009.

[34] Dino Di Carlo, Daniel Irimia, Ronald G Tompkins, and Mehmet Toner. Continuous inertial focusing, ordering, and separation of particles in microchannels. *Proceedings of the National Academy of Sciences*, 104(48):18892–18897, 2007.

[35] J Döpper, M Clemens, W Ehrfeld, S Jung, KP Kaemper, and H Lehr. Micro gear pumps for dosing of viscous fluids. *Journal of Micromechanics and Microengineering*, 7(3):230, 1997.

[36] F Durst, JCF Pereira, and C Tropea. The plane symmetric sudden-expansion flow at low reynolds numbers. *Journal of Fluid Mechanics*, 248:567–581, 1993.

[37] Haifa El-Sadi and Nabil Esmail. The effects of screw geometry on the pumping efficiency of micro-screw pump. *The Canadian Journal of Chemical Engineering*, 83(6):944–950, 2005.

[38] Anna Fabisiewicz and Ewa Grzybowska. Ctc clusters in cancer progression and metastasis. *Medical Oncology*, 34(1):12, 2017.

[39] Andrew D Fesnak, Carl H June, and Bruce L Levine. Engineered t cells: the promise and challenges of cancer immunotherapy. *Nature Reviews Cancer*, 16(9):566, 2016.

[40] Michael A Fischbach, Jeffrey A Bluestone, and Wendell A Lim. Cell-based therapeutics: the next pillar of medicine. *Science translational medicine*, 5(179):179ps7–179ps7, 2013.

[41] P Fischer, G Denbeaux, T Ono, T Okuno, T Eimüller, D Goll, and G Schütz. Study of magnetic domains by magnetic soft x-ray transmission microscopy. *Journal of Physics D: Applied Physics*, 35(19):2391, 2002.

[42] Nic Fleming. How artificial intelligence is changing drug discovery., 2018.

[43] Michael Foerster, Ferran Macià, Nahuel Statuto, Simone Finizio, Alberto Hernández-Mínguez, Sergi Lendínez, Paulo V Santos, Josep Fontcuberta, Joan Manel Hernàndez, Mathias Kläui, et al. Direct imaging of delayed magneto-dynamic modes induced by surface acoustic waves. *Nature communications*, 8(1):407, 2017.

[44] Thomas P Forbes and Samuel P Forry. Microfluidic magnetophoretic separations of immunomagnetically labeled rare mammalian cells. *Lab on a Chip*, 12(8):1471–1479, 2012.

[45] Juergen Friedrich, Claudia Seidel, Reinhard Ebner, and Leoni A Kunz-Schughart. Spheroid-based drug screen: considerations and practical approach. *Nature protocols*, 4(3):309, 2009.

[46] John A Gallagher, Jian Tian, and Christopher S Lynch. Composition dependence of field induced phase transformations in [0 1 1] c pin–pmn–pt relaxor ferroelectric single crystals with d322 piezoelectric mode. *Acta Materialia*, 81:512–523, 2014.

[47] UKNG Ghia, Kirti N Ghia, and CT Shin. High-re solutions for incompressible flow using the navier-stokes equations and a multigrid method. *Journal of computational physics*, 48(3):387–411, 1982.

[48] Todd M Gierahn, Marc H Wadsworth II, Travis K Hughes, Bryan D Bryson, Andrew Butler, Rahul Satija, Sarah Fortune, J Christopher Love, and Alex K Shalek. Seq-well: portable, low-cost rna sequencing of single cells at high throughput. *Nature methods*, 14(4):395, 2017.

[49] Wei Gong, Hua Li, Zhongren Zhao, and Jinchang Chen. Ultrafine particles of fe, co, and ni ferromagnetic metals. *Journal of Applied Physics*, 69(8):5119–5121, 1991.

[50] Alon Greenbaum, Yibo Zhang, Alborz Feizi, Ping-Luen Chung, Wei Luo, Shivani R Kandukuri, and Aydogan Ozcan. Wide-field computational imaging of pathology slides using lens-free on-chip microscopy. *Science translational medicine*, 6(267):267ra175–267ra175, 2014.

[51] David G Grier. A revolution in optical manipulation. *Nature*, 424(6950):810–816, 2003.

[52] Elisabeth Guazzelli and Jeffrey F Morris. *A physical introduction to suspension dynamics*, volume 45. Cambridge University Press, 2011.

[53] Vishal Gupta, Insiya Jafferji, Miguel Garza, Vladislava O Melnikova, David K Hasegawa, Ronald Pethig, and Darren W Davis. Apostream^{TM}, a new dielectrophoretic device for antibody independent isolation and recovery of viable cancer cells from blood. *Biomicrofluidics*, 6(2):024133, 2012.

[54] Hamed Haddadi and Dino Di Carlo. Inertial flow of a dilute suspension over cavities in a microchannel. *Journal of Fluid Mechanics*, 811:436–467, 2017.

[55] Hamed Haddadi, Hamed Naghsh-Nilchi, and Dino Di Carlo. Separation of cancer cells using vortical microfluidic flows. *Biomicrofluidics*, 12(1):014112, 2018.

[56] Pooria Hadikhani, Navid Borhani, S Mohammad H Hashemi, and Demetri Psaltis. Learning from droplet flows in microfluidic channels using deep neural networks. *Scientific Reports*, 9(1):8114, 2019.

[57] Ki-Ho Han and A Bruno Frazier. Paramagnetic capture mode magnetophoretic microseparator for high efficiency blood cell separations. *Lab on a Chip*, 6(2):265–273, 2006.

[58] Ki-Ho Han and A Bruno Frazier. Lateral-driven continuous dielectrophoretic microseparators for blood cells suspended in a highly conductive medium. *Lab on a Chip*, 8(7):1079–1086, 2008.

[59] Joshua L Hockel, Alexandre Bur, Tao Wu, Kyle P Wetzlar, and Gregory P Carman. Electric field induced magnetization rotation in patterned ni ring/pb (mg1/3nb2/3) o3](1- 0.32)-[pbtio3] 0.32 heterostructures. *Applied Physics Letters*, 100(2):022401, 2012.

[60] Kaitlyn Hood, Soroush Kahkeshani, Dino Di Carlo, and Marcus Roper. Direct measurement of particle inertial migration in rectangular microchannels. *Lab on a Chip*, 16(15):2840–2850, 2016.

[61] Marc Horner, Guy Metcalfe, S Wiggins, and JM Ottino. Transport enhancement mechanisms in open cavities. *Journal of Fluid Mechanics*, 452:199–229, 2002.

[62] Lotien Richard Huang, Edward C Cox, Robert H Austin, and James C Sturm. Continuous particle separation through deterministic lateral displacement. *Science*, 304(5673):987–990, 2004.

[63] Alex Hubert and Rudolf Schäfer. *Magnetic domains: the analysis of magnetic microstructures*. Springer Science & Business Media, 2008.

[64] Soojung Claire Hur, Albert J Mach, and Dino Di Carlo. High-throughput size-based rare cell enrichment using microscale vortices. *Biomicrofluidics*, 5(2):022206, 2011.

[65] Brian D Iverson and Suresh V Garimella. Recent advances in microscale pumping technologies: a review and evaluation. *Microfluidics and nanofluidics*, 5(2):145–174, 2008.

[66] George Barker Jeffery. The rotation of two circular cylinders in a viscous fluid. *Proceedings of the Royal Society of London. Series A, Containing Papers of a Mathematical and Physical Character*, 101(709):169–174, 1922.

[67] T Karino and HL Goldsmith. Flow behaviour of blood cells and rigid spheres in an annular vortex. *Philosophical Transactions of the Royal Society B: Biological Sciences*, 279(967):413–445, 1977.

[68] T Karino and HL Goldsmith. Aggregation of human platelets in an annular vortex distal to a tubular expansion. *Microvascular research*, 17(3):217–237, 1979.

[69] Murat Kaynak, Adem Ozcelik, Nitesh Nama, Amir Nourhani, Paul E Lammert, Vincent H Crespi, and Tony Jun Huang. Acoustofluidic actuation of in situ fabricated microrotors. *Lab on a Chip*, 16(18):3532–3537, 2016.

[70] Philipp J Keller, Annette D Schmidt, Joachim Wittbrodt, and Ernst HK Stelzer. Reconstruction of zebrafish early embryonic development by scanned light sheet microscopy. *science*, 322(5904):1065–1069, 2008.

[71] Reem Khojah, Ryan Stoutamore, and Dino Di Carlo. Size-tunable microvortex capture of rare cells. *Lab on a Chip*, 17(15):2542–2549, 2017.

[72] M Kläui, CAF Vaz, JAC Bland, EHCP Sinnecker, AP Guimaraes, W Wernsdorfer, G Faini, E Cambril, LJ Heyderman, and C David. Switching processes and switching reproducibility in ferromagnetic ring structures. *Applied physics letters*, 84(6):951–953, 2004.

[73] M Kläui, CAF Vaz, L Lopez-Diaz, and JAC Bland. Vortex formation in narrow ferromagnetic rings. *Journal of Physics: Condensed Matter*, 15(21):R985, 2003.

[74] Stephanie Knowlton, Ashwini Joshi, Philip Syrrist, Ahmet F Coskun, and Savas Tasoglu. 3d-printed smartphone-based point of care tool for fluorescence-and magnetophoresis-based cytometry. *Lab on a Chip*, 17(16):2839–2851, 2017.

[75] Jeffrey R Koseff, Ajay K Prasad, Chinyuan Perng, and Robert L Street. Complex cavities: Are two dimensions sufficient for computation? *Physics of Fluids A: Fluid Dynamics*, 2(4):619–622, 1990.

[76] Madeline A Lancaster and Juergen A Knoblich. Organogenesis in a dish: modeling development and disease using organoid technologies. *Science*, 345(6194):1247125, 2014.

[77] Ming Li, Mark van Zee, Carson T Riche, Bobby Tofig, Sean D Gallaher, Sabeeha S Merchant, Robert Damoiseaux, Keisuke Goda, and Dino Di Carlo. A gelatin microdroplet platform for high-throughput sorting of hyperproducing single-cell-derived microalgal clones. *Small*, 14(44):1803315, 2018.

[78] Byeonghwa Lim, Paolo Vavassori, R Sooryakumar, and CheolGi Kim. Nano/micro-scale magnetophoretic devices for biomedical applications. *Journal of Physics D: Applied Physics*, 50(3):033002, 2016.

[79] Chao Liu, Chundong Xue, Jiashu Sun, and Guoqing Hu. A generalized formula for inertial lift on a sphere in microchannels. *Lab on a Chip*, 16(5):884–892, 2016.

[80] Roberto Lo Conte, Zhuyun Xiao, Cai Chen, Camelia V Stan, Jon Gorchon, Amal El-Ghazaly, Mark E Nowakowski, Hyunmin Sohn, Akshay Pattabi, Andreas Scholl, et al. Influence of nonuniform micron-scale strain distributions on the electrical reorientation of magnetic microstructures in a composite multiferroic heterostructure. *Nano letters*, 18(3):1952–1961, 2018.

[81] Liang-Hsuan Lu, Kee Suk Ryu, and Chang Liu. A magnetic microstirrer and array for microfluidic mixing. *Journal of microelectromechanical systems*, 11(5):462–469, 2002.

[82] Enzo O Macagno and Tin-Kan Hung. Computational and experimental study of a captive annular eddy. *Journal of fluid Mechanics*, 28(1):43–64, 1967.

[83] Albert J Mach, Jae Hyun Kim, Armin Arshi, Soojung Claire Hur, and Dino Di Carlo. Automated cellular sample preparation using a centrifuge-on-a-chip. *Lab on a Chip*, 11(17):2827–2834, 2011.

[84] Joshua S Marcus, W French Anderson, and Stephen R Quake. Parallel picoliter rt-pcr assays using microfluidics. *Analytical chemistry*, 78(3):956–958, 2006.

[85] Joseph M Martel and Mehmet Toner. Inertial focusing in microfluidics. *Annual review of biomedical engineering*, 16:371, 2014.

[86] DJ Maull and LF East. Three-dimensional flow in cavities. *journal of Fluid Mechanics*, 16(4):620–632, 1963.

[87] Stefan Miltenyi, Werner Müller, Walter Weichel, and Andreas Radbruch. High gradient magnetic cell separation with macs. *Cytometry: The Journal of the International Society for Analytical Cytology*, 11(2):231–238, 1990.

[88] HK Moffatt. Viscous and resistive eddies near a sharp corner. *Journal of Fluid Mechanics*, 18(01):1–18, 1964.

[89] Tim R Mosmann and Robert L Coffman. Heterogeneity of cytokine secretion patterns and functions of helper t cells. In *Advances in immunology*, volume 46, pages 111–147. Elsevier, 1989.

[90] Coleman Murray, Edward Pao, Peter Tseng, Shayan Aftab, Rajan Kulkarni, Matthew Rettig, and Dino Di Carlo. Quantitative magnetic separation of particles and cells using gradient magnetic ratcheting. *Small*, 12(14):1891–1899, 2016.

[91] Jeonghun Nam, Hyunjung Lim, Dookon Kim, and Sehyun Shin. Separation of platelets from whole blood using standing surface acoustic waves in a microchannel. *Lab on a Chip*, 11(19):3361–3364, 2011.

[92] Keir C Neuman and Attila Nagy. Single-molecule force spectroscopy: optical tweezers, magnetic tweezers and atomic force microscopy. *Nature methods*, 5(6):491, 2008.

[93] Nao Nitta, Takeaki Sugimura, Akihiro Isozaki, Hideharu Mikami, Kei Hiraki, Shinya Sakuma, Takanori Iino, Fumihito Arai, Taichiro Endo, Yasuhiro Fujiwaki, et al. Intelligent image-activated cell sorting. *Cell*, 175(1):266–276, 2018.

[94] Vivian OBrien. Closed streamlines associated with channel flow over a cavity. *Physics of Fluids*, 15(12):2089, 1972.

[95] Nicole Pamme. Magnetism and microfluidics. *Lab on a Chip*, 6(1):24–38, 2006.

[96] Da-Chen Pang and Yi-Wei Lai. Rapid prototyping of a micromotor with an optical rotary encoder. *Micromachines*, 8(6):174, 2017.

[97] Seung-Eek Park and Thomas R Shrout. Ultrahigh strain and piezoelectric behavior in relaxor based ferroelectric single crystals. *Journal of Applied Physics*, 82(4):1804–1811, 1997.

[98] Filip Petersson, Lena Åberg, Ann-Margret Swärd-Nilsson, and Thomas Laurell. Free flow acoustophoresis: microfluidic-based mode of particle and cell separation. *Analytical chemistry*, 79(14):5117–5123, 2007.

[99] Filip Petersson, Andreas Nilsson, Cecilia Holm, Henrik Jönsson, and Thomas Laurell. Separation of lipids from blood utilizing ultrasonic standing waves in microfluidic channels. *Analyst*, 129(10):938–943, 2004.

[100] Marie Pødenphant, Neil Ashley, Kamila Koprowska, Kalim U Mir, Maksim Zalkovskij, Brian Bilenberg, Walter Bodmer, Anders Kristensen, and Rodolphe Marie. Separation of cancer cells from white blood cells by pinched flow fractionation. *Lab on a Chip*, 15(24):4598–4606, 2015.

[101] Mahla Poudineh, Peter M Aldridge, Sharif Ahmed, Brenda J Green, Leyla Kermanshah, Vivian Nguyen, Carmen Tu, Reza M Mohamadi, Robert K Nam, Aaron Hansen, et al. Tracking the dynamics of circulating tumour cell phenotypes using nanoparticle-mediated magnetic ranking. *Nature nanotechnology*, 12(3):274, 2017.

[102] Faxiang Qin and Hua-Xin Peng. Ferromagnetic microwires enabled multifunctional composite materials. *Progress in Materials Science*, 58(2):183–259, 2013.

[103] VL Rayz, L Boussel, MT Lawton, G Acevedo-Bolton, L Ge, WL Young, RT Higashida, and D Saloner. Numerical modeling of the flow in intracranial aneurysms: prediction of regions prone to thrombus formation. *Annals of biomedical engineering*, 36(11):1793, 2008.

[104] Sabine Riethdorf, Harriet Wikman, and Klaus Pantel. Review: Biological relevance of disseminated tumor cells in cancer patients. *International journal of cancer*, 123(9):1991–2006, 2008.

[105] Adam Rosenthal and Joel Voldman. Dielectrophoretic traps for single-particle patterning. *Biophysical journal*, 88(3):2193–2205, 2005.

[106] P Sajeesh and Ashis Kumar Sen. Particle separation and sorting in microfluidic devices: a review. *Microfluidics and nanofluidics*, 17(1):1–52, 2014.

[107] G Segre. Radial particle displacements in poiseuille flow of suspensions. *Nature*, 189:209–210, 1961.

[108] SN Sinha, AK Gupta, and M Oberai. Laminar separating flow over backsteps and cavities. ii-cavities. *AIAA journal*, 20(3):370–375, 1982.

[109] Hyunmin Sohn, Mark E Nowakowski, Cheng-yen Liang, Joshua L Hockel, Kyle Wetzlar, Scott Keller, Brenda M McLellan, Matthew A Marcus, Andrew Doran, Anthony Young, et al. Electrically driven magnetic domain wall rotation in multiferroic heterostructures to manipulate suspended on-chip magnetic particles. *Acs Nano*, 9(5):4814–4826, 2015.

[110] Elodie Sollier, Derek E Go, James Che, Daniel R Gossett, Sean O'Byrne, Westbrook M Weaver, Nicolas Kummer, Matthew Rettig, Jonathan Goldman, Nicholas Nickols, et al. Size-selective collection of circulating tumor cells using vortex technology. *Lab on a Chip*, 14(1):63–77, 2014.

[111] Martin J Stoddart. Cell viability assays: introduction. In *Mammalian Cell Viability*, pages 1–6. Springer, 2011.

[112] Daniel Stoecklein and Dino Di Carlo. Nonlinear microfluidics. *Analytical chemistry*, 91(1):296–314, 2018.

[113] Jiashu Sun, Yike Li, Fusheng Yan, Chao Liu, Yutao Sang, Fei Tian, Qiang Feng, Pengfei Duan, Li Zhang, Xinghua Shi, et al. Control over the emerging chirality in supramolecular gels and solutions by chiral microvortices in milliseconds. *Nature communications*, 9(1):2599, 2018.

[114] Robert M Sutherland. Cell and environment interactions in tumor microregions: the multicell spheroid model. *Science*, 240(4849):177–184, 1988.

[115] Junya Takagi, Masumi Yamada, Masahiro Yasuda, and Minoru Seki. Continuous particle separation in a microchannel having asymmetrically arranged multiple branches. *Lab on a Chip*, 5(7):778–784, 2005.

[116] AmirAli H Talasaz, Ashley A Powell, David E Huber, James G Berbee, Kyung-Ho Roh, Wong Yu, Wenzhong Xiao, Mark M Davis, R Fabian Pease,

Michael N Mindrinos, et al. Isolating highly enriched populations of circulating epithelial cells and other rare cells from blood using a magnetic sweeper device. *Proceedings of the National Academy of Sciences*, pages pnas–0813188106, 2009.

[117] Eric J Topol. High-performance medicine: the convergence of human and artificial intelligence. *Nature medicine*, 25(1):44, 2019.

[118] JR Torczynski and TJ OHern. Numerical simulations of flow in a three-dimensional cavity-channel geometry. Technical report, Sandia National Labs., Albuquerque, NM (United States), 1993.

[119] Y Ueda, T Kida, and M Iguchi. Steady approach of unsteady low-reynolds-number flow past two rotating circular cylinders. *Journal of Fluid Mechanics*, 736:414–443, 2013.

[120] Dwayne AL Vickers, Mengxing Ouyang, Chris Hyunseok Choi, and Soojung Claire Hur. Direct drug cocktail analyses using microscale vortex-assisted electroporation. *Analytical chemistry*, 86(20):10099–10105, 2014.

[121] Daniele Vigolo, Stefan Radl, and Howard A Stone. Unexpected trapping of particles at a t junction. *Proceedings of the National Academy of Sciences*, 111(13):4770–4775, 2014.

[122] Gaszton Vizsnyiczai, Giacomo Frangipane, Claudio Maggi, Filippo Saglimbeni, Silvio Bianchi, and Roberto Di Leonardo. Light controlled 3d micromotors powered by bacteria. *Nature communications*, 8:15974, 2017.

[123] Andreas Waldschik and Stephanus Büttgenbach. Micro gear pump with internal electromagnetic drive. *Microsystem Technologies*, 16(8-9):1581–1587, 2010.

[124] Xiao Wang and Ian Papautsky. Size-based microfluidic multimodal microparticle sorter. *Lab on a Chip*, 15(5):1350–1359, 2015.

[125] Zhuochen Wang and Jiang Zhe. Recent advances in particle and droplet manipulation for lab-on-a-chip devices based on surface acoustic waves. *Lab on a Chip*, 11(7):1280–1285, 2011.

[126] Frank M White and Isla Corfield. Viscous fluid flow, vol. 3, 2006.

[127] Chueh-Yu Wu, Daniel Stoecklein, Aditya Kommajosula, Jonathan Lin, Keegan Owsley, Baskar Ganapathysubramanian, and Dino Di Carlo. Shaped 3d microcarriers for adherent cell culture and analysis. *Microsystems & Nanoengineering*, 4(1):21, 2018.

[128] Tao Wu, Alexandre Bur, Ping Zhao, Kotekar P Mohanchandra, Kin Wong, Kang L Wang, Christopher S Lynch, and Gregory P Carman. Giant electric-field-induced reversible and permanent magnetization reorientation on magnetoelectric ni/(011)[pb (mg 1/3 nb 2/3) o 3](1- x)–[pbtio 3] x heterostructure. *Applied Physics Letters*, 98(1):012504, 2011.

[129] Zhenlong Wu, Yu Chen, Moran Wang, and Aram J Chung. Continuous inertial microparticle and blood cell separation in straight channels with local microstructures. *Lab on a Chip*, 16(3):532–542, 2016.

[130] Nan Xia, Tom P Hunt, Brian T Mayers, Eben Alsberg, George M Whitesides, Robert M Westervelt, and Donald E Ingber. Combined microfluidic-micromagnetic separation of living cells in continuous flow. *Biomedical Microdevices*, 8(4):299–308, 2006.

[131] Zhuyun Xiao, Roberto Lo Conte, Cai Chen, Cheng-Yen Liang, Abdon Sepulveda, Jeffrey Bokor, Gregory P Carman, and Robert N Candler. Bi-directional coupling in strain-mediated multiferroic heterostructures with magnetic domains and domain wall motion. *Scientific reports*, 8(1):5207, 2018.

[132] Zhuyun Xiao, Reem Khojah, Marc Chooljian, Roberto Lo Conte, Joseph D Schneider, Kevin Fitzell, Rajesh V Chopdekar, Yilian Wang, Andreas Scholl, Jane Chang, et al. Cytocompatible magnetostrictive microstructures for nano-and microparticle manipulation on linear strain response piezoelectrics. *Multifunctional Materials*, 1(1):014004, 2018.

[133] Zhuyun Xiao, Kotekar P Mohanchandra, Roberto Lo Conte, C Ty Karaba, JD Schneider, Andres Chavez, Sidhant Tiwari, Hyunmin Sohn, Mark E Nowakowski, Andreas Scholl, et al. Enhanced magnetoelectric coupling in a composite multiferroic system via interposing a thin film polymer. *AIP Advances*, 8(5):055907, 2018.

[134] Masumi Yamada, Megumi Nakashima, and Minoru Seki. Pinched flow fractionation: continuous size separation of particles utilizing a laminar flow profile in a pinched microchannel. *Analytical chemistry*, 76(18):5465–5471, 2004.

[135] Zhi Yao, Yuanxun Ethan Wang, Scott Keller, and Gregory P Carman. Bulk acoustic wave-mediated multiferroic antennas: Architecture and performance bound. *IEEE Transactions on Antennas and Propagation*, 63(8):3335–3344, 2015.

[136] George Youssef, Scott Newacheck, and Mario Lopez. Mapping magnetoelastic response of terfenol-d ring structure. *Applied Physics Letters*, 110(19):192408, 2017.

[137] Jun Zhang, Sheng Yan, Dan Yuan, Gursel Alici, Nam-Trung Nguyen, Majid Ebrahimi Warkiani, and Weihua Li. Fundamentals and applications of inertial microfluidics: a review. *Lab on a Chip*, 16(1):10–34, 2016.

[138] Jian Zhou, Susan Kasper, and Ian Papautsky. Enhanced size-dependent trapping of particles using microvortices. *Microfluidics and nanofluidics*, 15(5):611–623, 2013.